Vibrational Dynamics of Water at Interfaces

Study of vibrational dynamics of water with interface specific time resolved vibrational spectroscopy

Dissertation
zur Erlangung des Grades
„Doktor
der Naturwissenschaften“
am Fachbereich Physik, Mathematik und Informatik
der Johannes Gutenberg-Universität
in Mainz

Malte Deiseroth

geb. in .....

Mainz, den .....

Abstract

Although not proven, it is generally excepted that life without water is not possible. From cloud formation to protein folding, water holds an irreplaceable position in its importance for life. This thesis investigates the structure and the vibrational dynamics of the interfacial water hydrogen bond network at various charged interfaces. The hydrogen bond network is studied by specifically exciting the stretch vibration and probed with interface-specific sum-frequency spectroscopy. Moreover, phase-resolved and pump-probe spectroscopy are used to obtain molecular orientational and temporal information, respectively. At first the muscovite mica mineral-water interface, important for the heterogeneous ice nucleation, is investigated. A correlation between the interfacial water orientation and the ice nucleation temperature on mica is found, establishing water orientation as a possible inducer for ice nucleation. Then the effect of Na_2SO_4 and Na_2CO_3 on the water-air interface is compared. Despite significant differences in the static vibrational spectrum, due to the electrolytes, the same is not found for the vibrational dynamics, hinting towards ion independent water dynamics, even for the here tested large ion concentrations. Last, the influence of charged induced water orientation on the vibrational dynamics of lipid bound interfacial water is studied. The water orientation is hereby controlled using lipids with either a zwitterionic phosphocholine, or a reversed choline-phospho headgroup. The vibrational dynamics, as well as the energy transfer are found to be identical, suggesting orientation independent vibrational dynamics for lipid-bound water.

Zusammenfassung

Obwohl nicht bewiesen, so ist doch allgemein anerkannt, dass Leben ohne Wasser nicht möglich ist. Wasser ist zum Beispiel für Wolkenbildung oder auch Proteinfaltung entscheidend und in seiner Rolle ist Wasser unersetzlich. Diese Dissertation untersucht die Struktur und die Schwingungsdynamik des Wasserstoffbrückenbindungsnetzwerks in Wasser an unterschiedlichen geladenen Grenzflächen. Durch Anregung der Streckschwinung des Wassers wird, mittels grenzflächensensitiver Summen-Frequenz-Spektroskopie, das grenzflächennahe Wasserstoffbrückenbindungsnetzwerk untersucht. Mittels phasenaufgelöster und Pump-Probe Summen-Frequenz-Spektroskopie wird sowohl die molekulare Orientierung, als auch die Lebensdauer der angeregten Zustände, untersucht. Zuerst wird die für heterogene Eisbildung wichtige Muskovit(Glimmer)-Wassergrenzschicht untersucht. Dabei wird eine Korrelation zwischen der Orientierung des grenzflächennahen Wassers und der Nuklisationstemperatur gefunden und somit die Orientierung des Wassers als möglicher Beeinflusser von Eisnukleation vorgestellt. Folgend wird der Effekt von Na_2SO_4 und Na_2CO_3 auf die Schwingungsdynamik der Wasser-Luftgrenzschicht untersucht. Obwohl es im Schwingungsspektrum des Wassers aufgrund der Elektrolyte zu deutlichen Änderungen kommt, wird das Selbe nicht für die Schwingungsdynamik festgestellt. Alle Systeme verhalten sich, innerhalb der Fehlertoleranz, identisch. Zuletzt wird der Einfluss der Wasserorientierung auf die Schwingungsdynamik an Lipid-Wassergrenzflächen untersucht. Die Orientierung des Wassers kann hierbei durch das elektrische Feld der Lipidkopfgruppe gesteuert werden. Es wird gezeigt, dass die Schwingungsdynamik unabhängig von der Wasserorientierung ist. Gleiches gilt auch für den vibrationellen Energietransport an der Grenzfläche, welcher ebenfalls durch die Orientierung des Wassers an der Wasser-Lipidgrenzfläche nicht verändert wird.

Contents

1 Introduction

Vibrational spectroscopy is one of the most successful scientific tools of the last decades. From the comparable simple gas systems, to complex biological structures, the use of vibrational spectroscopy has advanced knowledge in many fields considerably. Vibrational spectroscopy is nowadays routinely used in engines to monitor and tune the conditions for ideal combustion, increasing the efficiency and lifetimes of such engines.[1] On airports, the availability of small Raman spectrometers has made a quick test for drugs and common compounds of explosives possible.[2,3] By combining IR spectroscopy of human blood serum with modern reinforcement learning algorithms, it might be, in the near future, possible to have a quick test for diseases currently difficult to diagnose.[4] As such, scientific work in the field of vibrational spectroscopy is often of interdisciplinary nature with biologically relevant systems, a chemical interpretation, and a physical investigation method.

The interface of different media is of the highest importance for many chemical reactions. In general, all kinds of interaction processes between two media, happen via some kind of interface. It is often the molecular structure and dynamics at interfaces that govern chemical reaction rates and processes.[5] However, the interface is also a notoriously difficult system to study. First, most measurement techniques are not interface-specific, but rather investigate the bulk of a sample. Second, the number of molecules directly at the surface is usually several orders of magnitude smaller than the number of bulk molecules. Thus despite the substantial interest in the properties of materials at the interface, relatively little is known about interfacial mechanisms and how in detail, they affect chemical reactions and their rates.

Throughout the last decades, it has become obvious that the most important biomolecule is water. Although not proven, it is widely accepted, that life without water is not possible. A famous example highlighting the importance of water in biological processes is protein folding. Here water is guiding the backbone of the peptide through its secondary structural assembly into its active structure.[6–8] The lipid-water interaction is crucial for the aggregation of lipid bilayers, forming cell membranes, which are determining the boundary of a cell.[9] However, water is not only important for small scale inner cell effects, but also shapes the climate on earth. Heterogeneous ozone chemistry is largely driven by interfacial chemistry on aerosols. Aerosols are finely suspended particles in water droplets, and they can contain electrolytes at high concentrations on the level of 1 M.[10] Clouds accommodate a large number of aerosols, and cloud formation plays a significant role in the complex and delicately coupled system that shapes the weather on the short and the climate on long time scales. The spatial extent, lifetime, particle size, and radiative properties of clouds are influenced by heterogeneous ice nucleation in aerosols. At temperatures

above −15 °C, ice nucleation is likely initiated by aerosols.[11] At lower temperatures the ice nucleation in clouds is probably dominated by the water-mineral, and in particular the water-feldspar interface.[12]
This thesis provides new insights into the interface-specific vibrations of the water-mineral interface. Specifically the muscovite mica-water interface is studied, where the effect of various surface cations on the average water alignment is investigated and compared to heterogeneous ice nucleation temperature measurements on the same interfaces. A study of the electrolyte influenced water-air interface follows. Where the focus shifts from the cation to the anion. The vibrational dynamics of the Na_2SO_4-water-air, the Na_2CO_3-water air, and the water-air interfaces are compared, and an extensive investigation of the vibrational dynamics of the OD-stretch vibrational region is given. The influence of water alignment on the interfacial vibration dynamics is then studied, by comparing the water zwitterionic lipid interface of two lipids, known to orient the water dipole moment on average in opposing orientation.

1.1 Water as Vibrating Molecule

Water is one of the most, if not the most, important ingredients for life. The molecular structure of water was revealed in the second half of the 18th century, where it was experimentally shown that water consists out of two components, known as oxygen and hydrogen. Up until today the scientific interest in water, and its properties has never rested and is still ongoing. Despite the long and successful story of water studies, still many, in particular collective, properties of water are not well understood and characterized.

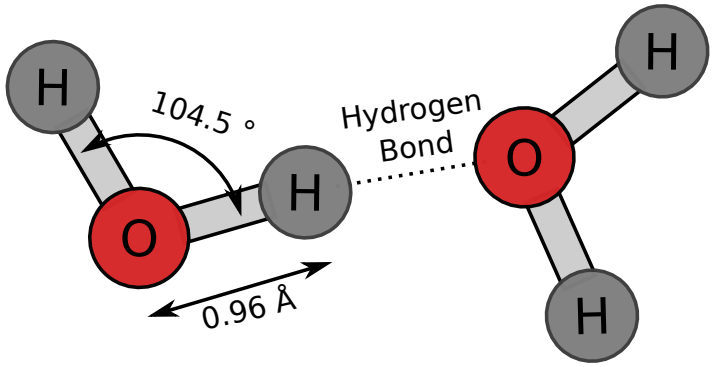

Figure 1.1: Model of two hydrogen-bonded water molecules.

Figure 1.1 shows a molecular model of two hydrogen-bonded water molecules.[13] A single water molecule consists of a single oxygen atom (red), and two covalent bond hydrogen atoms (grey). The average distance between the oxygen and the hydrogen atom is about 0.96 Å. The O-H-O opening angle is about 104.5° and due to the different electronegativity of the oxygen and the hydrogen atoms, water has a dipole moment of about 1.85 D.[14] Two water molecules can form an intermolecular hydrogen bond

with a typical energy barrier of about 0.1 eV-0.3 eV.[15] Each water molecule can as well be a hydrogen bond donor and a hydrogen bond acceptor and form up to four well defined hydrogen bonds with its surrounding water molecules. This hydrogen bond network is related to many of the unusual properties of water and still under intensive investigation.[16]
A method to probe the water hydrogen bond network experimentally is vibrational spectroscopy. Here vibrational normal modes of water are excited and because the surrounding water environment can alter the resonance frequency of the vibrational modes, information about the water environment itself can be extracted.

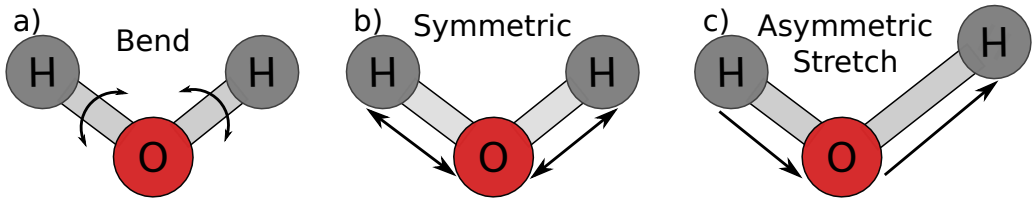

Figure 1.2: Fundamental vibrational modes of a single water molecule.

Figure 1.2 shows the three fundamental vibrational water modes. Figure 1.2 a) depicts the bending mode of water, where the O-H-O angle is altered with a vibrational frequency of about 1600 cm^{-1}. Figure 1.2 b) depicts the symmetric stretch mode. It can be understood as the symmetric change of the distance between each hydrogen atom and the oxygen atom. The asymmetric stretch is shown in Figure 1.2 c) and corresponds to a movement where one hydrogen decreases the distance to the oxygen, while the other increases the distance.
From Figure 1.2 and Figure 1.1 one can see, that the strength of the hydrogen bond, and the vibrational frequency of the OH-stretch vibration are coupled.[17,18] Very generally speaking, the resonance frequency of the undamped harmonic oscillator ω scales with

$$\omega = \sqrt{k/\mu} \tag{1.1}$$

with the force constant k of the harmonic oscillator and μ as effective mass of the system. Upon strengthening the hydrogen bond, one effectively reduces k of the OH-stretch vibration, as k scales with the inverse of the hydrogen bond strength. E.g. the OH-Stretch vibration has a higher resonance frequency for weakly hydrogen-bonded water then for strongly hydrogen-bonded water. This means that the OH-stretch vibration can be used as a reporter of the hydrogen bond strength, as its frequency depends on the local hydrogen bond environment of the probed water.

1.2 Interaction of Light and Matter

In the following, those parts of light-matter interaction relevant for this thesis are discussed. This section is limited to the minimum needed interpreting the following experimental section. It starts with the introduction of matter as a polarizable

medium, describing the fundamentals of light-matter interaction, following a brief introduction to the symmetry properties of the second-order susceptibility. Later on, some useful semiclassical relations of the second-order susceptibility will be presented. In the end, the processes most important for determining the intensity of the pump-probe SFG signal will be discussed.

1.2.1 Matter as Polarizable Medium

The Maxwell equations are a set of differential equations that can be used to describe all optical phenomena. In general, they can be used to describe light-matter interaction. One of the many possible forms of the Maxwell equations is given in the following:

$$\nabla \vec{D} = \rho \tag{1.2}$$

$$\nabla \vec{B} = 0 \tag{1.3}$$

$$\nabla \times \vec{E} = -\frac{\partial \vec{B}}{\partial t} \tag{1.4}$$

$$\nabla \times \vec{H} = \vec{j} + \frac{\partial \vec{D}}{\partial t} \tag{1.5}$$

With the electric displacement field $\vec{D}$, the electric field $\vec{E}$ the magnetic flux density $\vec{B}$, the magnetic filed $\vec{H}$, and the current and charge density j and ρ. $\vec{D}$ and $\vec{B}$ are linked with $\vec{E}$ and $\vec{B}$ via the dielectric and magnetic properties of the present media.

$$\vec{D} = \epsilon_0 \vec{E} + \vec{P} \tag{1.6}$$

$$\vec{B} = \mu_0 \vec{H} + \vec{M} \tag{1.7}$$

With $\vec{M}$ the macroscopic magnetization and $\vec{P}$ the polarization of the media. ϵ_0 is the permittivity and μ_0 the permeability of the vacuum. In the following, natural units will be used, thus $\epsilon_0 \equiv 1$, $\mu_0 \equiv 1$ as well as the speed of light $c \equiv 1$. Note that the polarization and the magnetization are, within the frame of the Maxwell equations, the only properties of a medium, relevant for light matter interaction. The physical interpretation of this is, that only polarization and magnetization of a material are relevant for light-matter interaction. To describe the propagation of light in a neutral medium e.g. water, it is often possible to simplify the equations by assuming no free charges $\rho = 0$, currents $\vec{j} = 0$ as well as a vanishing magnetization $\vec{M} = 0$. With this, the so called wave equation can be derived by calculating $\nabla \times \nabla \times \vec{E}$:

$$\nabla^2 \vec{E} - \frac{\partial^2 \vec{E}}{\partial t^2} = \frac{\partial^2 \vec{P}}{\partial t^2} \tag{1.8}$$

This differential equation links the motion of an electric field with the polarization of the surrounding media. It can be interpreted as if the right hand side of the equation acts as source of radiation, representing the response of the media to the applied electric field. Thus if one wants to understand optical phenomena of light-matter interaction,

the polarization of the medium is of decisive importance. To describe the polarization of matter as a function of the applied electric field, the following power series expansion has been proven to be useful.[19]

$$\vec{P}(t) = \vec{P}^{(1)}(t) + \vec{P}^{(2)}(t) + ... \tag{1.9}$$

$$\vec{P}^{(1)}(t) = \int_{-\infty}^{\infty} \chi^{(1)}(t-t')\vec{E}(t')dt' \tag{1.10}$$

$$\vec{P}^{(2)}(t) = \int_{\infty}^{\infty} \chi^{(2)}(t-t_1, t-t_2)\vec{E}(t_1)\vec{E}(t_2)dt_1dt_2 \tag{1.11}$$

$$\vec{P}^{(3)}(t) = \int_{\infty}^{\infty} \chi^{(3)}(t-t_1, t-t_2, t-t_3)\vec{E}(t_1)\vec{E}(t_2)\vec{E}(t_3)dt_1dt_2dt_3 \tag{1.12}$$

$$\vec{P}^{(4)}(t) = \int_{\infty}^{\infty} \chi^{(4)}(t-t_1, t-t_2, t-t_4)\vec{E}(t_1)\vec{E}(t_2)\vec{E}(t_3)\vec{E}(t_4)dt_1dt_2dt_3dt_4 \tag{1.13}$$

Where $\chi^{(1)}$ to $\chi^{(4)}$ are the linear, second, third and fourth order nonlinear susceptibilities of the medium.[1] It is those $\chi^{(n)}$ terms, that are of general interest, because if the significant elements of $\chi^{(n)}$ are known, the polarization of a medium for a given electric field can be calculated. The convolution in Equation 1.10 - Equation 1.13 is needed to account for causality, meaning that matter can not polarize instantaneously, but instead depends on its prior history. From an experimental point of view it is desirable to transform the polarization into frequency space via Fourier transformation as well as to use a Fourier component Ansatz for the electric field. Because the second-order effect will be the most important throughout the rest of this thesis, we focus on the second-order terms.

$$\vec{P}^{(2)}(\omega) = \int_{-\infty}^{\infty} \vec{P}^{(2)}(t)e^{i\omega t}dt, \qquad \vec{E}(t) = \sum_{\omega} \vec{E}(\omega)e^{-i\omega t} \tag{1.14}$$

together with Equation 1.11 and some resorting we get:

$$\vec{P}^{(2)}(\omega) = \sum_{\omega_i}\sum_{\omega_j}\int_{-\infty}^{\infty} dtdt_2dt_1\chi^{(2)}(t-t_1, t-t_2)\vec{E}(\omega_i)\vec{E}(\omega_j)e^{-i\omega_i t_1 - i\omega_j t_2 + i\omega t} \tag{1.15}$$

With $\omega = \omega_i + \omega_j$ we see that we now have formally the Fourier transformation of $\chi^{(2)}(t-t_1, t-t_2)$ times some electric fields.

$$\chi^{(2)}(\omega = \omega_i + \omega_j) = \int_{-\infty}^{\infty} dtdt_2dt_1\chi^{(2)}(t-t_1, t-t_2)e^{i(\omega_i(t-t_1))+\omega_j(t-t_2)} \tag{1.16}$$

Thus the polarization in frequency space becomes:

$$\vec{P}^{(2)}(\omega) = \sum_{\omega_i}\sum_{\omega_j}\chi^{(2)}(\omega = \omega_i + \omega_j)\vec{E}(\omega_i)\vec{E}(\omega_j) \tag{1.17}$$

[1] For simplicity the spatial components are neglected here. See[19,20] for a complete description.

Interestingly we observe that while the field has frequency components of ω_i and ω_j the polarization has terms with $2\omega_i$, $2\omega_j$ and $\omega_i \pm \omega_j$. It is the existence of those terms that are responsible for the nonlinear processes, called Sum Frequency Generation (SFG), Difference Frequency Generation (DFG) and Second Harmonic Generation (SHG). To observe effects induced by the higher-order terms of the polarization, large amplitudes of the electric field are needed. Therefore the first observation of SHG was published in the year 1961 using a ruby optical maser and shortly after the first observation of SFG proving the fundamental correctness of Equation 1.17.[21,22] Interestingly, it took another 25 Years until 1987 for SFG to be used on a molecular monolayer as a surface-specific spectroscopic tool for the first time.[23] Due to the still ongoing improvements of fs laser systems, SFG has developed into a versatile tool for spectroscopic investigation of interfacial properties on the molecular scale.[24] In the following, some properties of the second order susceptibility will be discussed.

1.2.2 Properties of the Second-Order Nonlinear Susceptibility

The second order susceptibility is a unique material property. Within the electric dipole approximation it exhibits a certain amount of symmetry and inherits symmetry properties from its optical medium. The second order susceptibility in tensor notation for fixed frequencies can take the following form:

$$P_i^{(2)} = \sum_{jk} \chi_{ijk}^{(2)} E_j E_k \tag{1.18}$$

With i, j, k as the Cartesian coordinates and thus $\chi^{(2)}$ is a rank three tensor. By inspecting Equation 1.18, one can see that the indices j and k are dummy indices. They can be freely interchanged without changing the polarization. E.g.:

$$\chi_{ijk}^{(2)} = \chi_{ikj}^{(2)} \tag{1.19}$$

Qualitatively this means the order of the two $\vec{E}$ fields in Equation 1.18 is irrelevant. Because changing the sign of all three subscripts is the same as reversing the axis system, the physical phenomena described by $\chi_{ijk}^{(2)}$ must reverse sing under inversion transformation as well:

$$\chi_{ijk}^{(2)} = (-1)^3 \chi^{(2)}{}_{-i-j-k} \tag{1.20}$$

More constrains on the symmetry of $\chi^{(2)}$ come from the symmetry of the optical medium itself. In the case of a centrosymmetric media the $\chi^{(2)}$ tensor must be invariant under inversion transformation of all coordinates:

$$\chi_{ijk}^{(2)} = \chi_{-i-j-k}^{(2)} \tag{1.21}$$

However, the only way to fulfill Equation 1.20 as well as Equation 1.21 at the same time is, if all components of $\chi^{(2)}$ are 0. Thus the $\chi^{(2)}$ tensor of a centrosymmetric medium vanishes. Yet at the interface of two media, this centrosymmetry is necessarily broken, even if the involved media are centrosymmetric themselves.

Considering a medium at an interface with a C_∞ symmetry axis around the z-axis as shown in Figure 1.3 a), the medium must have inversion invariant and interchangeable x and y components of the $\chi^{(2)}$ tensor as the axes are per definition inversion invariant. In other words, ${\chi^{(2)}}_{xxx}$ equals ${\chi^{(2)}}_{-x-x-x}$. Because Equation 1.20 still holds, the ${\chi^{(2)}}_{xxx}$ component must vanish.

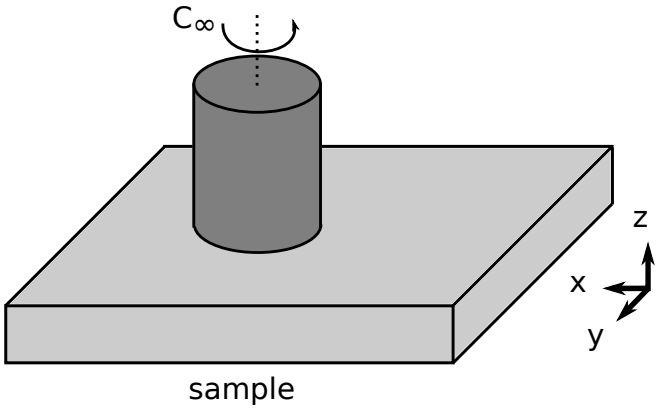

Figure 1.3: Medium with C_∞ axis. Most liquids, and also water, fall into this category. The coordinate system typically has a z-direction perpendicular to the sample surface and the x-y plane parallel to the sample surface.

As a result of these symmetry considerations, the following eight $\chi^{(2)}$ components are left, of which 4 are independent: $\chi^{(2)}_{zxx} = \chi^{(2)}_{zyy}$, $\chi^{(2)}_{xzx} = \chi^{(2)}_{yzy}$, $\chi^{(2)}_{xxz} = \chi^{(2)}_{yyz}$ and $\chi^{(2)}_{zzz}$. This means the second-order susceptibility of a medium with C_∞ symmetry at the vacuum interface is completely described by four independent susceptibility values.

1.2.3 Semi-classical Simplifications

The above-mentioned properties of $\chi^{(2)}$ are very useful in many cases. However, they tell very little about the physical insights of the $\chi^{(2)}$ tensor. An extensive description can be found in literature and is beyond the scope of this thesis.[25–27] Instead, semiclassical models are often used to derive some of the fundamental properties of $\chi^{(2)}$. The semiclassical approach is particularly helpful when dealing with large molecular ensembles and collective effects, as these ensemble effects can overshadow the quantum mechanical details. Semiclassical models can result in a simpler and more intuitive understanding of nonlinear optical effects. It is very useful to relate $\chi^{(2)}$ with the number density of excited oscillators, their average orientational dipole alignment and the so-called hyperpolarizability $\beta^{(2)}_{i'j'k'}$.[28]

$$\chi^{(2)}_{ijk} = N \sum_{i'j'k'} \langle R_{ii'} R_{jj'} R_{kk'} \beta^{(2)}_{i'j'k'} \rangle \tag{1.22}$$

With $R_{\lambda\lambda'}$ as element of the Euler rotational transformation matrix, transforming from the molecular coordinates system λ'(a,b,c) to the laboratory coordinates λ(x,y,z). The

hyperpolarizabilities $\beta_{i'j'k'}$ have been worked out in detail by Hirose et al.[29] Typically for molecular SFG spectroscopy, the IR frequency is near a molecular vibrational resonance. Thus the second-order molecular polarizability is described by:

$$\beta^{(2)} = \beta^{(2)}_{\mathrm{NR}} + \sum_q \frac{\beta^q}{\omega_{IR} - \omega_q + i\Gamma_q} \tag{1.23}$$

With the first term $\beta^{(2)}_{\mathrm{NR}}$ representing a non-resonant contribution and β^q, ω_q and Γ_q as the sum-frequency strength factor tensor, resonant frequency and damping constant of the qth molecular vibrational mode. The tensor elements of β are in turn related to the IR and Raman properties of the vibrational mode:[30]

$$\beta^q_{r'j'k'} = -\frac{1}{2\omega_q} \frac{\partial \alpha^{(1)}_{i'j'}}{\partial Q_q} \frac{\partial \mu_{k'}}{\partial Q_q} \tag{1.24}$$

with $\frac{\partial \alpha^{(1)}_{i'j'}}{\partial Q_q}$ and $\frac{\partial \mu_{k'}}{\partial Q_q}$ the partial derivatives of the Raman polarizability tensor and the IR transition dipole moment of the qth vibrational mode. Q_q is the normal coordinate of mode q. The appearance of these two terms is also the reason why a molecular vibration needs to be Raman and IR active to be resonant in SFG Spectroscopy. Thus for simple molecules, this can serve as a quick check whether a vibration is SFG-resonant, by checking whether the vibration changes the dipole moment as well as the polarizability of a molecule. If both are the case, then a vibration can be expected to be SFG active. Further one learns that the intensity of the SFG signal increases with the average alignment of the oscillators. However note that the term alignment can be misleading in this case, as both, a completely random, as well as a centrosymmetric confirmation can lead to a cancellation of the SFG signal.[31]

2 Interface Specific Vibrational Spectroscopy

Up to this point it is not clear how to experimentally access any of the mentioned material properties. However from Equation 1.20 and Equation 1.21, one can see that the $\chi^{(2)}$ tensor of a centrosymmetric medium vanishes. Thus a $\chi^{(2)}$ signal of a centrosymmetric medium must originate from the inherently non-centrosymmetric interface of the medium. This is the reason why SFG is considered interface specific, even though it technically is just suppressed within centrosymmetric media.
In the following, the most important experimental aspects of interface-specific vibrational spectroscopy will be explained. It will start with an introduction of the experimental details of static SFG. Here both, static, as well as phase-resolved SFG will be discussed. Following an introduction to the field of time-resolved pump-probe SFG. Afterwards, the setup used throughout this thesis will be described, and the basic properties characterizing the setup will be presented.

2.0.1 The Intensity of Sum Frequency Generation

To access vibrational modes of molecules, typically laser light close to the resonance of the investigated vibrational mode is used. The stretch vibration of, e.g., water has its fundamental resonance frequency at $3200\,\mathrm{cm}^{-1}$. If heavy water (D_2O) is used, the stretch vibration is found at $2400\,\mathrm{cm}^{-1}$.[32,33] This means, to probe vibrational modes Infrared (IR) laser light in the range of $1000\,\mathrm{cm}^{-1}$ to $4000\,\mathrm{cm}^{-1}$ can be used. The availability of short-pulsed, high power Ti:sapphire laser systems marks a major breakthrough in this field, as it allows to generate broad band IR pulses with a spectral width of up to about $1000\,\mathrm{cm}^{-1}$, depending on the central frequency.[34,35] This is particularly useful for the study of the water stretch vibration, having a broad resonance of about $800\,\mathrm{cm}^{-1}$ at a central frequency of about $3200\,\mathrm{cm}^{-1}$.
Figure 2.1 a) depicts the energy scheme of an SFG process. An IR photon excites the sample resonantly from the ground state $|g\rangle$ into the vibrational excited state $|v\rangle$. A second photon (VIS) upconverts the system into an unstable virtual state $|s\rangle$, from where the SFG photon, with a frequency of the sum of $\omega_{IR}+\omega_{VIS}=\omega_{SFG}$ is emitted. The exact frequency of the VIS photon is, as long as it is far from any resonance, not important. It is simply there to up-convert the resonant IR laser beam into interface-specific SFG light. A practical advantage of 800 nm up-conversion is that the resulting SFG light can be detected at around 675 nm and is thus in the visible region, where many and also cost efficient optical elements are available. Figure 2.1 b) shows the beam configuration of an SFG setup. To generate SFG light, the two laser beams IR

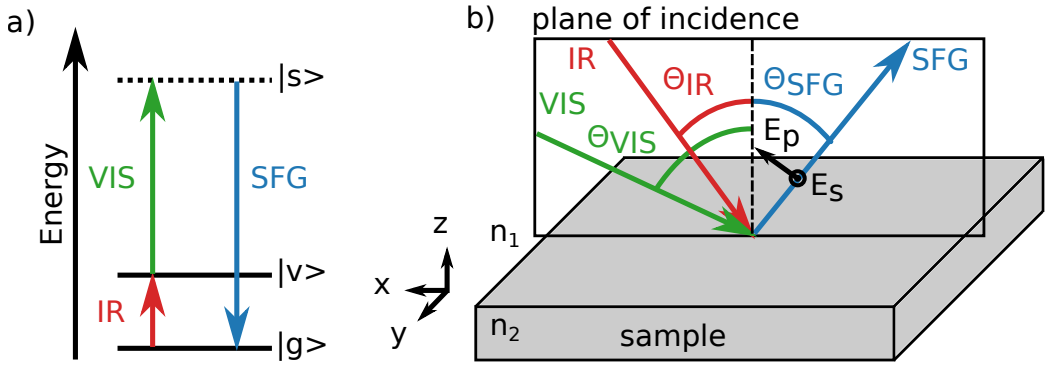

Figure 2.1: a) Energy levels of the SFG process. The IR beam is resonant with a molecular vibration and the VIS up-converts to a virtual vibrational state. Upon relaxation, SFG light is emitted. b) Beam geometry of an SFG experiment. Reflection and transmission of IR, VIS, and SFG beam are omitted for clarity. n_1 is the refractive index of air, n_2 is the refractive index of the medium.

and VIS need to be overlapped in time and space on the sample. From now on a beam oriented geometry instead of a cartesian coordinate system is used. In this geometry, all beams, IR, VIS and SFG lie within the same plane of incidence. The beam angles Θ_{IR}, Θ_{VIS} and Θ_{SFG} are defined with respect to the surface normal of the sample. Thus, the polarization of the a beam can be described by two components, an in-plane component (p for parallel) and an out-of-plane component (s for senkrecht). As such the electrical components of the laser beams translate to:

$$E_x = E_p \cos\theta_i, \quad E_y = E_s, \quad E_z = E_p \sin\theta_i \tag{2.1}$$

By probing different polarization components, it is possible to probe different components of the $\chi^{(2)}$ tensor. The following table shows a mapping between polarization combinations and Cartesian $\chi^{(2)}_{ijk}$ elements in the case of an azimuthally isotropic interfaces (C_∞) like water-vacuum. Note the polarizations are typically given in the order of SFG, VIS, IR.

Polarization	Elements of $\chi^{(2)}_{ijk}$
PSS	$\chi^{(2)}_{zyy}$
SPS	$\chi^{(2)}_{yzy}$
SSP	$\chi^{(2)}_{yyz}$
PPP	$\chi^{(2)}_{zzz}, \chi^{(2)}_{zxx}, \chi^{(2)}_{xzx}, \chi^{(2)}_{xxz}$

In the following the relation between $\chi^{(2)}_{SSP}$ and $\chi^{(2)}_{yyz}$ will be shown, as the SSP polarization is the only polarization used throughout this thesis. The complete set of equations can be found in literature.[36] The SFG intensity in the reflected direction

is given by:

$$I(\omega_{\mathrm{SFG}}) = \frac{8\pi^3 \omega_{\mathrm{SFG}}^2 \sec^2\theta_{\mathrm{SFG}}}{n(\omega_{\mathrm{SFG}})n(\omega_{\mathrm{VIS}})n(\omega_{\mathrm{IR}})} \left|\chi_{eff}^{(2)}\right|^2 I_{\mathrm{VIS}}(\omega_{\mathrm{VIS}}) I_{\mathrm{IR}}(\omega_{\mathrm{IR}}) \tag{2.2}$$

Here n is the refractive index of the sample as a frequency dependent function, ω_i with $i \in \{\mathrm{SFG}, \mathrm{VIS}, \mathrm{IR}\}$ the respective wavenumber, θ_{SFG} the reflection angle of the SFG light and I the respective Intensity. The effective nonlinear susceptibility is given by $\chi_{eff}^{(2)}$ as:

$$\chi_{eff}^{(2)} = [\vec{e}(\omega_{\mathrm{SFG}})\vec{L}(\omega_{\mathrm{SFG}})]\chi^{(2)}[\vec{L}(\omega_{\mathrm{VIS}})\vec{e}(\omega_{\mathrm{VIS}})][\vec{L}(\omega_{\mathrm{IR}})\vec{e}(\omega_{\mathrm{IR}})] \tag{2.3}$$

With $\vec{e}(\omega)$ the unit polarization vector and $\vec{L}(\omega_i)$ the Fresnel factor at frequency ω_i. To transform between the beam coordinate system (SSP) and the sample coordinate system (yyz) the following equation can be used:

$$\chi_{SSP}^{(2)} = L_{yy}(\omega_{SFG})L_{yy}(\omega_{VIS})L_{zz}(\omega_{IR})\sin\theta_{IR}\chi_{yyz}^{(2)} \tag{2.4}$$

With $L_{yy}(\omega)$ and $L_{zz}(\omega)$ as diagonal elements of $\vec{L}(\omega)$ given by

$$L_{xx}(\omega_i) = \frac{2n_1(\omega_i)cos\gamma_i}{n_1(\omega_i)cos\gamma_i + n_2(\omega_i)cos\theta_i} \tag{2.5}$$

$$L_{yy}(\omega_i) = \frac{2n_1(\omega_i)\cos\theta_i}{n_1(\omega_i)\cos\theta_i + n_2(\omega_i)\cos\gamma_i} \tag{2.6}$$

$$L_{zz}(\omega_i) = \frac{2n_2(\omega_i cos\theta_i)}{n_1(\omega_i)cos\gamma_i + n_2(\omega_i)cos\theta_i}\left(\frac{n_1(\omega_i)}{n'(\omega_i)}\right)^2 \tag{2.7}$$

With γ_i the refracted angle from $n_1(\omega_i)\sin\theta_i = n_2(\omega_i)\sin\gamma_i$. n' is the effective refractive index parameter of the interfacial layer. Typically n' is an unknown parameter in this equation. However for a selected amount if systems, n' was studied in greater detail.[36,37]

This means $\chi_{SSP}^{(2)}$ and $\chi_{yyz}^{(2)}$ are proportional and to translate between the two coordinate systems, the refractive index n_j of the media, as well as the angles of incidence need to be known. A practical implication of this is that Fresnel factors need to be taken into account, if one wants to compare SFG spectra of different setups having different beam geometry. This is in particular important for buried interfaces, where the Fresnel factors can introduce significant distortion to the observed spectra.[38]

At this point by combining Equation 2.2 with Equation 1.22, we see that the intensity of SFG light scales like:

$$I_{SFG} \propto |E_{SFG}|^2 \propto |\chi^{(2)}|^2 = N^2|\langle\beta^{(2)}\rangle|^2 \tag{2.8}$$

with E_{SFG} as electric field of the emitted SFG light, N the number of oscillators and $\langle\beta^{(2)}\rangle$ the orientational average of the hyperpolarizability closely related to the dipole moment $\langle\mu_z\rangle$ in the case of SSP polarization.[27] Therefore relative SFG intensity

variations can be caused by changes in the orientation of the oscillators ($\langle\beta^{(2)}\rangle$), and/or changes in the density (N^2) of the oscillators.
In summary, SFG allows observing several interfacial properties of water. By comparing relative intensities, one can investigate the average alignment of water at the interface. Further changes in frequency can hint towards structural changes in water, where the hydrogen bond can be strengthened or weakened.[17]

2.0.2 Signal Normalization to Correct for the IR-Spectrum

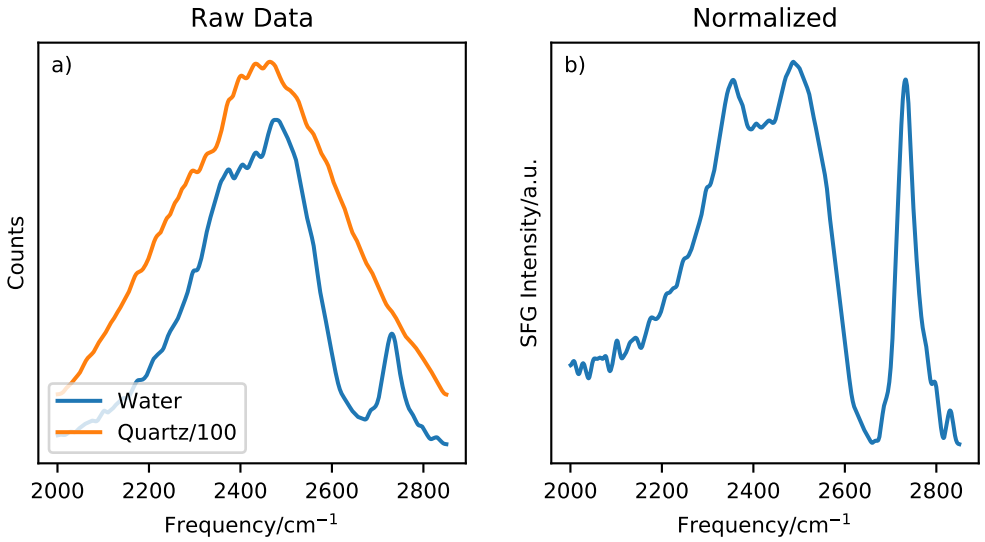

Figure 2.2: a) SFG of the D_2O-Air and Quartz-Air interface. Measurement time for water is 100s, the measurement time for quartz is 10s. Counts on quartz are divided by 100. b) Normalized water spectrum after division with the quartz spectrum.

To account for the spectrum of the broad IR laser pulse, a reference SFG spectrum has to be recorded during each SFG measurement. Due to its strong and reproducible SFG signal, z-cut quartz is used for this. Figure 2.2 a) shows the raw SFG signal generated at the Quartz-Air and the D_2O-Air interface. The quartz spectrum was recorded for 10 s, while the water spectrum was recorded for 100 s. Still, the quartz signal is roughly 100 times larger than the signal generated by the D_2O-Air interface. All recorded SFG spectra are divided by the corresponding quartz SFG signal. Because all angles and the coherence length of the SFG setup are known, as well as the $|\chi^{(2)}|^2$ of quartz in absolute numbers (V^4m^{-2}), this could, in principle, be used to calculate an absolute scale for the SFG signal.[39,40] However, the care needed to do so is experimentally demanding, and most of the time not necessary. Thus SFG spectra are typically reported in arbitrary units (a.u.), and amplitudes are only compared if the experimental conditions allow so.

2.0.3 Separating Real and Imaginary part of $\chi^{(2)}$

As seen from Equation 2.2, intensity-based SFG, only allows to access $|\chi^{(2)}|^2$. As $\chi^{(2)}$ is, in general, a complex quantity, information about the real and imaginary part of $\chi^{(2)}$ is lost. With so called phase-resolved SFG (PS-SFG) this obstacle can be overcome. PS-SFG was first deployed in the year 1990[41] with a ps laser system, it matured through the years and was 2008 for the first time used in a fs based laser systems.[42] It quickly became an important tool in the field of surface sensitive spectroscopy. For an in-depth explanation of the method, the interested reader is redirected to.[42]

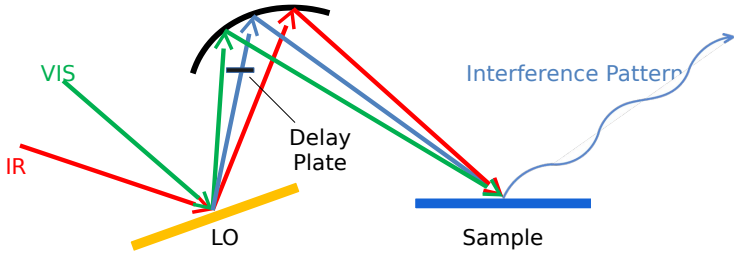

Figure 2.3: Sketch of the sample stage of a phase-resolved SFG setup. The Local Oscillator (LO) generates a strong SFG signal. The reflected laser beams are focused by a curved mirror onto the sample generating a second SFG signal. The frequency-dependent interference pattern of both SFG signals is recorded on a CCD Camera.

Figure 2.3 is a conceptual sketch of the sample stage of a PS-SFG setup. At a qualitative level, PS-SFG extends SFG by an additional signal from a local oscillator (LO). Often the LO SFG signal is produced on either a gold or a quartz sample. Instead of directly recording the LO SFG signal, it is, together with the reflection of the visible and the IR laser beam, collected on a parabolic mirror and refocused on to the sample. It is of crucial importance that the LO signal is temporally delayed with respect to the reflected IR and visible beams. At the sample, the visible and the IR beam are overlapped once again, generating sum-frequency light. The two SF signals (the one from the LO and the one from the sample) generate an observable interference pattern on the detector. This interference pattern is then compared to the interference pattern of a reference, and via Fourier transformation, the real and imaginary components of the signal are extracted. These real and imaginary components are proportional to the real and imaginary parts of the sample $\chi^{(2)}$.
Figure 2.4 shows the data processing pipeline of a PS-SFG experiment. At first, an interference pattern is observed a). This interference pattern is Fourier transformed into time-space as seen in b). Only the, by the delay plate, delayed components of the signal are extracted. This corresponds to a bandpass filter in time. Next, an inverse Fourier transformation is performed, resulting in the spectrum shown in c). After normalization with a reference signal the real and imaginary components of the signal are obtained d) and these components are proportional to the real and imaginary

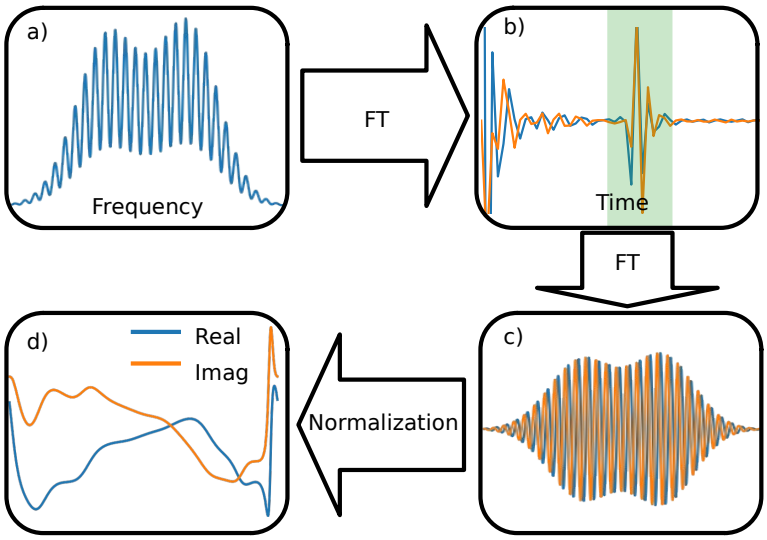

Figure 2.4: Data processing of a PS-SFG setup. a) Fourier transformation is used to separate the real and imaginary parts of the interference pattern. b) The time selection is based on the delay due to the thickness of the delay plate (green rectangle). c) Reverse Fourier transformation transforms the signal back into frequency space, and after normalization with a reference (d) real and imaginary component of $\chi^{(2)}$ can be extracted.

components of the samples $\chi^{(2)}$.
One of the most important features of PS-SFG is that it can be used to determine the orientation of the transition dipole moment. Because the sign of the imaginary component of $\chi^{(2)}$ corresponds to the sign of the transition dipole moment. The transition dipole moment of water points into the direction of the two hydrogen atoms, this means, if the sign of the $\mathrm{Im}(\chi^{(2)})$ is negative, water points on average into the bulk phase and if the sign is positive water points on average up into vapor phase. Therefore this technique can be used to investigate interfacial water orientation.

2.0.4 Bulk Signal due to Field Induced $\chi^{(3)}$ Effects

Field-induced effects can add bulk contributions to the observed SFG intensity. This is known as a field-induced $\chi^{(3)}$ effect and arises, when an electric field, reaching from the interface into the bulk, is present.[43–45] This can be the case if, e.g., water with surface-active ions is investigated.
Figure 2.5 is a sketch, for surface active ions, with the cations on average closer to the surface then the anions. Due to the different average distance of the anions and cations to the water-vapor interface, an electric field, E_z arises. This electric field can in turn effectively enlarge the non centrosymmetric interfacial region. As a result the SFG signal does not only depend on $\chi^{(2)}$, but is accompanied by a $\chi^{(3)}$ bulk term

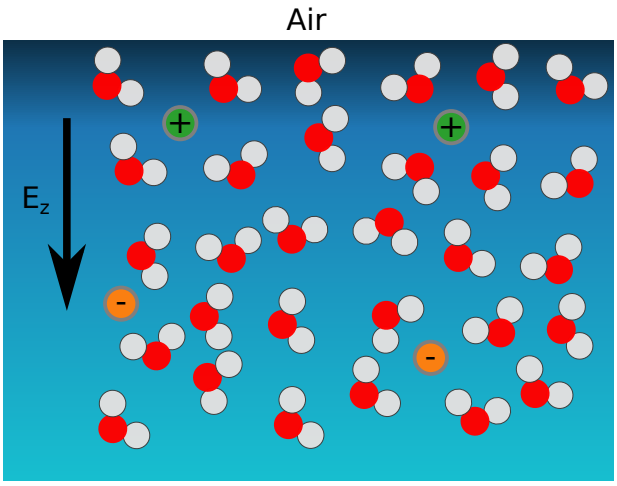

Figure 2.5: Sketch of the water-air interface in the presence of ions. If one species of ions is on average closer to the interface than the corresponding counter ion, an interfacial electric field is induced. This electric field effectively increases the region of non-centrosymmetry and thus adds a bulk-like contribution to the measured SFG intensity.

resulting in:

$$I(\mathrm{SFG}) \propto \left| E_{\mathrm{VIS}} E_{\mathrm{IR}} \left(\chi^{(2)} + \int_0^\infty \chi^{(3)} E_z(z) e^{i\Delta k_z z} dz \right) \right|^2 \tag{2.9}$$

with the electric field $E_z(z)$ and the phase mismatch Δk_z integrated from the interface $z = 0$ into the bulk.
It is neither trivially possible to disentangle the $\chi^{(3)}$ and the $\chi^{(2)}$ signal from one another, measuring the total SFG intensity, nor is the absolute size of the $\chi^{(3)}$ term known in general. However, in the case of water, the frequency dependency of the $\chi^{(3)}$ term has been measured.[45] This $\chi^{(3)}$ spectrum of water can be used to estimate the influence on the spectral shape of the measured $I(\mathrm{SFG})$ intensity.[46]

2.1 Vibrational Dynamics of Molecules at Interfaces

The methods discussed up to this point all investigate the static properties of $\chi^{(2)}$. However in particular for chemical reactions, also the dynamics are relevant.[5] For example, it has been shown that water exhibits fast vibrational dynamics on the sub ps time scale.[47–49] Thus throughout this section, Pump-Probe SFG (PP-SFG), a method for investigating the temporal evolution of vibrational modes at the interface, is presented. PP-SFG is a time resolving extension of ordinary SFG. Here two IR laser, the so-called pump and probe lasers are used. The probe laser corresponds to the IR laser of an SFG experiment. However, the intensity of the SFG light is different in the presence or absence of the pump laser. Thus by comparing the SFG signal

intensity with and without the pump laser and by changing the time delay between the pump and the probe laser pulses, the vibrational lifetime of the excited states can be investigated.

2.1.1 The Intensity of a Pump-Probe SFG Experiment

During a pump-probe experiment, the sample is probed within two different states. In the following, these two states will be called pumped and unpumped. The sample is unpumped, if no interaction with the pump laser has taken place. This corresponds to the ordinary SFG process described in subsection 2.0.1. Consequently, the state after interaction with the pump laser is called pumped. Physically this translates into probing two different terms of $\vec{P}(t)$. If the pump laser is off, $P^{(2)}$ from Equation 1.11 is probed. If the pump laser is on, $P^{(4)}$ of Equation 1.13 is probed. Figure 2.6 shows the most important double-sided Feynman diagrams of a pump-probe SFG experiment. The rules for generating double-sided Feynman diagrams are beyond the scope of this thesis, and the interested reader is redirected to[26,50]

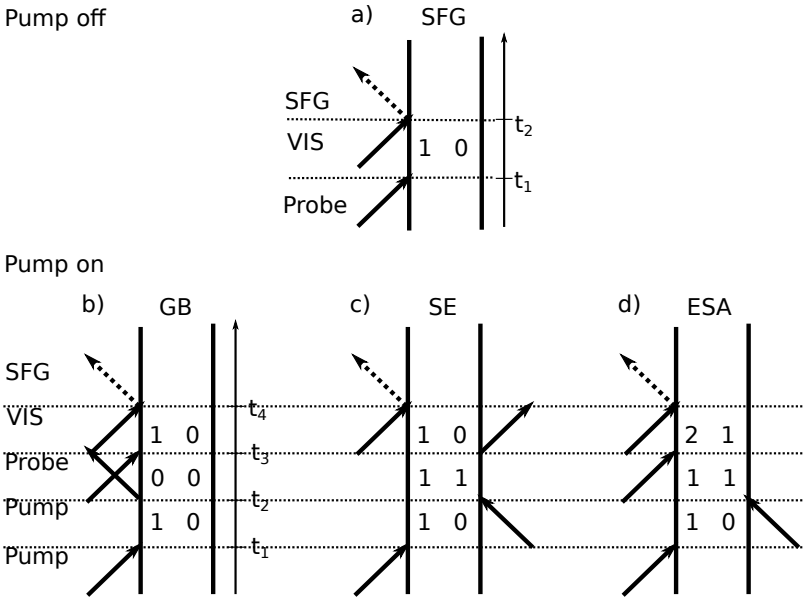

Figure 2.6: Double-sided Feynmandiagrams of pump-probe SFG. The diagramm of a) corresponds to an ordinary SFG experiment. b) describes ground state bleach (GB), c) stimulated emission (SE) and d) excited state absoprtion (ESA).

Figure 2.6 a) shows the diagram for ordinary SFG and corresponds to the unpumped state thereafter probing $P^{(2)}_{\text{pump off}}$. At t_1 the system interacts with an incoming IR pulse and the system is in the $|1\rangle\langle 0|$ state. This is called a coherence and the quantum mechanical source of polarization. The second interaction at t_2 with the visible pulse, generates a virtual state, that is not resonant with any vibrational mode. This

interaction generates SF light obeying the selection rules of subsection 1.2.2.
Figure 2.6 b)-d) shows the most significant diagrams with the pump laser on. The diagram of Figure 2.6 b) refers to ground state bleaching (GB), for simplicity often just called bleach. Here the first interaction with the pump pulse at t_1 causes a coherence, that is then removed by the second pump pulse interaction at t_2. Figure 2.6 c) describes stimulated emission (SE). For SE the first pump pulse interaction at t_1 creates a $|1\rangle\langle 0|$ coherence, but the second pump pulse interaction at t_2 creates a $|1\rangle\langle 1|$ population. The diagram of Figure 2.6 d) shows excited state absorption (ESA). In the case of ESA the probe pulse interaction at t_3 is different, because instead of a $|1\rangle\langle 0|$ coherence like in ordinary SFG, a $|2\rangle\langle 1|$ coherence is generated. Note that the ESA process has, compared with the GB and SE, a different sign, as the number of left side interactions is odd in the case of ESA, but even in the other cases. By changing the time between the arrival of the pump and the probe pulse, the time difference between t_2 and t_3 can be manipulated experimentally, and this allows to study the time evolution of the $|1\rangle\langle 1|$ population experimentally.
The diagrams of Figure 2.6 can be used to calculate the corresponding response functions, that are in turn responsible for the macroscopic polarizations $P^{(2)}$ and $P^{(4)}$.[51] Following the convention of ref[26] the macroscopic polarization is a function of the transition dipole moments (μ) and the electic field (E). In the ordinary SFG case e.g. pump laser off, one observes:

$$P^{(2)}_{\mathrm{SFG}} = P^{(2)}_{\text{pump off}} \propto -\mu_{01}\alpha_{01}E_{\mathrm{VIS}}E_{\mathrm{IR}} \tag{2.10}$$

Where E_{VIS} and E_{IR} are the incoming electric fields, μ_{01} is the transition dipole moment for the IR excitation between ground $|0\rangle$ and first vibrational state $|1\rangle$, i.e. the vibrational mode. Further $\alpha_{01} = \mu_{\mathrm{VIS}}\mu_{\mathrm{SFG}}$ as a combined term describing the interaction of VIS and SFG, also called the transition polarizability, characterizing an electronic process. To consider the case with a pump interaction, the total polarization is given by the summation of all four polarizations, described by the four diagrams of Figure 2.6. Thus

$$P^{(4)}_{\text{pump}} \propto P^{(4)}_{\mathrm{GB}} + P^{(4)}_{\mathrm{SE}} + P^{(4)}_{\mathrm{ESA}} + P^{(2)}_{\text{pump off}} \tag{2.11}$$

needs to be calculated. In Figure 2.6 one can see that the polarization for GB and SE is identical as it is given by:

$$P^{(4)}_{\mathrm{GB}} = P^{(4)}_{\mathrm{SE}} \propto \mu^2_{01}E^2_{\text{pump}}\mu_{01}\alpha_{01}E_{\mathrm{VIS}}E_{\mathrm{IR}} \tag{2.12}$$

with $\mu^2_{01}E^2_{\text{pump}}$ due to the two pump interactions. For ESA one obtains:

$$P^{(4)}_{\mathrm{ESA}} \propto -\mu^2_{01}E^2_{\text{pump}}\mu_{12}\alpha_{12}E_{\mathrm{VIS}}E_{\mathrm{IR}} \tag{2.13}$$

with μ_{12} as transition dipole moment for the IR probe transitions between first and second excited state and α_{12} the same for the electronic transition. Assuming an harmonic oscillator, for the vibrational as well as the electronic potential, the transition dipole moment has a relation of $\mu_{12} = \sqrt{2}\mu_{01}$ as well as $\alpha_{12} = \sqrt{2}\alpha_{01}$. If this is

inserted into Equation 2.13, the sum $P^{(4)}_{\mathrm{GB}} + P^{(4)}_{\mathrm{SE}} + P^{(4)}_{\mathrm{ESA}}$ would vanish, leaving us with no difference between the pumped and the unpumped case. However if the vibrational potential is anharmonic, the ESA is frequency shifted with respect to GB/SE, as the energy gap between the $|0\rangle \rightarrow |1\rangle$ transition is larger then the energy gap between the $|1\rangle \rightarrow |2\rangle$ transition.

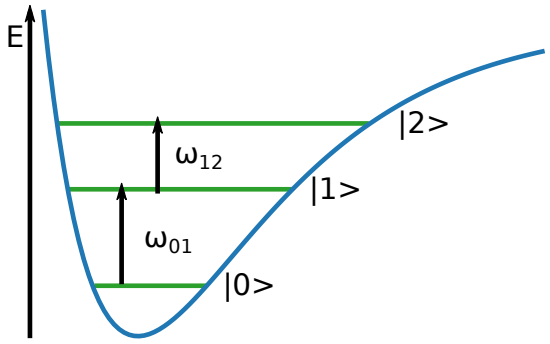

Figure 2.7: Morse potential as anharmonic oscillator model for e.g. water stretch vibrations. The $|0\rangle \rightarrow |1\rangle$ tansition has a larger energy gap then the $|1\rangle \rightarrow |2\rangle$ transiton. Thus excitation energy is smaller for ω_{12} then for ω_{01}.

This is shown in Figure 2.7 for the energy of the Eigenstates of the first three states of the anharmonic morse potential. Thus if ESA does not cancel with GB/SE, this, by itself, is already a strong indication for an underlying anharmonic potential. Further, it explains why two signals of opposite sign but similar intensity are expected for GB/SE and ESA. The stretch vibration of water is known to exhibit a strong anharmonicity.[52,53] This also means that the frequencies of ESA and GB/SE are well separated when studying the water stretch vibration.
During a pump-probe SFG experiment, the two intensities with and without the pump excitation are measured, based on an alternating shot to shot detection pattern. Each intensity (with and without the pump) is proportional to the square of the electric field generated by the nonlinear polarization. To obtain the measured intensities we need to calculate:

$$I_{\mathrm{SFG,pump\ off}} \propto \left| P^{(2)}_{\mathrm{pump\ off}} \right|^2$$
$$I_{\mathrm{SFG,pump}} \propto |P^{(4)}_{\mathrm{GB}} + P^{(4)}_{\mathrm{SE}} + P^{(4)}_{\mathrm{ESA}} + P^{(2)}_{\mathrm{pump\ off}}|^2$$

This expands into six cross and four square terms. However it can be simplified by assuming, as already stated, that 0-1 and 1-2 transition are well separated and do not overlap in frequency. Thus all cross terms containing both transitions will be zero e.g. $P^{(4)}_{\mathrm{ESA}} P^{(2)}_{\mathrm{pump\ off}} = 0$ and the difference signal with pump on and pump off is

$\Delta I_{\mathrm{SFG}} = I_{\mathrm{SFG,pump}} - I_{\mathrm{SFG,pump\ off}}$:

$$\Delta I_{\mathrm{SFG}} \propto |P^{(4)}_{\mathrm{ESA}}|^2 + 4|P^{(4)}_{\mathrm{GB}}|^2 + 4P^{(4)}_{\mathrm{GB}}P^{(2)}_{\mathrm{pump\ off}} \tag{2.14}$$

$$= (-\mu_{01}^2 E^2_{\mathrm{pump}}\mu_{12}\alpha_{12}E_{\mathrm{VIS}}E_{\mathrm{IR}})^2 \tag{2.15}$$

$$+ 4(\mu_{01}^2 E^2_{\mathrm{pump}}\mu_{01}\alpha_{01}E_{\mathrm{VIS}}E_{\mathrm{IR}})^2 \tag{2.16}$$

$$+ 4(\mu_{01}^2 E^2_{\mathrm{pump}}\mu_{01}\alpha_{01}E_{\mathrm{VIS}}E_{\mathrm{IR}})(-\mu_{01}\alpha_{01}E_{\mathrm{VIS}}E_{\mathrm{IR}}) \tag{2.17}$$

By substituting $\zeta = \mu_{01}\alpha_{01}E_{\mathrm{VIS}}E_{\mathrm{IR}}$, $\mu_{01}^2 E^2_{\mathrm{pump}} = \mu_{01}^2 I_{\mathrm{pump}}$, $\mu_{12} = \sqrt{2}\mu_{01}$ and $\alpha_{12} = \sqrt{2}\alpha_{01}$, this simplifies to:

$$\Delta I_{\mathrm{SFG}} \propto \underbrace{4(\mu_{01}^2 I_{\mathrm{pump}}\zeta)^2}_{I_{\mathrm{ESA}}} + \underbrace{4(\mu_{01}^2 I_{\mathrm{pump}}\zeta)^2 - 4\mu_{01}^2 I_{\mathrm{pump}}\zeta^2}_{I_{\mathrm{GB/SE}}} \tag{2.18}$$

Here one needs to note, that the first term corresponds to the intensity contribution from the ESA signal. Thus $I_{\mathrm{SFG,ESA}} \propto 4(\mu_{01}^2 I_{\mathrm{pump}}\zeta)^2$ while the last two terms correspond to the combined intensity of GB and SE. Therefore $I_{\mathrm{SFG,GB/SE}} \propto 4(\mu_{01}^2 I_{\mathrm{pump}}\zeta)^2 - 4\mu_{01}^2 I_{\mathrm{pump}}\zeta^2$
By taking the ratio of these two contributions, we can learn about there relative importance towards the complete signal intensity.

$$I_{\mathrm{SFG,ESA}}/I_{\mathrm{SFG,GB/SE}} = \frac{\mu_{01}^2 I_{\mathrm{pump}}}{\mu_{01}^2 I_{\mathrm{pump}} - 1} \tag{2.19}$$

Because typically $\mu_{01}^2 I_{\mathrm{pump}} < 1$, these two terms have opposite sign with e.g. $\mu_{01}^2 I_{\mathrm{pump}} = 0.1$ the ESA signal is 0.1, while the GB/SE signal is 0.9. This means the overall intensity is dominated by the $|1\rangle \rightarrow |0\rangle$ transition and one mainly observes GB/SE intensity and not ESA. The same can also be understood by noting:

$$\chi^{(2)}_{\mathrm{GB/SE}} \propto (N_0 - N_1); \quad \chi^{(2)}_{\mathrm{ESA}} \propto (N_1 - N_2) \tag{2.20}$$

where N_x is the population of the vibrational level x. Given that the pump beam can excite about 10 % of the oscillators into the first excited vibrational state, then $N_0 = 0.9$, $N_1 = 0.1$ and $N_2 = 0$. Defining an ordinary SFG intensity of I, we observe for $I_{\mathrm{GB/SE}}$ a reduced signal of $(1-(0.8^2))\mu\alpha I = 0.36\mu\alpha I$, assuming a transition dipole moment $\mu_{01} \equiv \mu$ and $\alpha_{01} \equiv \alpha$. For the I_{ESA} we expect $(\sqrt{2}\mu\sqrt{2}\alpha 0.1)^2 I = 0.04\mu\alpha I$ where $\mu_{12} = \sqrt{2}\mu_{01}$ and $\alpha_{12} = \sqrt{2}\alpha_{01}$ of the harmonic approximation is used. Thus the $I_{\mathrm{GB/SE}} : I_{\mathrm{ESA}}$ ratio is roughly $9:1$. Leaving the $I_{\mathrm{GB/SE}}$ signal and consequently the $|1\rangle \rightarrow |0\rangle$ the most significant contributor to the observed intensity.

2.1.2 Experimental Simplifications for Pump-Probe SFG

As discussed in subsection 2.1.1, the vibrational dynamics of interfacial water can be studied by means of PP-SFG spectroscopy. Here we focus on symmetric PP-SFG, where the pump laser and the probe laser have about the same central frequency. The

interested reader may be redirected to,[54] for experiments where pump and probe laser have different central frequencies. From an experimental point of view, GB, SE and ESA are challenging to separate, and the combined pumped state is treated as a single state. This leads to a simplified but often useful view on PP-SFG.

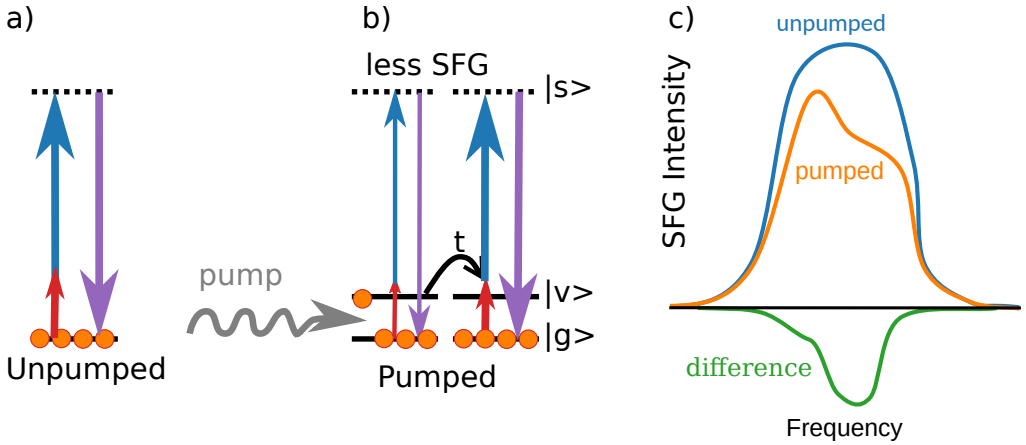

Figure 2.8: a) and b) Energy diagram of a pump-probe SFG experiment. c) Toy model of pump-probe SFG signals.

Figure 2.8 a) and b) shows the energy diagram of a PP-SFG experiment. Here two independent intensities, one for the unpumped and one for the pumped process, are recorded. As already mentioned, the unpumped process is equal to the ordinary SFG process described in Figure 2.1. However, the energy diagram of the pumped process is different. Here the pump beam (grey arrow) changes the population of the oscillators in the ground state, indicated by the orange dots. Due to the depletion of the ground state, the probe pulse, generating the SF signal, has a decreased likelihood of generating SF light. Thus the SF intensity of the pumped process is decreased in comparison with the unpumped process. By tuning the time delay between pump and probe pulse, one is able to study the lifetime of the excited vibrational state, as with increasing delay time, a greater fraction of the excited state population decays into the ground state. Figure 2.8 c) is a model, showing a possible pumped and unpumped SFG signal intensity as it could appear during an experiment for a fixed pump-probe time delay. Figure 2.8 c) makes clear that the pumped signal is reduced in comparison to the unpumped signal intensity. Furthermore, it shows that the quantity of interest is the difference or the ratio of the pumped and the unpumped signal, containing spectral as well as temporal information about the $|v\rangle$ state. In the following, I will explain the model used to phenomenologically describe the spectroscopic effects of the $|v\rangle \rightarrow |g\rangle$ transition.

2.1.3 Phenomenological Description with the Four-Level-Model

To describe the experimentally observed dynamics of the above mentioned $|v\rangle \rightarrow |g\rangle$ transition in water, assuming a single exponential decay is not sufficient. Instead,

the so-called four-level-model is used. It was initially used to describe pump-probe dynamics of bulk water.[55,56] Later it turned out that it can also be used to describe the interfacial vibrational dynamics of water.[57] To the best of the my knowledge, this model has always been solved numerically if used to describe SFG data. This thesis aids in the analysis of this model as it presents an analytical solution to the four-level-model previously not used in the field of SFG. This section is, therefore, part of the publication Deiseroth et al.[58]

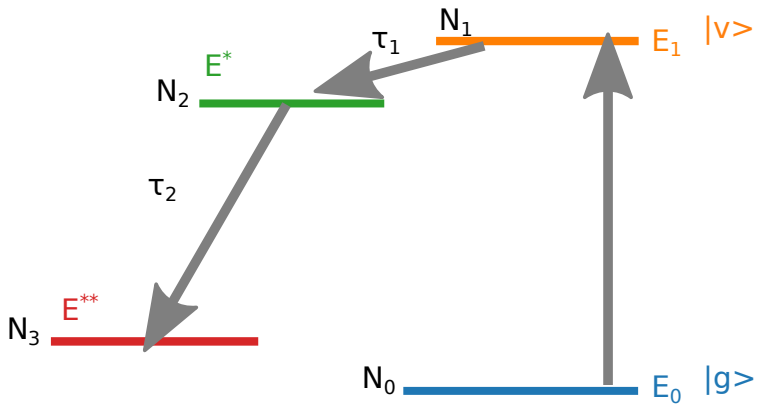

Figure 2.9: Energy level of the involved vibrational states. A pump pulse excites molecules from the ground level N_0 into N_1. With a lifetime of τ_1 the molecules decay into an intermediate state N_2 and after τ_2 into a long lived heated ground state N_3.

Figure 2.9 shows an energy level diagram of the four-level-model. A pump pulse excites a fraction of the molecules from the vibrational ground state N_0 into an excited state N_1. The excited molecules stay in N_1 for an average lifetime of τ_1 and decay via an intermediate state N_2 into the heated ground state N_3. Due to the absorption of the laser beam, the temperature of the system changes. In particular, the cooling of the system occurs at timescales much longer then the experiment resolves. Thus a stable heated ground state is a reasonable assumption to account for these temperature effects.[47,59,60] However note that experimental deviations from this assumption have been observed and effects due to long time delays are currently under investigation.[61] The model in Figure 2.9 can be described by a system of coupled first-order linear differential equations given in Equation 2.21 - Equation 2.24. N is the total number of oscillators, $N_i(t)$ with $i \in \{0,1,2,3\}$ denotes the number of oscillators at time t in state i and τ_i is the corresponding lifetime of the state N_i.

$$N_0(t) = N - N_1(t) - N_2(t) - N_3(t) \tag{2.21}$$

$$dN_1(t)/dt = -N_1(t)/\tau_1 \tag{2.22}$$

$$dN_2(t)/dt = N_1(t)/\tau_1 - N_2(t)/\tau_2 \tag{2.23}$$

$$dN_3(t)/dt = N_2(t)/\tau_2 \tag{2.24}$$

Typically a Gaussian-shaped excitation function is applied within Equation 2.22 and Equation 2.23 to account for the temporal width of the excitation pulse. This makes it impossible to solve the differential equation analytically. However, as shown below, if one first solves the differential equations and then convolves this solution with a Gaussian instrument response function, a purely analytical model function can be derived. This has the practical advantage of not needing a numerical differential equation solver upon fitting the data and thus leads to more robust fitting results.
The analytical solution to Equation 2.21 - 2.24 is given by the equations 2.25 - 2.28.

$$N_0(t) = N - N_1(t) - N_2(t) - N_3(t) \tag{2.25}$$

$$N_1(t) = N_1(0)e^{-t/\tau_1} \tag{2.26}$$

$$N_2(t) = \frac{1}{\tau_1/\tau_2 - 1}(e^{-t/\tau_1} - e^{-t/\tau_2})N_1(0) + e^{-t/\tau_2}N_2(0) \tag{2.27}$$

$$N_3(t) = \left(\frac{1 - e^{-t/\tau_1}}{1 - \tau_2/\tau_1} + \frac{e^{-t/\tau_2} - 1}{\tau_1/\tau_2 - 1}\right) N_0(0) + (1 - e^{-t/\tau_2})N_2(0) + N_3(0) \tag{2.28}$$

The pumping due to the probe pulse is negligible and therefore we assume $N_0(0) = N - n$, $N_1(0) = n$, $N_2(0) = 0$ and $N_3(0) = 0$ at initial time $t = 0$ with n the number of initially excited oscillators. This simplifies Equation 2.27 and Equation 2.28 because only their first terms deviate from 0. Assuming an instantaneous excitation pulse, the time dependent bleach $R_{SFG}(t)$ is modeled by the population of involved vibrational states as show in Equation 2.29.

$$R_{SFG}(t) \propto S(t, \tau_1, \tau_2, c) = (N_0(t) - N_1(t) + N_2(t) + cN_3(t))^2/N_0(0)^2 \tag{2.29}$$

This assumes the same spectral shape of the ground state $N_0(t)$ and the intermediate state $N_2(t)$ while R_{SFG} is reduced by the amount of oscillators in the first excited state $N_1(t)$. The scaling factor c accounts for the differences in the spectral shape of the heated ground state $N_3(t)$ in comparison with $N_0(t)$.
To account for the finite temporal width of the pump laser, Equation 2.29 must be convolved with the temporal profile of the excitation pulse resulting in Equation 2.30.

$$R_{SFG}(t) \propto S(t, \tau_1, \tau_2, c) \circledast P_{ext}(t) \tag{2.30}$$

Where $P_{ext}(t)$ denotes an arbitrary shaped excitation function and $\circledast$ a convolution. By assuming a Gaussian excitation profile with width σ at time μ and amplitude A, the convolution integral of Equation 2.30 can be solved analytically resulting in Equation 2.31

$$R_{SFG}(t) \propto S'(t, \tau_1, \tau_2, c, A, \sigma, \mu) = S(t, \tau_1, \tau_2, c) \circledast G(t, A, \sigma, \mu)^1 \tag{2.31}$$

[1] A reference implementation of the function can be found at https://github.com/deisi/bleach-models.

Out of the 6 parameters of Equation 2.31, 3 can be readily determined independently. The width σ and the temporal position μ of the excitation beam can be deduced from the measured cross-correlation of the three involved laser beams. Previous results from pump-probe IR measurements for bulk H_2O have indicated that τ_2 is 700 fs.[17,47,62] The free parameters are thus: The lifetime of the first excited state τ_1, the amplitude of the excitation A and the amplitude of the heat c. $S'(t, \tau_1, c, A)$ is then used as a model function for a least square fit to the measured $R_{SFG}(t)$ traces, and τ_1 is thus extracted as the lifetime of the initially excited vibrational state.

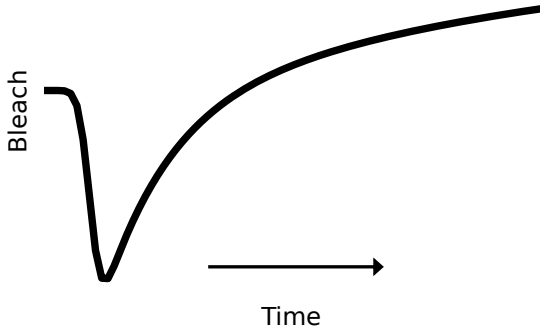

Figure 2.10: Trace calculated by the four-level-model. The slope of the left edge is determined by the width of the gaussian excitation function. The slope on the right side is dominated by the τ_1 and τ_2 lifetimes.

Figure 2.10 shows a calculated trace using Equation 2.31. For small delay times, the trace shows a fast decrease. Typically this decrease is dominated by the width of the Gaussian excitation function. Then the signal increases with lifetimes dominated by τ_1 and τ_2. The final amplitude depends on the value of the heat parameter c.
Note that the presented deviation of $R_{SFG}(t)$ is based on the ratio of pumped an unpumped population. This can be seen by the form of Equation 2.29, where the denominator is $N(0)$ (typical equal to 1). In Equation 2.14 the difference of pumped and unpumped SFG intensity is used. However, the result of Equation 2.31 can be transformed for difference based pump-probe data. Assuming g is a normalized Gaussian function, f is an arbitrary function and the population at time zero is set to $N(0) = 1$. We obtain:

$$g \circledast (f - 1) = (g \circledast f) - (g \circledast 1) = (g \circledast f) - 1 \int g dt \tag{2.32}$$

The tailing integral $\int g dt$ becomes 1 if g is a normalized Gaussian function, what is the case here. Thus for difference-based results, the same function can be used, except it needs to be subtracted by 1.

2.2 Pump-Probe Sum Frequency Generation Setup

The static and PP-SFG experiments were performed using a custom build tabletop PP-SFG setup. In the following the fundamental optical elements of the setup will be described.

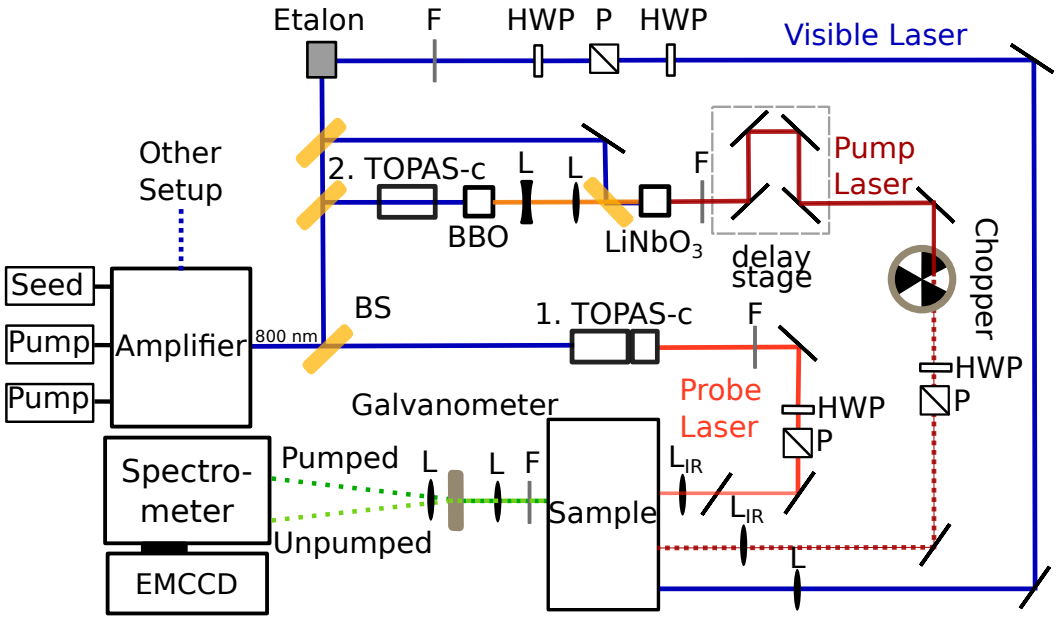

Figure 2.11: Sketch of a pump-probe SFG setup. Abbreviations are beam splitter (BS), Filter (F), half-wave plate (HWP), polarizer (P), lens (L), charged coupled device (CCD), barium borate crystal (BBO), lithium niobate crystal ($LiNbO_3$). For the sake of clarity, alignment and optimization related optical elements are not shown, elements are not drawn to scale.

A simplified sketch of the PP-SFG setup is shown in Figure 2.11. Laser pulses are produced by a seed oscillator (Mai Tai, Spectra Physics) with a central wavelength of 800 nm and roughly 50 nm bandwidth. The Spitfire Ace amplifier is pumped by two Empowers (22 mJ pulse energy at a central wavelength of 527 nm) and has a power output of about 10 W and a pulse length of 40 fs with a repetition rate of 1 kHz. The output of the amplifier is split by several beam splitter (BS).
Roughly 3 Watts are sent into a Topas-C with a DFG stage and a tunable output wavelength of between 2 μm and 10 μm. The output pulse energy of the Topas-C varies with the output frequency. Typically about 40 μJ at a center frequency of 2500 cm^{-1} after an IR bandpass filter (F). A half-wave plate (HWP) and a polarizer (P) are used to guarantee p-polarization at the sample and the angle of incidence on the sample is 40° with respect to the surface normal. In an ordinary SFG experiment, this beam is called IR beam due to its frequency range, while in a pump-probe experiment, this beam is called probe.
Less then 1 W of the broad 800 nm laser light is sent into an etalon , and depending

on the angle of the etalon with respect to the beam axis, a specific central frequency of the visible is selected. Here a central wavelength of 812 nm is used. The exact frequency is needed for calibration of the center SFG frequency, but has no further influence on the experiment as the visible laser frequency is far from any resonances of the studied samples. A combination of a half-wave plate, a polarizer, and an additional half-wave plate is used to control the polarization of the visible laser at the sample (s-polarized), as well as reduce the power of the visible beam. This is useful for heat-sensitive samples, such as lipid monolayers, that can be burned or spatially moved out of the focus by the laser beam itself.[63] The incident angle of the visible laser with respect to the surface normal is 70°. At the sample, a pulse energy of up to 20 μJ is used.

To generate the narrowband pump beam at $\approx$ 2000 nm the idler output of a second Topas-C is sent into a BBO crystal to generate $\approx$1000 nm IR pulses (green in Figure 2.11). These pulses are overlapped with 800 nm pulses within a $LiNbO_3$ crystal to generate narrowband pump pulses via a DFG process (p-polarized, $\approx 90\,cm^{-1}$ full width at half maximum, fwhm). By tuning the frequency of the doubled idler and adjusting the phase-matching condition at the $LiNbO_3$ crystal, the infrared pump laser can be tuned between $2350\,cm^{-1}$ and $2750\,cm^{-1}$. The maximum pulse energy at the sample varies from 5 μJ to 10 μJ, depending on the central pump frequency. The angle of incidence with respect to the surface normal is 55° and a copper blocks every second pump pulse reducing the effective pump pulse rate to 500 Hz.

By overlapping probe and visible laser pulses at the sample, SFG light is produced at a central frequency of 674 nm and sent into a Acton SpectraPro-300i spectrometer and detected using an Andor Newton DU971 P-BV electron-multiplied charged coupled device (EMCCD) camera. The integration time of a single spectrum is between 10 s and 200 s depending on the specific sample signal intensity and laser power.

During a pump-probe SFG measurement, multiple nonlinear optical effects take place. Most of these processes are not of interest during a PP-SFG experiment and are suppressed using spatial and spectral filtering. However, the sum signal of pump-probe-visible (PPV) turns out to be useful. It is emitted at almost the same angle as the SFG light, but due to its shift in central frequency (570 nm) it can be suppressed by the spectrometer. The PPV signal is a bulk allowed $\chi^{(3)}$ signal and, therefore, much stronger than the bleach of SFG. Because the requirements for PPV and bleach are the same, the PPV signal can be used to align for optimal bleach conditions. PPV further allows measuring the cross-correlation of the setup. This is done by changing the delay between pump-probe using the delay stage (see Figure 2.11) and recording the PPV signal as a function of pump-probe time delay. This requires a sample with instantaneous response to the changes induced by the pump, probe and visible laser beams. Therefore typically gold is used to measure the cross-correlation.

2.2.1 Analysis of the Instrument Response Function

With PP-SFG setup, it is possible to estimate the temporal shape of the instrument response function. This is possible because the limiting factor for the instrument

response function is the pulse duration of the individual beams. The exact pulse duration of pump, probe and vis beam individually is challenging to measure and would require multiple autocorrelation measurements. However for PP-SFG experiment this is not needed. Instead, the time dependency of the convolution of the pump pulse with the SFG of the probe and vis beam is of interest. This time dependency is proportional to the time dependency of the bulk sensitive $\chi^{(3)}$ signal, occurring at the sum frequency of the pump, probe, and vis beam. Here this signal occurs at a central wavelength of about 575 nm depending on the specific central frequencies of the used beams. By recording the integrated intensity of this signal as a function of pump-probe time delay, the temporal width of the instrument response function can be estimated. In the following, this measurement is called a cross-correlation scan, and its width is used as an estimator for the instrument response function. Prior to each pump-probe experiment, the cross-correlation is measured and fitted with a Gaussian function to determine the width. The width is typically less then 200 fs (see Figure 2.12) and varies slightly with the specific central frequency of the pump and probe beam, as well as with the general alignment of the setup. A careful inspection of Figure 2.12 reveals, that the cross-correlation is not strictly of Gaussian shape. The visible asymmetry originates from the optical elements of the setup, and, in particular, the etalon. However, this asymmetry will not be further considered.

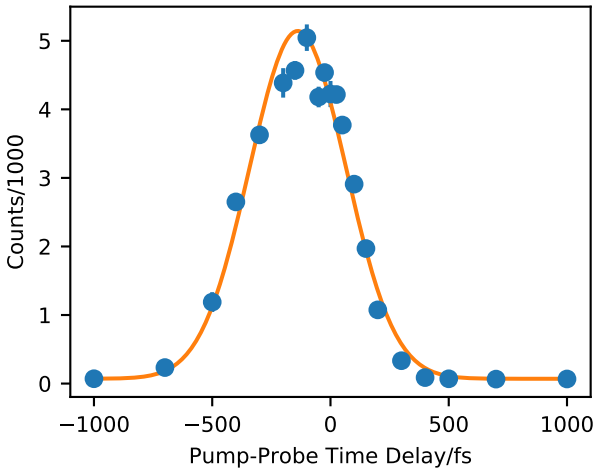

Figure 2.12: Cross-Correlation of Pump-Probe and visible as a function of pump-probe time delay. The cross-correlation is fitted with a Gaussian and used to approximate the system response function of the setup.

2.3 Analyzing Pump-Probe SFG Data

Throughout the course of this thesis, a substantial amount of python code aiding in the analysis of pump-probe SFG data was written. This python code can be found at https://github.com/deisi/SFG2D. Explaining the analysis package is out of the

scope of this thesis, but the packages provide:

- Modules to import various spectroscopic file formats
- Abstraction classes for background subtraction and normalization
- Methods to analyze static, phase-resolved, pump-probe as well as 2D-SFG data.
- Module with fitting classes. In particular the four-level-model
- Visualization functions

3 Regulating Heterogeneous Ice Nucleation Efficiency of Mica with Ions

Part of this chapter has been submitted to Journal of the American Chemical Society and is at the time of writing under revision.[64] The submission contains the abstract, the introduction as well the ice nucleation measurements, the SFG measurments and the results.

3.1 Abstract

Heterogeneous ice nucleation (HIN) is ubiquitous in numerous environmental and biological processes. In nature, HIN triggered by mineral aerosols can have a significant impact on the regional atmosphere and climate. Mineral surfaces typically expose various ions. However, the dependence of HIN on the nature of the mineral surface ions is still largely unexplored. By taking advantage of the unique property that the K^+ on the atomically flat (001) surface of muscovite mica (a prototype model for the surface of mineral aerosols) can be facilely replaced by different cations through ion exchange, we investigate ion-specific effects on HIN. The experiments show that the surface (001) of H^+-exchanged mica displays markedly higher HIN efficiencies than that of Na-/K-mica. In other words, the HIN efficiencies strongly depend on the characteristics of the cations embedded on the mica surface. Vibrational sum-frequency generation spectroscopy reveals that the H-mica induces substantially less orientation ordering, compared to the Na-/K-mica, within the contact water layer at the interface.

3.2 Introduction

Heterogeneous ice nucleation (HIN) is widely observed in a variety of environmental and biological processes. A better understanding of the HIN underlying mechanisms is important, for example, to develop improved models of cloud formation.[11,65–67] However, predicting and tuning of HIN is still very challenging. In part due to the lack of understanding molecular-level mechanisms of HIN.[68,69] As a quantitative measure, Koop et al. introduced water activity (i.e., the ratio of the water vapor pressure of the solution and of pure water under the same conditions) as a determinant for homogeneous ice nucleation in aqueous solution.[70,71] Naturally ice nucleation often

occurs via HIN on e.g. the surface of mineral aerosols. These mineral aerosols are embedded with various types of ions and are key to the formation of clouds and ice nuclei.[72–77] Many studies have focused on the impact of mineral aerosols with different ions on ice nucleation and conflicting conclusions exist due to the complexity of the surface of mineral aerosols.[12,78–86] Kumar and coworkers found that the HIN efficiencies of even the same feldspars were distinct in the solution of NH_3 (NH_4^+) and Na_2SO_4, possibly due to the ion exchange and/or adsorption of ions on the feldspars' surfaces.[66,75]

While the role of water has been intensely studied, direct experimental studies of the effect of ions on interfacial water and on the HIN efficiency are crucial to achieve an improved understanding of HIN tuning. In this study, muscovite mica surfaces with different cations were examined in order to establish a correlation between the ion specificity of interfacial water, and the impact of ion specificity on HIN. More importantly, the cation K^+on the mica surface can be exchanged with other cations.[87,88] Our measurements show that the HIN efficiency, measured by the ice nucleation temperature (TH) is sensitively dependent on the cations on the mica surface. The mica surface with atop H^+-exchanged (H-mica) displays the highest HIN efficiency, while mica surface with atop Na^+ (Na-mica) has the lowest efficiency in promoting ice nucleation among mica surfaces with various cations. Vibrational sum-frequency generation (SFG) spectroscopy analysis reveals that the H-mica has the least oriented interfacial water. In contrast, the Na-mica has the most oriented interfacial water.

3.3 Molecular Structure of Muscovite

The molecular structure of muscovite mica is shown in Figure 3.1, with layers of OH groups highlighted in color.

Figure 3.1 a) shows the side view of two layers of muscovite mica with labeled 1-OH^1, 1-OH^2, 2-OH^1 and 2-OH^2 groups and the connecting K^+ layer in the center. The side view of the molecular structure of muscovite mica indicates two layers of tetrahedral SiO_4 sheets sandwiching one octahedral aluminum layer. The substitution of Si^{4+} by Al^{3+} in the SiO_4 sheet leads to an intrinsic negative charge of mica surfaces, which are neutralized by electrostatically bound interlayer K^+.[90] Mica can be cleaved atomically flat along the K^+ layer and the outermost K^+ layer can be exchanged with ions, by flowing or immersing mica into ionic solutions to obtain Na-Mica, H-Mica, Cs-Mica, K-Mica or Rb-Mica.[31,88,91–94] Figure 3.1 b) shows the top view of the mica crystal, with the same color highlighting of the OH groups, showing the rotational orientation of the OH groups. The OH groups of 1-OH^1 and 1-OH^2 have a 180° back to back symmetry. The same back to back symmetry is found in the second mica layer (2-OH^1 and 2-OH^2) but rotated by an angle of about 108° relative to the 1-OH^1 layer.

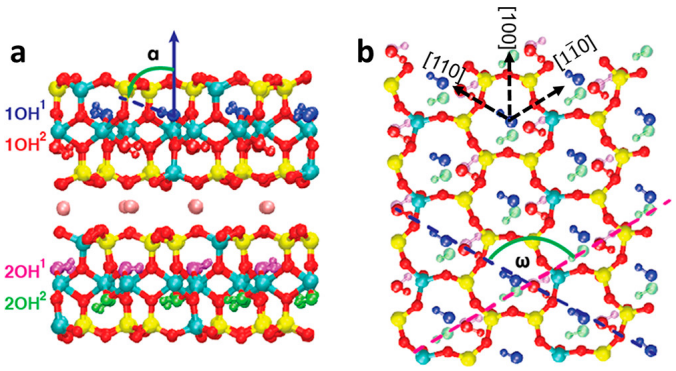

Figure 3.1: a) side view of the molecular structure of two layers of muscovite mica. The OH groups are colored according to their relative surface position. The layers of OH groups are labeled in order with 1-OH^1, 1-OH^2, 2-OH^1 and 2-OH^2. b) top view of the outermost mica layer. The orientation of the deeper OH groups is highlighted. Reprinted with permission from.[89] Copyright 2019 American Chemical Society

3.4 Mica XPS Data to confirm ion exchange

To confirm the ion exchange on the mica surface, XPS spectra on various ion-exchanged mica surfaces were measured. XPS spectra in the 750 eV-710 eV, 1090 eV-1050 eV, and 215 eV-180 eV energy region indicative of the Cs 2p, the Na 1s and the Cl 2p orbital binding energy, are shown in Figure 3.2 and Figure 3.3. Note that it is not trivially possible to confirm the exchange of H^+ with XPS. The samples exposed to ionic solutions were rinsed with water prior to vacuuming and cleaved before the first contact with ionic solutions.

Figure 3.2 shows XPS spectra of mica surfaces after exposure to different ionic solutions. Different colors in the same panel denote different positions on the same sample. Panel a) to c) show the XPS spectra at the Cs 3d orbital binding energy region. a) of a freshly cleaved mica sample, b) a sample exposed to 0.5 M CsCl for 30 min and c) a sample first exposed to 0.5 M CsCl for 30 min and subsequently exposed to 0.5 M KCl for 30 min. Note that the shift in the red spectrum of panel b) is most likely due to space charge effects on the insulating mica sample, induced by the neutralizer of the XPS setup.[95] Panel d) to f) of Figure 3.2 show XPS spectra in the orbital binding energy region of the Na 1s orbital. d) of a freshly cleaved mica sample, e) of a sample exposed to 0.5 M NaCl for 30 min and f) exposed to 0.5 M NaCl for 30 min and subsequently to 0.5 M KCl for the same amount of time.

The spectra of Figure 3.2 confirm that Cs as well as Na atoms attach to the surface and that KCl is sufficient to remove Cs and Na from the surface.[88] In the case of Na one can notice that even the cleaved sample shows a significant amount of Na atoms at the surface. As this sample was never exposed to Na specifically, we assume a residual Na contamination within the samples themselves as mica is mined and not produced synthetically.[96]

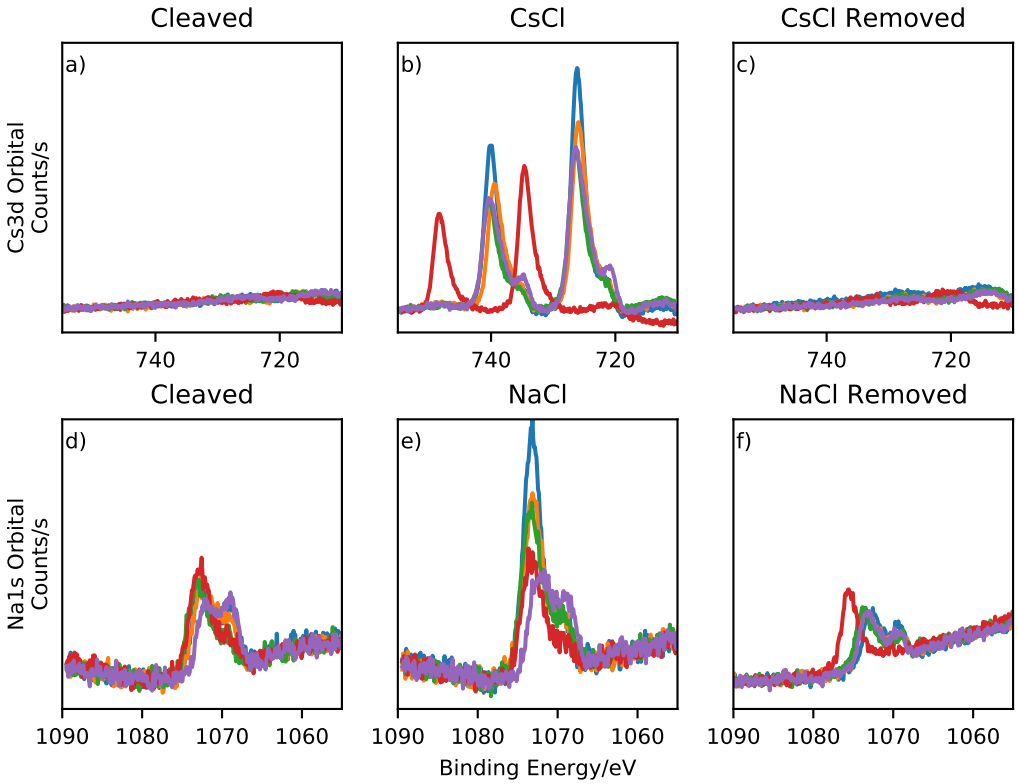

Figure 3.2: XPS spectra of ion exchanged mica surfaces. Panel a) to c) show the Cs3d orbital binding energy region. Surface near Cs atoms show two peaks at about 740 eV to 720 eV with a 1/3 to 2/3 area ratio. Panel d) to f) shows the Na1s orbital binding energy region. Surface near Na atoms show a single peak at about 1075 eV. The shoulders at 1070 eV, 730 eV and 720 eV as well as the shifted red spectrum in d) are most likely an artifact of the neutralizer.

The Na peak in panel e) shows intensity fluctuations of about 50 % throughout the same sample. As this behavior was recorded for several samples with contact to NaCl, we conclude that Na is inhomogeneous distributed at the mica surface with a coverage of about 50 %.

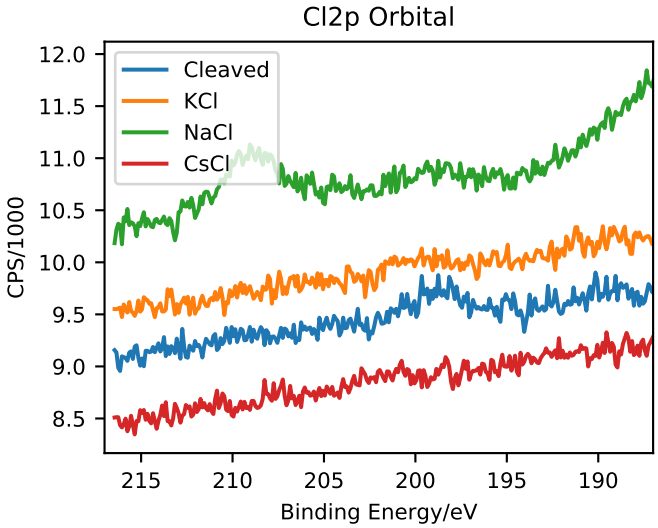

Figure 3.3: XPS spectra of 4 different mica samples. Surface near Cl atoms would show two peaks at 198.6 eV and 200.2 eV with a respective 2/3 and 1/3 area ratio.

Figure 3.3 shows XPS spectra of the Cl2p orbital binding energy region on freshly cleaved mica and mica samples exposed to KCl, NaCl, and CsCl. Surface near Cl atoms would show two peaks at 198.6 eV and 200.2 eV with a 2/3 to 1/3 area ratio respectively. Considering the neutralizer as systematic uncertainty of the measurement, a 1.6 eV energy splitting between the two peaks needs to hold. Thus the two peaks visible in the green NaCl measurement at 209 eV and 198 eV with there 11 eV splitting can not originate from Cl. The 198 eV peak visible in both the NaCl (green) and the cleaved (blue) measurement could match to the 198.6 eV peak of the Cl2p orbital, given that the weaker 200.2 eV peak stays below the detection threshold. However, the result would then be that also the cleaved mica sample contains a similar amount of near-surface Cl atoms. We thus conclude that there is no significant amount of Cl left on the surface after rinsing during the ion exchange process.

3.5 Ice Nucleation Measurements

The ice nucleation temperature (TH) measurements were performed by Shenglin Jin and Jianjun Wang and are reproduced here with permission.
Figure 3.4 shows the effect of mica surface cations on TH and thus the HIN efficiency. First, the mica surface is dried by flushing nitrogen and then water droplets of 0.1 μl are

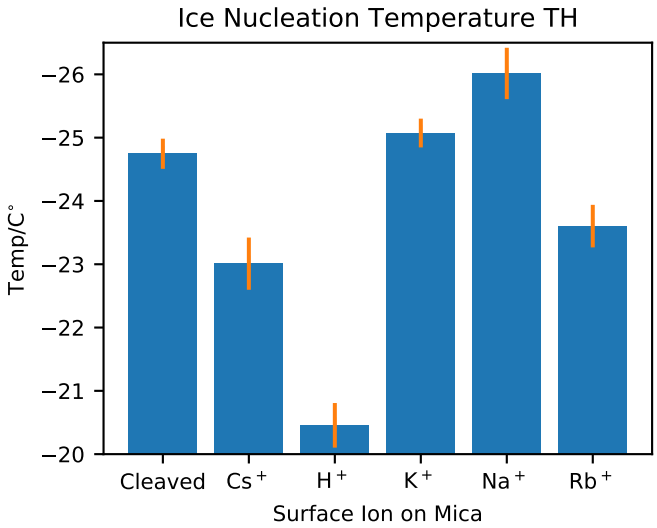

Figure 3.4: Ice nucleation temperature measurement of droplets on ion exchanged mica. H^+ exchanged mica exhibits highest ice nucleation temperature (−20 °C), while Na^+ exhibits lowest ice nucleation temperature (−26 °C). Replotted from[64] with permission.

placed on top of the mica samples. The samples are then installed in a temperature-controlled closed sample cell and cooled down at a constant cooling rate of 5 °C/min. The effect of cooling rate is studied in detail in the publication.[64] The freezing of the water droplets is monitored with a high-speed camera connected to an optical microscope. As shown in Figure 3.4, the ice nucleation temperature TH of water droplets on the surface of H-mica is ca. −20 °C, whereas it is ca −26 °C on Na-mica. The order of TH on the mica surfaces with cations is H-mica > Cs-mica > Rb-mica > K-mica > Na-mica. The mica surface with H^+ exhibits a substantially higher average TH than those with other alkali cations. These results indicate that the TH depends on the type of cation on the mica surfaces. However, the molecular mechanism causing these differences in HIN efficiency remains unclear. E.g., it could be, that water orientation and structure are controlling factors of the HIN efficiency. Therefore we use SFG to study the interfacial structure of the cation exchanged mica-water interface.

3.6 Causes for Sample to Sample Variations

By measuring the SFG response from the mica-water interface, it is possible to obtain information on the molecular structure of the mica-water interface. Because water absorbs the IR laser beam of the SFG setup, the experiment was performed in the so-called buried configuration, shown in Figure 3.5, with all laser beams passing through the mica sample and the SFG light detected in reflection geometry.
To verify that IR, VIS and SFG laser beams pass through the mica sample, IR and

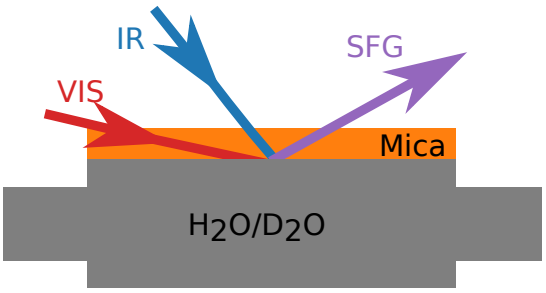

Figure 3.5: Beamgeometry for the mica-water SFG experiments. All three laser beams, IR, VIS and SFG pass through the mica sample.

VIS-transmission spectra of a mica sample were measured. The transmission spectra and the relevant frequency and wavelength regions are denoted in Figure 3.6.

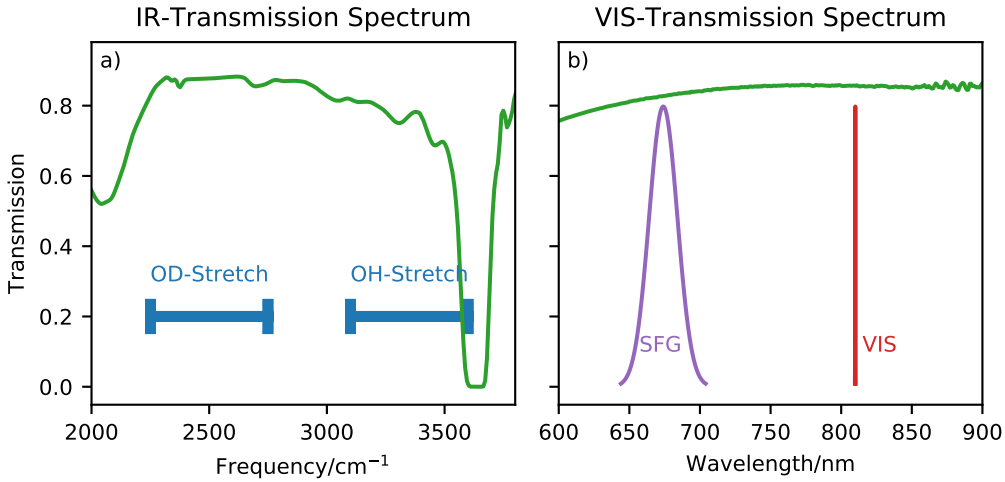

Figure 3.6: IR- and VIS-transmission spectra of a mica sample. a) is the IR-Tranmission spectrum, with the transmittance in green and the OH-stretch and OD-stretch resonances marked with blue bars. b) transmittance of the same mica sample in the wavelength region of the VIS and SFG laser beam.

Figure 3.6 a) shows the IR-transmission spectrum of a 0.18 mm ± 0.03 mm thick mica sheet in green. The blue bars labeled OH-stretch and OD-stretch, mark the relevant region of the stretch vibrations, respectively. The IR-transmission spectrum shows a strong absorption above 3500 cm^{-1}. This absorption is known to originate from the hydroxyl groups within the lattice structure and is the reason for the spectral cutoff in Figure 3.7 at 3500 cm^{-1}.[89] Throughout the 3500 cm^{-1} to 2300 cm^{-1} region, where primarily the OD-stretch and the OH-stretch vibrations are resonant, the IR-transmission spectrum is mostly flat, with a transmittance of about 80 %. Below

2300 cm^{-1} another absorption dip in the IR-transmission spectrum of mica appears. Figure 3.6 b) shows a VIS-transmission spectrum of the same mica sheet. The VIS beam of the SFG experiment has a central wavelength of about 810 nm with a bandwidth of less than 1 nm. The SFG light has a central wavelength of about 674 nm with a bandwidth of more than 20 nm. In both, the spectral region of the SFG signal and the VIS laser beam, the transmittance of the mica sample is flat with a transmittance of about 80 %. Thus the transmission spectra of Figure 3.6 confirm that the buried geometry of Figure 3.5 is suitable for detecting SFG light from the mica-water interface.
#Proof that the signal is from mica-h2o and not mica-d2o To exclude the mica-air interface as the primary source of the SFG signal, an isotopic exchange experiment was performed. Here the SFG spectrum of the mica-H_2O interface with the central IR laser beam frequency resonant to the OH-stretch vibration of H_2O is compared to the SFG spectrum of the mica-D_2O interface at the same central IR laser beam frequency.

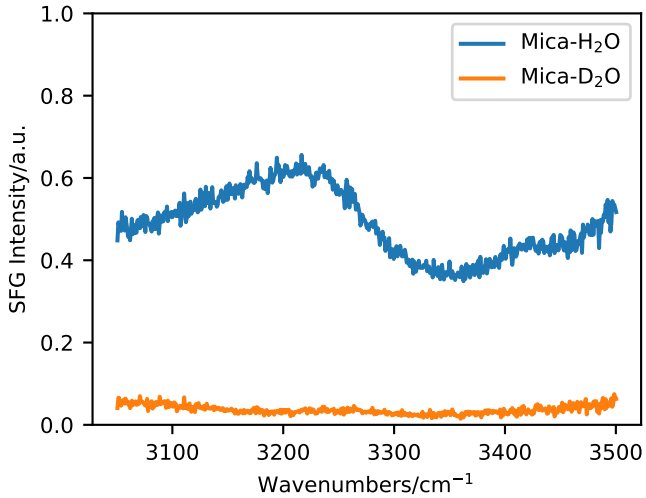

Figure 3.7: SFG intensity of mica-D_2O in comparison with mica-H_2O in the OH stretch region. The signal of the bonded region from 3100 cm^{-1} to 3500 cm^{-1} vanishes up on isotopic dilution.

The spectra of the isotopic exchange experiment are shown in Figure 3.7. As expected, the SFG intensity from the mica-H_2O interface (blue) is significantly larger than the SFG signal from the mica-D_2O interface (orange). This excludes the mica-air interface as the primary SFG signal source and leaves the mica-liquid interface as the most likely source of SFG signal.
During the SFG experiments, it became clear that the positioning of the mica sample has a significant impact on the mica-water SFG spectrum. Thus SFG spectra as a function of sample rotation were measured.
Figure 3.8 a) shows three SFG spectra of the same mica-D_2O sample at three different

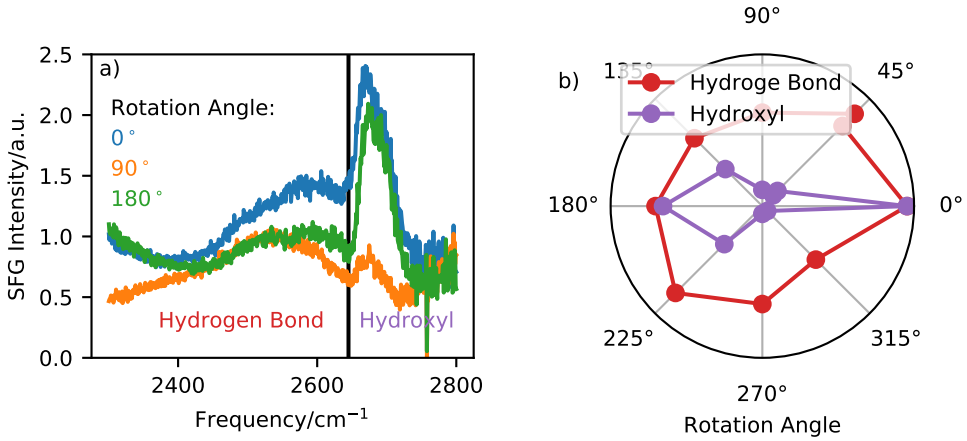

Figure 3.8: a) exemplary spectra of the same mica-water sample at three different rotation angles. b) Integrated SFG intensity for the hydrogen-bonded region ($2300\,\mathrm{cm}^{-1}$ – $2630\,\mathrm{cm}^{-1}$) and the hydroxyl region ($2630\,\mathrm{cm}^{-1}$ – $2750\,\mathrm{cm}^{-1}$) as a function of the rotation angle.

rotation angles. The rotation angle is defined with respect to the plane of incidence of the VIS and IR laser beam. The spectra in Figure 3.8 a) are separated into two regions, the hydrogen-bonded region from 2300 to $2630\,\mathrm{cm}^{-1}$ and the hydroxyl region from $2630\,\mathrm{cm}^{-1}$ to $2750\,\mathrm{cm}^{-1}$. The 0° rotation angle is calibrated by the maximum integrated SFG intensity of the hydroxyl region. The spectra of Figure 3.8 a) clearly show rotation angle-dependent SFG intensities. Figure 3.8 a) makes clear, that primarily the hydroxyl region is affected by the rotation angle. Figure 3.8 b) is a polar-plot of the integrated SFG intensity of the hydrogen-bonded and the hydroxyl region, respectively, where the distance from the origin corresponds to the integrated SFG intensity. Figure 3.8 b) shows a strong rotational dependency for the hydroxyl region (asymmetric shape) and a substantially smaller effect on the hydrogen-bonded region (round shape).

By looking at the crystal structure of the muscovite mica itself, (Figure 3.1) the angle dependency of Figure 3.8 can be understood. The hydroxyl signal originates primarily from the OH hydroxyl groups of the mica itself. In total four layers with OH groups labeled, 1-OH^1, 1-OH^2, 2-OH^1 and 2-OH^2 in Figure 3.8, are responsible for the hydroxyl Signal. The outermost 1-OH^1 and 1-OH^2 layers have a 180° orientation, generating the 180° symmetry of Figure 3.8. The two deeper layers 2-OH^1 and 2-OH^2 are rotated by about 105° relative to there outer most counter layer 1-OH^1 and 1-OH^2 respectively. Thus a second and a third maximum at about 105° and 285° are expected. Figure 3.8 b) clearly shows SFG signals from 1-OH^1 and 1-OH^2 layer at 0° and 180°. The signals from 2-OH^1 and 2-OH^2 are not clearly visible. Both maxima at 135° and 275° are candidates for the 2-OH^1 signal, depending on a left- or right-handed crystal symmetry. However, in either case, the signal at 285° or 75° expected from 2-OH^2 is

missing. Given the rough 45° sampling steps used here, the 2-OH[2] signal could very well be undetected. The effect of the muscovite mica hydroxyl groups on the SFG signal has been studied in details by Tuladhar et al.[89] From these results, it is clear that the crystal structure of the muscovite mica itself has an impact on the observed mica-water SFG spectrum and needs to be accounted for.
To further study the reproducibility of the SFG spectrum from the mica-water interface, we turn towards Figure 3.9. Here the SFG spectra from three separate mica-water interfaces are shown.

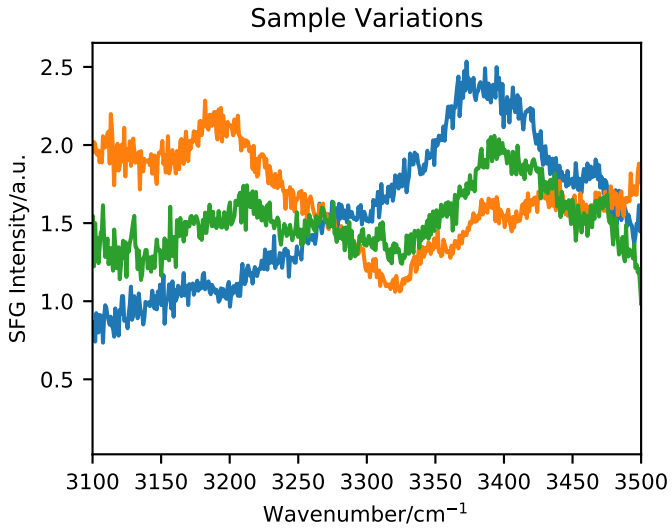

Figure 3.9: Three SFG spectra in the OH-stretch vibrational region for three different mica-water interfaces at arbitrary rotational angles. The spectra show significant differences, in particular the variations around 3100 cm^{-1} to 3250 cm^{-1} can not be explained by rotational effects.

The signal between 3000 cm^{-1} and 3550 cm^{-1} originates primarily from the OH stretch vibrations of water at the mica-water interface, with clear spectral differences between the samples. The samples are positioned with an arbitrary rotation, and the above mentioned rotational effects could cause some sample variations. Further, the samples have a thickness variance of 0.15 mm - 0.21 mm likely causing a constant SFG intensity offset. An additional source of uncertainty is the presence of small cracks within the mica sheets. The adhesion force of the K layers of mica is relatively weak, allowing for easy sample cleaving, but also increasing the likelihood of crystal defects along the K plains.[97,98] As the mica samples are relatively thin, interference of multiple SFG signal reflections could cause variations as well.[99] Overall we see that a set of systematic uncertainties makes the investigation of the mica-water interface difficult.

3.7 SFG on Mica-Water Interface

The main objective here is to investigate the impact of mica surface ion exchange on the mica-water interface. Thus the observations and analysis of sample-to-variations above lead to a systematic measurement and analysis scheme described in the following.
By using a flow cell to perform the ion exchange on the mica surface, the need for sample replacing between ion exchange steps is removed. Instead, samples are exchanged only to obtain additional statistical information.

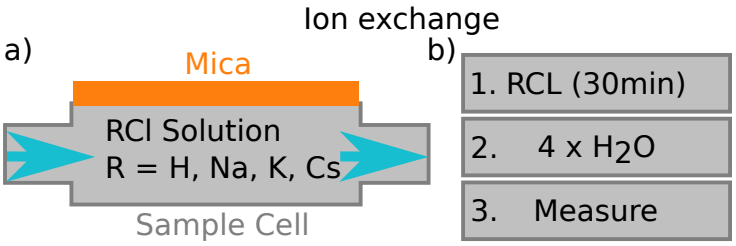

Figure 3.10: a) the flow cell configuration allows the ion exchange by flowing RCl solutions. b) the flowing sequence of a single ion exchange.

Figure 3.10 a) shows the flow cell design with the mica interface atop the flow cell. By flowing solutions of HCl, NaCl, KCl or CsCl, the surface cation of mica can be exchanged. Figure 3.10 b) depicts the flowing procedure used to obtain a single SFG spectrum from a R^+ terminated mica-water interface. At first, the surface cation is exchanged by flowing RCL solution. In a second step, pure water is flown to clean the sample cell of residual RCl solution and in a third step the SFG spectrum of the mica-water interface is measured.
As mica is naturally terminated with K^+ ions, flowing KCl can be considered as cleaning the surface of exchange ions. Therefore each sample was first cleaned by flowing KCl solution, and the initial K-mica SFG spectrum was measured. Then the surface ion-exchange was performed according to Figure 3.10 b), and the R-mica SFG spectrum was recorded. After flowing KCl solution a second time, a final K-mica SFG spectrum of the cleaned K-mica-water interface was measured. By comparing relative intensity changes of these three spectra, the influence of the surface ions on the mica-water SFG spectrum could be inferred.
Figure 3.11 shows SFG spectra of the mica-water interface of three different mica samples, with three different surface ions attached to the mica interface. Each panel shows an initial K-mica spectrum in blue, and an Na-mica, Cs-Mica or H-mica in orange. In green, a final K-mica spectrum after cleaning is shown. Note that the difference in the spectral shape of the initial K-mica is not due to the attached ions, but rather due to variations of the mica samples themselves. Figure 3.11 a) shows an enhancement of roughly a factor of 2 in the SFG intensity of the mica-water signal if Na^+ ions are attached to the mica-surface. Figure 3.11 b) shows, within the experimental uncertainty, the same spectrum in the case of Cs^+ and K^+ terminated mica-water interface. Figure 3.11 c) shows the influence of H^+ relative to K^+ and

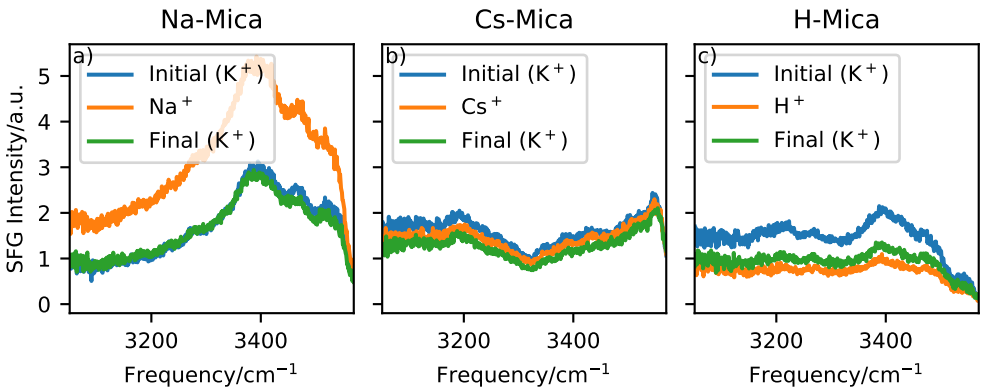

Figure 3.11: SFG Spectra of the mica-water interface of three different samples terminated with Na^+, Cs^+ and H^+ respectively. Note the difference in spectral shapes due to sample to sample variations. a) Na-Mica shows a signal enhancement of a factor of two compared to K-Mica. b) Cs-Mica spectrum shows no significant difference to the spectrum of K-Mica. c) H-Mica has a by about 50 % reduced SFG intensity compared to the initial K-Mica signal intensity.

one can see a significant drop in the SFG intensity upon attaching H^+ at the surface. However, note that K^+ after flowing of HCl does not recover back to its original K^+ spectrum, but rather has a lasting decreasing impact on the SFG intensity. To study the effect of the mica surface ion on the intensity of the mica-water SFG intensity in detail, the SFG intensity of Figure 3.11 are integrated over the shown spectral range, and the experiment is repeated for three to four independent measurement sets with different mica samples.

Figure 3.12 shows the integrated SFG intensities normalized to the initial K^+ terminated mica spectra. Sequential measurement sets are of the same color, and surface cation content is denoted on the x-axis. Arrows guide the eye towards the significant trend. In the case of Na^+, one can see two distinct cases. In one case, the signal intensity increases almost by a factor of two and in the other by only about 20 %. Note that similar behavior was observed in the XPS spectra on Na^+ terminated mica, where the Na^+ coverage was measured to be spatially inhomogeneous with a surface coverage of about 50 % (see Figure 3.2). Figure 3.12 b) shows that Cs-mica is not significantly different from K-mica. The effect of H-mica, shown in Figure 3.12 c) is interesting, as H-mica shows a substantially reduced SFG intensity compared to the initial K-mica. However, the effect of HCl is not fully reversible by flowing KCl solution. By averaging the in Figure 3.12 observed intensities, it is possible to obtain generalized results about the cationic effect on the mica-water interface.

Figure 3.13 shows the on average observed SFG intensity as a function of mica surface cation. The average SFG intensity of K-mica serves as a reference and is thus per definition 1. As a consistency check, cleaved and K-mica are displayed independently, and within the experimental uncertainty, the same average SFG intensity is observed.

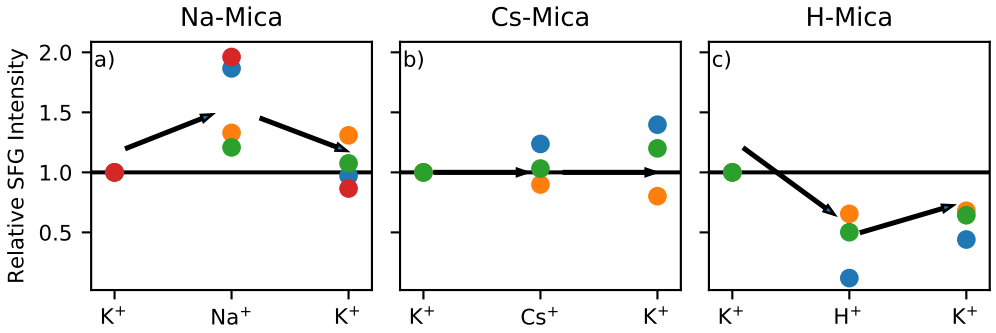

Figure 3.12: Trends of repeated SFG intensity measurements as relative variation of Na^+, Cs^+ and H^+ terminated mica surface. a) intergrated SFG intensity of Na-Mica compared to K-Mica. b) integrated SFG intensity of Cs-Mica compared to K-Mica and c) shows the integrated intensity compared to K-Mica. Note that the intensity does not recover after cleaning in the case of H-Mica.

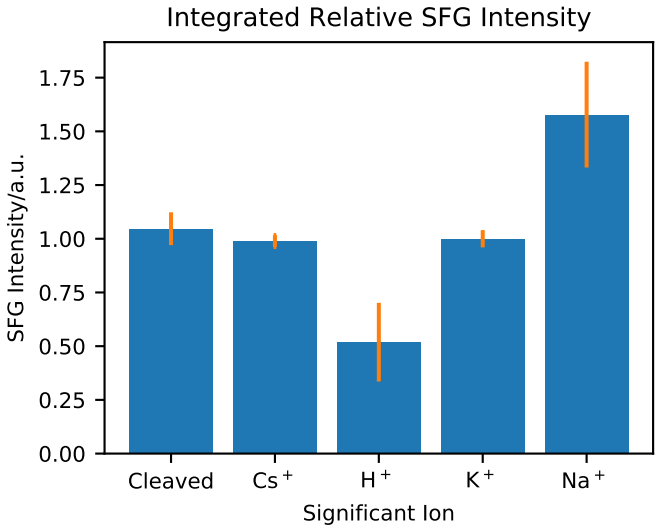

Figure 3.13: Average integrated SFG intensity of mica-water interfaces in the OH-stretch region from 3000 cm^{-1} to 3550 cm^{-1}, normalized to the intensity from the K-mica-water interface.

Clearly, Cs-mica is not significantly different from K-mica, but Na-mica shows a significant SFG intensity increase of about 50 %, while H^+ shows a significant intensity decrease of about 50 %.
As explained in Equation 1.24, the SFG intensity depends on the density and the orientation of the contributing oscillators. The observed variation in intensity is most likely not caused by density variations of the interfacial water, as this is expected to correlate with the ion size. Cs-mica and K-mica show no significant difference, even though they have different ion radii.[100] It is thus likely that the observed SFG intensity variations are caused by changes in the orientation of interfacial water. Possibly the specific cation species on the mica surface causes a change of the average interfacial water orientation. This change alters the average z-projection of the water dipole moment and, in turn, changes the SFG intensity. The observed SFG intensity variations thus reflect changes in the average orientation of interfacial water dipole moments.[31]
By comparing Figure 3.4 and Figure 3.13 one can see that the ice nucleation temperature and the SFG results are correlated. A lower ice nucleation temperature coincides with a larger SFG intensity and vice versa. Meaning water, with an on average more aligned dipole moment in z-direction (Na^+), exhibits a lower ice nucleation temperature, because the alignment hinders it from forming ice crystals. Contrary less oriented water (H^+) can move more freely and form ice crystals more easily and therefore increases the HIN efficiency. This conclusion is consistent with previous reports that the density and orientation of the interfacial water govern the HIN efficiency, which can be affected by the surface lattice and/or surface charges etc.[84,93,94,101]
Further insights into the molecular structure of the mica-water interface were obtained by using ab initio molecular dynamics simulations. It was found that the HIN efficiency could depend on the positional arrangement of the interfacial water layer. Depending on the mica surface cation, the interfacial water layer could mimic the hexagonal structure of the Ih basal plane of ice and thus favor ice nucleation. Here the size of the protruding surface cation and the absorption energy seems to be the tuning parameters. Additionally, the interfacial water orientation was found to depend on the surface cation atop mica as well. In the MD simulations, it was observed that for H-Mica about 25 % of the interfacial water molecules were pointing towards as well as away from the mica interface. For K-Mica and Cs-Mica 75 % and 67 % of the interfacial water molecules were pointing towards the mica interface, while 7 % and 6 % were pointing away from the interface. The 25 % pointing ratio of the H-Mica matches roughly the expected ratio for an ice crystal and could thus favor ice nucleation. The 75 % and 67 % for K-Mica and Cs-Mica deviate significantly from the pointing ratio of the ice crystal and thus hinder ice nucleation. It was therefore hypothesized that the interfacial water pointing orientation could be a relevant factor for ice nucleation as well. The molecular insights presented here hopefully help to gain a better understanding of HIN on other mineral surfaces as well.

4 Influence of Electrolytes on Dynamics of Interfacial Water

The following chapter is reproduced with minor changes from J. Phys. Chem. B 2019, 123, 40, 8610-8616.[58] https://pubs.acs.org/doi/10.1021/acs.jpcb.9b08131. Further permissions related to the material excerpted must be addressed to the ACS

4.1 Abstract

Heterogeneous ozone chemistry occurring on aerosols is driven by interfacial chemistry and thus affected by the surface state of aerosol particles. Therefore, the effect of electrolytes on the structure of interfacial water has been under intensive investigation. However, consequences for energy dissipation rates and mechanisms at the interface are largely unknown. Using time-resolved sum frequency generation spectroscopy, we reveal that the relaxation pathway is the same for neat water-air as for aqueous solutions of Na_2SO_4 and Na_2CO_3. We further show that similar lifetimes are extracted from all investigated systems and that these lifetimes show an excitation frequency dependent relaxation time from 0.2 ps up to 1 ps. Hence, despite static SFG on the same systems revealing that the interfacial aqueous structure changes upon adding electrolytes, the vibrational dynamics are indistinguishable for both pure water and different electrolyte solutions.

4.2 Introduction

Physical and chemical processes occurring at aqueous interfaces have been shown to play a prominent role in a variety of fields ranging from the chemistry of atmospheric aerosols and heterogeneous catalysis to biophysics and biochemistry. For instance, the heterogeneous ozone chemistry occurring on aerosols is largely driven by interfacial chemistry.[10] In the case of atmospheric aerosols, the situation is especially complicated because of the large number of different components aerosols can contain.[102] Among these components is a variety of ions, e.g., sodium, sulfate, and carbonate, originating from natural, as well as artificial sources.[103,104] Sulfate, for example, can be found in large quantities in urban areas, since it is released during industrial production processes.[105] On the other hand, roughly 30 % of the CO_2 released by human activity in the past few decades has been uptaken by the ocean and a large part of it now resides in the form of CO_3^{2-} within the ocean itself.[106]

Given its relevance to environmental chemistry, the structure of interfacial water in contact with ions has been under intensive investigation throughout the past decades.[107–113] While knowledge of the structure of interfacial water is essential for understanding heterogeneous ozone chemistry, understanding the dynamics of these interfaces is also important, as in the course of chemical conversion on the surface of the aerosol transport of excess energy to and from the reaction sites is crucial. Yet, a molecular model of these transport mechanisms is currently missing. How is the energy transported to and from reaction sites? What is the effect of different ions on the transport mechanisms?

Here we study, using sum-frequency-generation (SFG) and its phase-resolved (PS) extension PS-SFG, the effect of ions on the structure and the vibrational dynamics of interfacial water. SFG is a second-order nonlinear process that is interface-specific owing to its selection rules.[31] We use an infrared (IR) beam in resonance with the O-H stretch vibration of the water molecules. The O-H stretch vibrational frequency is a marker of the strength of the local hydrogen bond network and the intensity provides information about the degree of alignment.[17]

SFG and PS-SFG have already been used to study the effect of ions on the hydrogen bond network of interfacial water. It was found that ions can perturb the strength of the hydrogen bonds at the interface even though the ions are located several hydration layers away from the interface. The results indicate that ions increase the strength of the hydrogen bond network. Furthermore, the relative order of ions at the interface was investigated and an ion distribution model was developed. With the help of PS-SFG the orientation of the dipole moment at the aqueous-air interface was studied and it was shown that certain ions can even reverse the order of the dipole moment at the interfacial region of water.[107–109]

To study the vibrational energy flow, we present the first study on the vibrational dynamics of the water stretch vibration under the influence of ions. We use Pump-Probe (PP) SFG to probe the vibrational dynamics at the interface, the interface-specific counter-part to Pump-Probe IR spectroscopy. PP-SFG adds an additional pump laser that is tuneable in frequency and time to the SFG setup. With its sub-picosecond time resolution it is well suited to measure the lifetimes of the water stretch vibration. PP-SFG can be used to measure how fast the involved oscillators lose their excitation energy, how vibrational energy is exchanged between molecules and how fast they change there hydrogen bond partners. Previous PP, IR, and SFG studies on water have shown a strong pump frequency dependence of the relaxation time. Weakly bonded hydrogen molecules relax slower then stronger bonded hydrogen molecules.[114] Studies of water in contact with lipids at negative charged surfactants have revealed interesting coupling dynamics between different water species.[115]

As water in nature is rarely free of ions, it is important to understand the effects of ions on the water-vapor interface. It remains unclear whether the ion induced changes to the hydrogen bond network also influence the vibrational lifetimes of the involved molecular vibrations.

4.3 Methods

Laser pulses are produced by an oscillator (Mai Tai, Spectra Physics) with a central wavelength of 800 nm and roughly 50 nm bandwidth. The Spitfire Ace is pumped by two Empowers (22 mJ pulse energy at 527 nm) and has a power output of about 10 W and a pulse length of 40 fs with a repetition rate of 1 KHz. The sum frequency signal is generated using a focused broadband IR beam generated by a Topas-c with DFG stage (p-polarized, 15 μJ, 350 cm^{-1}, centered at 2500 cm^{-1}, angle 40° to surface normal) and a fraction of the 800 nm output, send into an etalon to generate a narrow-band visible laser pulse (s-polarized, 20 μJ, 810 nm, angle 70°). The SFG signal with a central frequency of 674 nm is sent into a spectrometer and detected using an Andor Newton electron-multiplied charged coupled device (EMCCD) camera. The integration time of a single spectrum is between 100 s and 200 s depending on the specific signal intensity and laser power. To correct for the frequency content of the IR beam, all SFG spectra are normalized to the non- resonant SFG response of z-cut quartz.
The salts are SigmaAldrich ACS Grade with a purity of more than 99.9 % and prior to dissolving them in D_2O, the salts are baked for 10 h at 650 °C. No CH contamination could be observed in the SFG experiments. Both the Na_2SO_4 and Na_2CO_3 solutions prepared at room temperature had molality of 1.8 mol/kg; the exact concentrations can be found in Table 4.1.

Table 4.1: Used salt concentrations.

Ion	Amount/g	D_2O/ml	Molality/mol/kg
Na_2CO_3	64 ± 1	300 ± 1	1.8 ± 0.1
Na_2SO_4	62 ± 1	220 ± 1	1.8 ± 0.1

To avoid heating effects from the laser, the sample is rotated such that subsequent laser pulses hit different spots. A chiller is used to keep the temperature of the sample constant during the measurement. To minimize evaporation, the temperature is maintained between 10 °C to 15 °C, and an automated syringe is used to keep the water level at a constant height throughout the measurement.
To generate the narrowband pump (p-polarized, ≈ 90 cm^{-1} full width at half maximum, fwhm, 55° angle) at ≈ 2000 nm the idler output of a second Topas-c is sent into a BBO crystal to generate ≈1000 nm IR pulses. These pulses are overlapped with 800 nm pulses within a $LiNbO_3$ crystal to generate the narrowband pump pulses. By tuning the frequency of the doubled idler and adjusting the phase-matching condition at the $LiNbO_3$ crystal, the infrared pump laser can be tuned between 2350 cm^{-1} and 2750 cm^{-1}. The power varies from 5 μJ to 10 μJ depending on the central pump frequency. The cross-correlation of pump and probe is emitted at about 570 nm after up-conversion with the visible laser pulse. Prior to each pump-probe experiment, the pump-probe delay dependency is measured and used as a reference for the instrument response function. The instrument response function typically has a temporal width of about 200 fs (subsection 2.2.1). To record pump-probe spectra, a chopper blocks

every second laser pulse of the pump and a vibrating mirror separates the pumped and unpumped response sending them onto distinct sections of the CCD camera.

4.4 Structure on the Water-Air interface

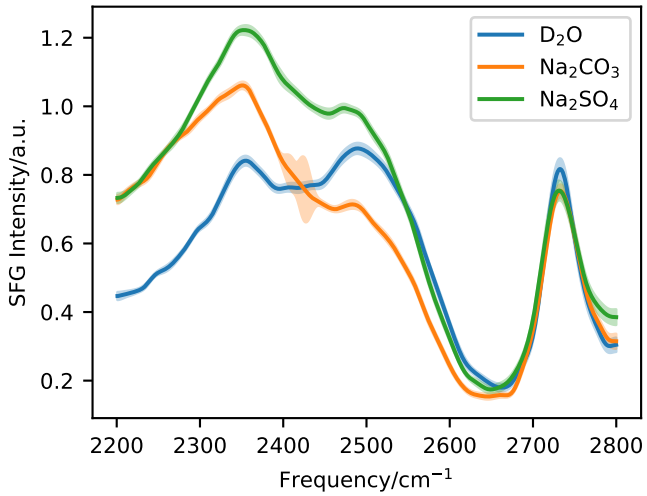

Figure 4.1: SFG of OD-Stretch vibrations for D_2O, 1.8 M Na_2SO_4 and 1.8 M Na_2CO_3. Shading around the lines indicates uncertainty of the data based on 10 averaged spectra. The region of enlarged uncertainty at 2400 cm^{-1} originates from an unusual cluster of cosmic muon induced spikes.[116]

To investigate the impact of ions on the structure and the vibrational dynamics of the water-air interface, we first turn towards the structure. Structural information can be extracted from the interfacial vibrational spectrum, as stronger hydrogen bonds result in lower vibrational frequencies, and weaker hydrogen bonds in higher vibrational frequencies.[17] The spectrum of just the interface is obtained by SFG spectroscopy in which the incoming infrared beam is in resonance with the molecular vibration of interest.[31]

A SFG spectrum of the OD-stretch vibration of D_2O is shown in Figure 4.1. We use D_2O instead of H_2O as the vibrational dynamics is slower.[57] This also means that conclusions drawn from D_2O could be different for H_2O. Around 2750 cm^{-1} the free O-D peak is visible. This relative sharp peak originates from O-D groups pointing into the vapor phase and thus having no hydrogen bond partner.[33] Due to the absence of hydrogen bond acceptors, these bonds vibrate at a relatively high frequency. The relatively broad feature from 2200 cm^{-1} to 2550 cm^{-1} originates from hydrogen-bonded O-D vibrations and consists of two peaks centered around 2380 cm^{-1} and 2510 cm^{-1}. The origin of these two features has previously been investigated using different isotopic dilutions of H_2O, D_2O, Methanol and Ethanol mixtures. This has allowed separating

intramolecular and intermolecular contributions and led to the conclusion, that the intramolecular coupling generates the double-peak feature, while the intermolecular coupling induces a redshift of the O-H stretch vibration.[33,117–120]
A solution of 1.8 M Na_2CO_3 in D_2O shows a static SFG spectrum that is substantially different from that of the clean water surface. The strongly hydrogen-bonded region from 2200 cm^{-1} to 2420 cm^{-1} is enhanced, whereas the weakly hydrogen bond region from 2420 cm^{-1} to 2600 cm^{-1} is reduced in intensity. This hints towards an overall strengthening of the hydrogen-bonded network in the presence of Na_2CO_3, while the free OD appears unchanged.
In the case of Na_2SO_4, the spectral changes are different. 1.8 M Na_2SO_4 in D_2O causes a signal enhancement from 2200 cm^{-1} on up till 2550 cm^{-1}, while from this point on, until the end of the free OD peak at 2800 cm^{-1}, the signal is identical to that of pure water. The low frequency enhancement can again be interpreted as strengthening of the hydrogen bond network.[121,122]

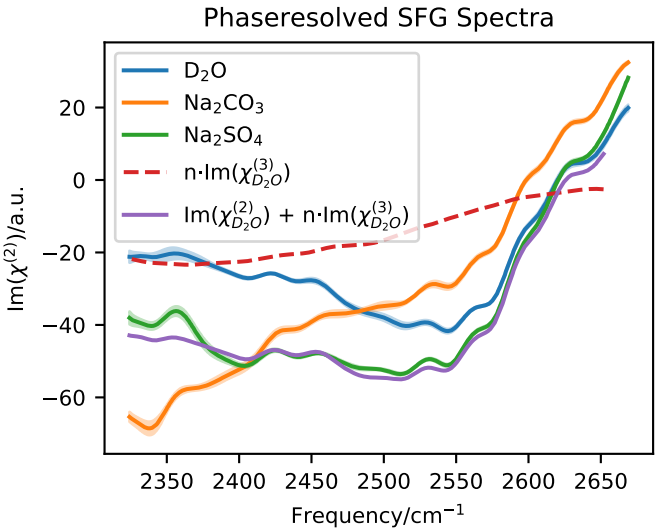

Figure 4.2: Phaseresolved SFG spectra of D_2O, Na_2SO_4- and Na_2CO_3-D_2O of the OD-stretch vibration. The difference between the spectrum of D_2O and Na_2CO_3 could be explained by a $\chi^{(3)}$ contribution from D_2O. The purple line is the sum of the D_2O spectrum and a $\chi^{(3)}$ specturm from Wen et. al.[45] showing a remarkable similarity to the observed Na_2SO_4 spectrum.

To investigate the orientation of the water molecules at the interface, we performed phase-resolved (PS) SFG measurements. Figure 4.2 (b) shows $\mathrm{Im}(\chi^{(2)})$ of the same salt-D_2O solutions. The hydrogen-bonded region of D_2O around 2300 cm^{-1} to 2600 cm^{-1} has a negative $\mathrm{Im}(\chi^{(2)})$ indicative of a net downwards orientation of the O-D transition dipole moment of interfacial water towards the bulk.[41,42,123] Around 2620 cm^{-1}, the $\mathrm{Im}(\chi^{(2)})$ changes sign, showing that the free OD at around 2750 cm^{-1} has an opposite and thus net orientation with the O-D transition dipole moment

out of the interface. Adding 1.8 M Na_2CO_3 reduces the $\mathrm{Im}(\chi^{(2)})$ around the weakly bonded 2550 cm^{-1} region and increases the $\mathrm{Im}(\chi^{(2)})$ below 2490 cm^{-1}. This supports the hypothesis of Na_2CO_3, strengthening the interfacial hydrogen bonding network in comparison with the neat D_2O-air interface. A solution of 1.8 M Na_2SO_4 in D_2O enhances the $\mathrm{Im}(\chi^{(2)})$ as well in both the strongly and weakly hydrogen-bonded region. The enhancement is similar as in the case of the static SFG spectrum from Figure 4.1 (a) and can again be interpreted as a strengthening of the hydrogen-bonded network. Nonetheless, this increase could also resemble $\chi^{(3)}$ contributions. From previous studies of charged interfaces, it is known that $\chi^{(3)}$ effects can play a role in the observed SFG and PS-SFG spectra.[45,46,124,125] In particular, it was shown that the existence of a static electric field can induce an anisotropy throughout the bulk water and thus alter the SFG signal. It is commonly assumed that the electric field induced by the charge is screened by counterions effectively over the Debye length. The Debye length of saltwater with 2 M ion concentrations is below 2 Å and thus smaller than a single water layer, implying that the $\chi^{(3)}$ contributions should be insignificant.[124,126,127] On the other hand, there is a remarkable agreement between the Na_2SO_4 PS-SFG spectrum and a constructed PS-SFG spectrum where the PS-SFG spectrum of neat D_2O and $\chi^{(3)}$ as reported by Shen et al.[45] is used. This is shown as purple line in Figure 4.2. The $\mathrm{Im}(\chi^{(3)}_{D_2O})$ was taken from $\chi^{(3)}$ data of H_2O and transformed into D_2O region using the harmonic approximation. To match the difference, a scaling factor of $n = -7$ was used. The exact number of the scaling factor is meaningless, but the negative sign of the $\chi^{(3)}$ contribution implies that the positive ion Na^+ is closer to the surface than the negative ion ${SO_4}^{2-}$.[45] As Na^+ prefers bulk hydration,[128] we conclude that both ions Na^+ and ${SO_4}^{2-}$ are sub surface. This is in line with simulation studies[129] In the case of Na_2CO_3 the $\chi^{(3)}$ contribution to the signal could be excluded based on the spectral shape of the signal. We can only speculate about the reason for the difference of Na_2SO_4 and Na_2CO_3 in $\chi^{(3)}$ signal. It could be that Na_2SO_4 forms a double-layer-like structure, while ${CO_3}^{2-}$ and Na^+ distribute more within the same water slab, creating an in-plane electric field that is not probed by SFG here.

Static and phase-resolved SFG spectra of 1 M Na_2SO_4 and 1 M Na_2CO_3 in H_2O have previously been reported by Allen and coworkers.[108,109] Even though the overall spectral shapes between theirs and ours are comparable, there are some notable differences. At present it remains unclear whether these differences are the result of different concentrations, D_2O vs H_2O effects, impurities, or phase errors.[130]

From these and prior measurements,[107–109] we conclude, that ions in bulk have a direct effect on the interfacial hydrogen bonded network. However, from the SFG and the PS SFG spectra nothing can be inferred about the vibrational dynamics at the interface. Do ions increase or decrease the lifetimes of the OD stretch vibration? Is the energy flow dynamics affected? To shed some light on these questions, we now turn towards the dynamics of the stretch vibration of the interfacial hydrogen bond network.

4.5 Vibrational Dynamics

To probe the vibrational dynamics at the interface we use Pump-Probe (PP)-SFG. By tuning both, the pump-probe time delay and the central pump frequency, we obtain information about the relaxation time, as a function of the excitation frequency.[131,132]

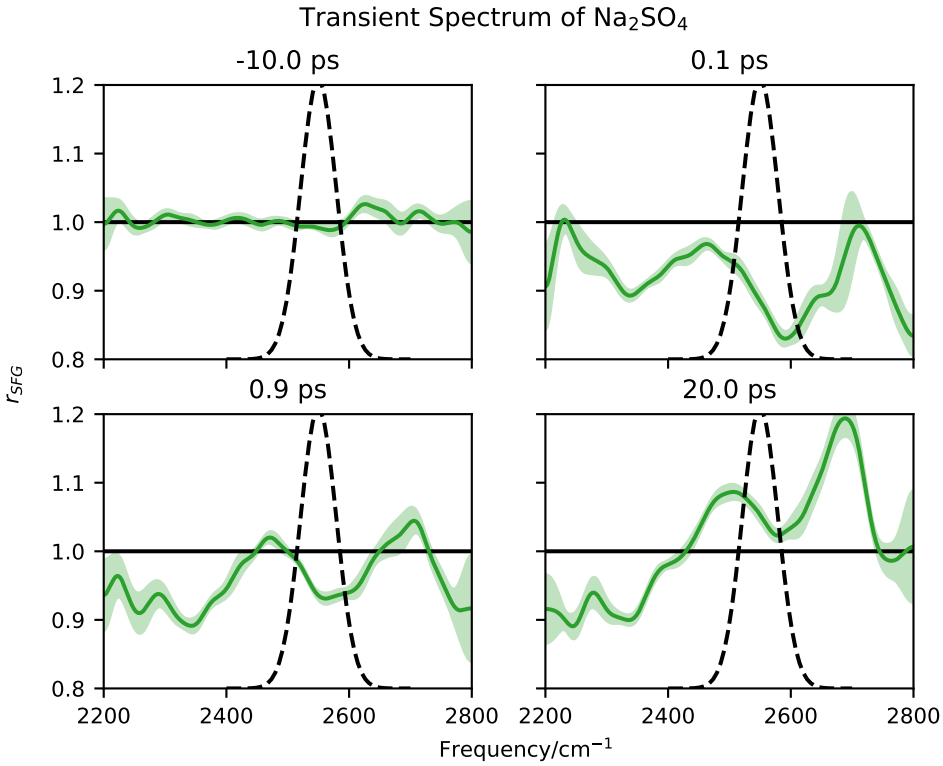

Figure 4.3: Ratio of pump/unpumped SFG spectra (green) at four different pump-probe time delays (−10 ps, 0.1 ps, 0.9 ps, 20 ps) of 2 M Na_2SO_4-D_2O solution. The dashed black line denotes the spectral shape of the pump pulse and the red line is an guide to the eye.

Figure 4.3 shows the ratio of pump/unpumped SFG spectra (bleach) at pump-probe time delays of −10 ps, 0.1 ps, 0.9 ps and 20 ps exemplary for 2M Na_2SO_4 pumped at 2550 cm^{-1} as a green line. The black dashed line denotes the spectral shape of the pump pulse. At negative pump-probe time delays, the probe pulse arrives at the sample before the pump pulse. Thus the ratio for negative times is a flat line around 1. At 0.1 ps the pump pulse depletes the ground state, and we see a reduction in the ratio around the mean pump frequency. At later times, i.e. after the excitation due to the pump pulse, the system relaxes, and therefore the ratio recovers back to 1. However one notes, that the spectrum after 20 ps has a distinct shape and shows frequency-dependent features. To understand this frequency dependency, we turn towards Figure 4.4.

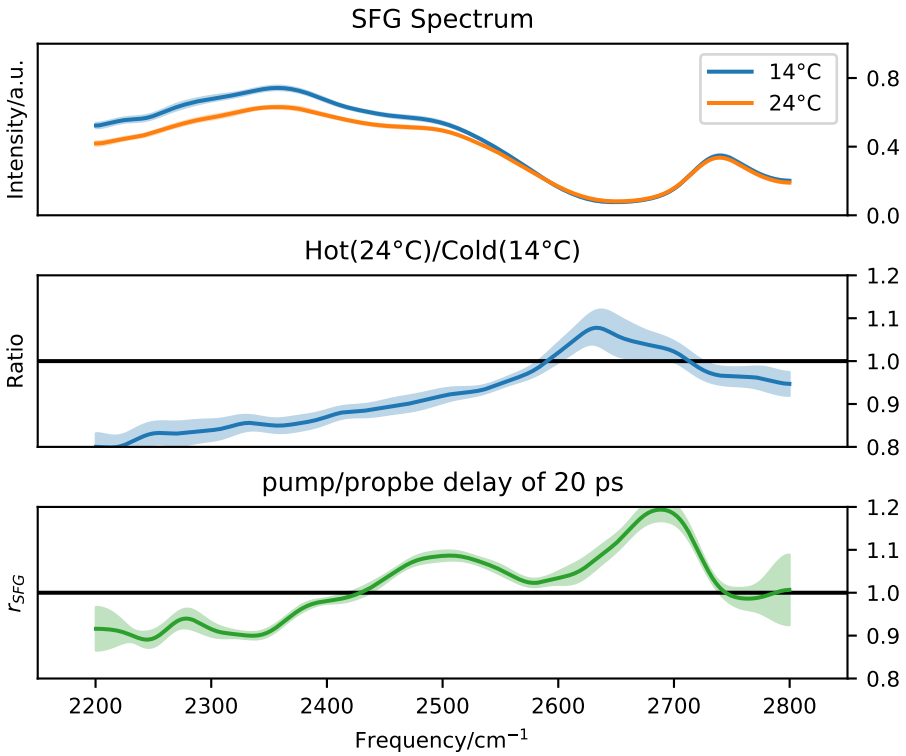

Figure 4.4: SFG Spectra of Na_2SO_4. Top panel shows the SFG spectra of cold (14 °C) and hot (24 °C) Na_2SO_4. The middle panel shows the ratio of hot/cold. Bottom panel shows pumped/unpumped for a pump-probe time delay of 20 ps.

The top panel of Figure 4.4 shows static SFG spectra for Na_2SO_4 at 24 °C (Hot) and 14 °C (Cold). Heat leads to an overall loss of orientation throughout the hydrogen bond network, in particular, the strongly hydrogen bonded region with its intermolecular coupling around 2380 cm^{-1} is affected by this. For a better visibility, the middle panel shows the ratio of the hot and the cold spectrum, while the bottom panel shows the ratio of the pump and unpumped SFG signals for relatively large 20 ps pump-probe time delays. If the signal at 20 ps is solely given by a temperature difference, the spectra in panel b) and panel c) should be the same. While the overall slope of the ratios is indeed the same, the bottom panel exhibits a more complex structure. Apparently, the state reached after 20 ps is not yet fully thermalized.

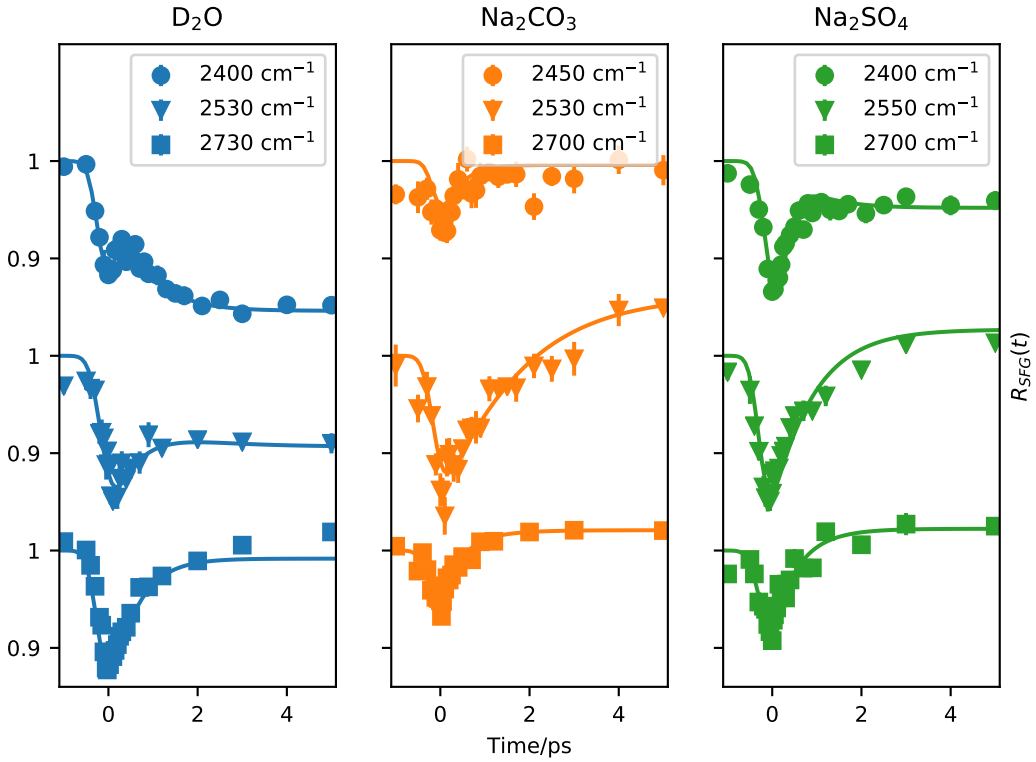

Figure 4.5: Traces of D_2O, Na_2CO_3, and Na_2SO_4 at three different pump frequencies. Lifetimes are extracted by fitting a four-level model. For pump frequencies greater than 2700 cm^{-1} a single exponential fit is used.

The traces show in Figure 4.5 are constructed by averaging the bleach over ±30 cm^{-1} around the central excitation frequency. For each trace between 5-25 transient SFG spectra at 31 different pump-probe time delays were measured and averaged. In Figure 4.5 traces for D_2O, Na_2SO_4, and Na_2CO_3 at three different mean pump frequencies each are shown. At negative times, the pump pulse arrives after the probe pulse, and thus, R_{SFG} is 1. At around $t = 0$ ps, the pump and the probe pulses start to overlap in time, and the ground state of the sample is bleached, resulting in a decrease

of R_{SFG} and a consecutive recovery of the signal.
One notes that the magnitude of R_{SFG} depends on the power of the pump pulse and the IR absorption cross-section at the pumped frequency. Because the pump power is highest at around $2500\,\mathrm{cm}^{-1}$ as is the IR absorption, the largest bleach can be seen around this pump frequency. Remarkably, D_2O pumped close to the free OD at $2730\,\mathrm{cm}^{-1}$ is an exception to that rule, as we observe a relative high R_{SFG} of 10 %. Taking the overall picture into account, one can see that the amplitude is largest for Na_2SO_4 and smallest for Na_2CO_3 with D_2O in between. Primarily, the amplitude of the trace is related to the IR absorption of the pump laser.

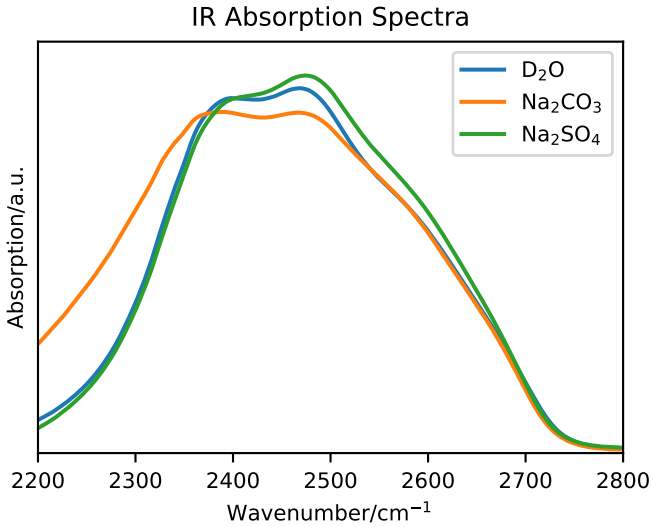

Figure 4.6: IR absorption of Na_2SO_4, Na_2CO_3, and D_2O within the probed frequency range. The OD-Stretch vibration gives rise to a borad resonance from $2200\,\mathrm{cm}^{-1}$ to $2700\,\mathrm{cm}^{-1}$.

Figure 4.6 shows IR absorption spectra of Na_2SO_4, Na_2CO_3, and D_2O with the same salt concentrations as for the SFG spectra. The ATR spectra show the highest absorbance for Na_2SO_4 and the smallest for Na_2CO_3 with D_2O in between. This matches roughly what is expected from the amplitudes of Figure 4.5. Surprising is the long tail of Na_2CO_3 between $2200\,\mathrm{cm}^{-1}$ and $2300\,\mathrm{cm}^{-1}$, that does not have a counterpart in the SFG spectrum or traces of the same ionic solutions.
For long delay times ($t \geq 4\,\mathrm{ps}$) R_{SFG} of Figure 4.5 converges to a value different from one, but constant on the picosecond timescale of the experiment. This late time signal represents the elevated temperature of the system and the subsequent weakening of the H-bonds after vibrational relaxation as discussed above in Figure 4.4. Depending on the influence of the heat, the value of this constant can be either smaller or larger than one. D_2O pumped at $2400\,\mathrm{cm}^{-1}$ is an example for a long time signal smaller than one, while most others show a signal exceeding one.
To extract relaxation times the traces are modeled (See Figure 4.5). The reproducible

bump in the trace of D_2O at delay times of a few hundred femtoseconds, pumped at 2400 cm^{-1}, shows that a model with at least two lifetimes is needed to describe the process. As such we use a four-level model described in subsection 2.1.3 for pump frequencies exciting within the range of the bonded OD stretch vibration (pump frequency < 2700 cm^{-1}). For the free OD region (>2700 cm^{-1}) a single exponential model is used.[133–135] Figure 4.7 shows the lifetimes of the first excited state τ_1 for all excitation frequencies on all samples.

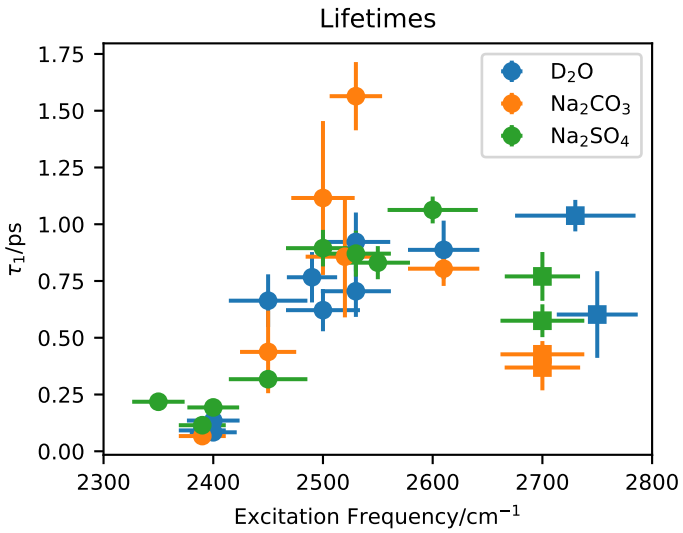

Figure 4.7: Lifetimes of the OD stretch vibration for the given excitation frequency. Round dots indicate lifetimes extracted from a four-level model. Squares indicate lifetimes extracted from a single exponential fit. The x error bars correspond to 1 σ excitation width, y error bars are fit errors. In total, ≈ 24000 SFG spectra were analyzed.

Figure 4.7 shows, that we observe the shortest lifetimes of ≈ 0.2 ps for all samples around a pump frequencies of 2400 cm^{-1}. From Figure 2.12 it can be seen that the instrument response function is limiting in the low frequency region. Up on increasing the excitation frequency to 2600 cm^{-1} an increase in lifetime up to almost 1 ps is found. In the case of D_2O this nicely matches previously obtained results.[114] It was hypothesized, that the reason for this heterogeneity is the coupling of the OD-stretch mode with an overtone of the OD bending mode.[136–139] Around 2400 cm^{-1}, the 1st overtone of the bending mode overlaps with the OD-Stretch vibration. Therefore the overtone provides an efficient relaxation path to the excited molecules. Upon exciting the surface at a frequency of 2500 cm^{-1} or higher, the coupling to the overtone of the bending mode becomes less efficient, leading to slower vibrational relaxation. An alternative explanation is provided from theoretical work, interpreting this frequency dependency as a hydration layer effect and correlating it with the number of H-bonds per water molecules.[140]

Pumping close to the free OD peak (2700 cm^{-1} to 2750 cm^{-1}) shows lifetimes around 0.5 ps for the stretch vibration. With Na_2SO_4 and D_2O having roughly 700 fs lifetime and Na_2CO_3 400 fs. The free OD was previously studied and showed lifetimes around 800 fs.[135]
As apparent from Figure 4.7, the difference in lifetimes between the three samples D_2O, Na_2CO_3, and Na_2SO_4 are minimal. For specific pump frequencies, the lifetime of the samples can be different by more than 2σ, but the error bars capture only the stability of the individual experiment, and do not account for correlations between the fitting parameters and sample-to-sample variations. Taking the complete picture into account there is no clear difference between the three samples. This is somewhat surprising, because, as it can be seen in Figure 4.1 and Figure 4.2, the static SFG spectra of Na_2SO_4 and Na_2CO_3 show significant differences from D_2O, hinting towards structural changes induced by the CO_3^{2-} and $SO_4{}^{2-}$ ions. Nevertheless, this structural change apparently does not significantly influence the vibrational dynamics of the involved vibrational state within the uncertainty of the experiment. It could, however, be that larger and more granular sampling rate of the pump frequency, or an improved signal to noise ratio, reveals differences between D_2O-H_2O and D_2O-ion bindings. However given the fact that differences in the static spectra appear through bands of about 100 cm^{-1}, a 60 cm^{-1} wide pump pulse should be sufficient to resolve these differences. Furthermore, lifetimes with differences of less then 0.2 ps are challenging to detect with the currently available measurement techniques.

4.6 Conclusion

Returning to the questions presented in the introduction of this section, we conclude that the interfacial water structure of aerosol particles is ion-dependent. As such, the surface structure can be responsible for unique properties of aerosol particles. Still, because the interfacial vibrational dynamics seem to be unaffected by the ion content, models of excess energy transport do not need to take the specific ion content into account. Instead, models taking solely the properties of the static H-bond network of water into account, are likely sufficient to describe the details of excess energy transport accurately, even for aerosol particles with high ion concentrations. We further note that the four-level model, first developed for bulk water, can be used for interfacial water as well, even if the H-bond network is perturbed by high ionic concentrations. In addition, we show that the lifetime of the stretch vibration depends on the excitation frequency and ranges from about 0.2 ps to over 1 ps.

5 Influence of Water Orientation on Water Dynamics

The following chapter is reproduced with minor changes from Phys. Chem. Chem. Phys., The Royal Society of Chemistry, 2020.[141]

5.1 Abstract

Zwitterionic phospholipids are one of the main constituents of biological membranes. The electric field associated with the two opposite headgroup charges aligns water molecules in the headgroup region. Here, we study the role of water alignment on the sub-picosecond vibrational dynamics of lipid-bound water. To this end, we compare the dynamics of oppositely oriented water associated with, respectively, a phosphocholine (PC) headgroup and an inverse-phosphocholine with non-ethylated phosphate groups (CP). We find that the dynamics are independent of the water orientation, implying that the vibrational dynamics report on the local properties of the water molecules.

5.2 Introduction

The main constituents of biological membranes are zwitterionic phosphatidylcholine (PC) lipids, using amphiphilic interactions with the adjacent water molecules to form the naturally occurring bilayer structure.[142] Interestingly, the naturally occurring zwitterionic phosphatidylcholine lipid only exists in the PC conformation. The CP, or CPe, conformation, containing a reversed headgroup structure, has to be synthesized and does not occur naturally.[143] This raises the question whether there are fundamental differences between the PC and CP(e) conformation making the latter biologically irrelevant. Perttu et al.[143] discovered that DPPC and DPCPe liposomes release encapsulated anionic carboxyfluorescein as well as glucose at different rates, suggesting that the configuration of the headgroup charge plays a significant role in determining membrane permeability. Further, it was found that CPe liposomes do not appreciably interact with Ca^{2+} ions. It was hypothesized that the permeability for Na^{+} and Cl^{-} might be altered as well. Another important but often overlooked feature of a lipid is its interaction with water itself. Dreier et al.[144] have shown that the charge distribution throughout the zwitterionic headgroup determines the orientation of the water bound to the headgroup.[145,146] Given the opposite orientation of water bound to PC- and CPe- based lipids, one might expect that the molecular structure of lipid-bound water is different for the two lipids.

For oppositely oriented water in contact with, respectively, the negatively charged lipid DPPG and positively charged DPTAP, it has indeed previously been shown that both the structure and vibrational dynamics of water in contact with these headgroups is different. For negative (positive) lipids, the water dipole points towards (away from) the lipid layer, exhibiting an ultrafast relaxation path available only for the positively charged lipid.[60,147,148] In the case of the negatively charged surfactant sodium dodecyl sulfate (SDS) Water interface two types of water were reported.[115] Given the ubiquitous presence of the lipid/water interface, these kinds of differences in vibrational dynamics – that reflect differences in structure[149] – could be important for the functionality of lipid bilayers.
To investigate the role of interfacial water alignment on the water properties, we study the lipid water interaction using sum-frequency-generation (SFG) spectroscopy, an even-order nonlinear process that is almost exclusively interface-specific owing to its selection rules.[31,146,150,151] We use an infrared beam in resonance with the OD-stretch vibration to probe the interfacial (heavy) water (D_2O) in contact with the lipids. The OD-stretch vibrational frequency is a marker of the strength of the local hydrogen bond network and the intensity of the SFG signal provides information about the average orientation of the transition dipole moment.[17] To study the vibrational dynamics of the water lipid interface we use Pump-Probe SFG (PP-SFG) spectroscopy, the interface-specific counterpart to infrared (IR) Pump-Probe spectroscopy.[152] With PP-SFG it is possible to study vibrational dynamics at a sub ps time scale and thus the spectral diffusion.[51,153] Here, we use this method to investigate vibrational dynamics and spectral diffusion of water interacting with PC and CP monolayers. Our results demonstrate, that despite the opposite orientation, the vibrational dynamics of CP and PC-bound water molecules are indistinguishable.

5.3 Experimental Section

A pulsed laser beam is produced by an oscillator (Mai Tai, Spectra Physics) with a central wavelength of 800 nm and roughly 50 nm bandwidth. Two Empowers (22 mJ pulse energy at central wavelength of 527 nm) pump a Spitfire Ace optical amplifier, providing a power output of about 10 W at a pulse length of 40 fs with a repetition rate of 1 kHz. The sum frequency signal is generated by overlapping a narrow-band 800 nm visible laser pulse (s-polarized, pulse energy of 20 μJ, central wavelength of 810 nm, incidence angle to surface normal of 70°) with a focused broadband IR beam generated by a Topas-c with DFG stage (p-polarized, pulse power of 7 μJ, FWHM of 350 cm^{-1}, central frequency of 2500 cm^{-1}, incidence angle of 40° to surface normal) The SFG signal has a central frequency of 674 nm and is sent into a spectrometer and detected using an Andor Newton electron-multiplied charged coupled device (EMCCD) camera. The accumulation time of a single spectrum is 100 s. To correct for the intrinsic spectrum of the IR beam, all SFG spectra are normalized to the non-resonant SFG spectrum of z-cut quartz.
The narrowband pump beam (p-polarized, $\approx$ 90 cm^{-1} FWHM, 55° incidence angle to

surface normal) is generated by doubling the frequency of the 1000 nm idler output of a second Topas-c within a BBO crystal, generating IR pulses at ≈ 2000 nm. These pulses are overlapped with 800 nm pulses within a $LiNbO_3$ crystal generating the narrowband pump pulses. The infrared pump beam can be tuned between 2350 cm^{-1} and 2750 cm^{-1}, by tuning the frequency of the doubled idler and adjusting the phase-matching condition at the $LiNbO_3$ crystal. The resulting IR power varies from 5 μJ to 10 μJ depending on the central pump frequency.
To record pump-probe spectra, a chopper blocks every second laser pulse in the pump laser path, and a vibrating mirror separates the pumped and unpumped signal spatially on the CCD camera. With a motorized delay stage the time delay between the pump- and the probe pulse is changed using various step sizes between 50 fs and 6 ps. The total time range is −10 ps to 20 ps where the pump arrives after (before) the probe for negative (positive) times. In total 27 different pump-probe time delay spectra were recorded.
To minimize heating effects from the laser, the sample is rotated at 13.6 rpms with the laser spots on a 55 mm diameter cycle.[63] A chiller is used to keep a constant temperature of 20 °C throughout the experiment and the water level is kept constant using a reservoir.

5.3.1 Monolayer Preparation

The lipids are obtained from Avanti Polar Lipids and dissolved in a 9:1 mixture of chloroform (>99%, stabilized with amylene, Fischer Scientific) and methanol (99.99%, Fischer Scientific) at a concentration of 0.43 mmol/l. To avoid oxidation of the unsaturated lipid molecules, DOPC and DOCPe are dissolved under a nitrogen atmosphere. D_2O (99.9 %) is obtained from Euriso-Top and used as received.

Table 5.1: Average configuration of monolayer preparation

Lipid	Concentration	Drops	Coverage	Surface Pressure
Unit	mmol/l	Number	$Å^2$/molecule	mN/m
DOPC	0.43	54 ± 5	64 ± 6	11 ± 2
DOCPe	0.43	44 ± 1	77 ± 2	13 ± 1

Stock solutions of DOPC and DOCPe are prepared with the in Table 5.1 given concentration of lipid, dissolved in Chloroform. The monolayers are prepared by dropping the specified amount of 0.25 μl drops of stock solution on D_2O in a rotating teflon trough. The trough has a diameter of 77 mm and is filled with 35 ml D_2O.
A tensiometer is used to measure the surface pressure during monolayer preparation. To obtain similar surface pressure results through the 14 monolayer preparations the drop count of the lipid needs to be adjusted and is the reason for the relative large variance of 10 % in the drop count of DOPC. On average this results in a surface coverage of 64(6) $Å^2$/molecule and 77(2) $Å^2$/molecule at a surface pressure of 11(2) mN/m and 13(1) mN/m for DOPC and DOCPe respectively.[144] To prevent the

lipids from degradation, all sample preparation steps and measurements are performed under N_2 atmosphere.

5.3.2 Surface Pressure Measurement

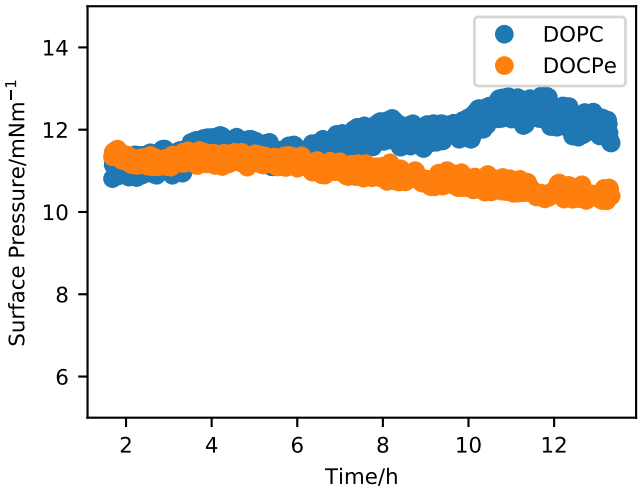

Figure 5.1: Surface pressure measurements on DOCPe and DOPC covered D_2O for 12 h during a pump-probe measurement.

Each pump probe measurement was carried out over a course of 12 h. Figure 5.1 shows that the surface pressure is stable throughout the 12h time period with a slow drift of about 10%, while the water level is kept constant using a reservoir.

5.3.3 Pump Positions

Table 5.2: Mean frequency of the pump IR spectrum and the width (1σ) of a gaussian fit to the Pump IR spectrum.

Mean Frequency/cm^{-1}	2350	2400	2500
Width/cm^{-1}	22	24	45

Three different pump frequencies were used. The position of the pump is determined by measuring the non-resonant Pump-Visible SFG response from a gold sample and the mean position and width is given in Table 5.2.

5.3.4 Heat Correction

Typically D_2O relaxation dynamics are described using a four-level-model[58,60] with two lifetimes $\tau_1 \approx 0.4$ ps and $\tau_2 \approx 0.7$ ps. We approximate the ingrowth of heat using

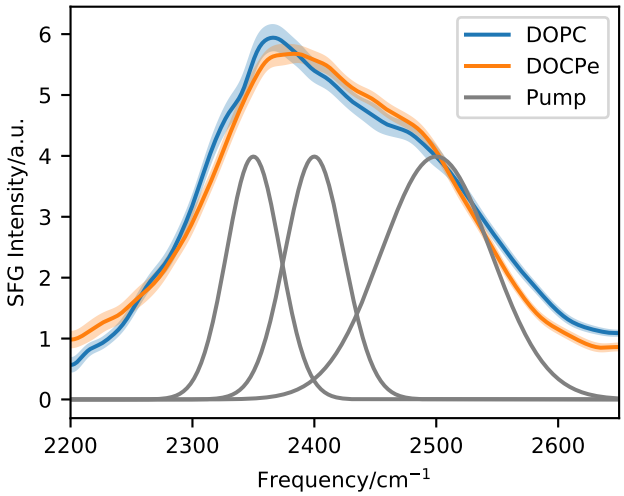

Figure 5.2: SFG of the OD Stretch vibration of the lipid-D_2O interface. The grey curves show the spectra of the IR pump laser beam.

Equation 5.1. With $\tau_{\text{heat}} = 1\,\text{ps}$ and $A(\omega)$ as bleach at $t = 20\,\text{ps}$ at probe frequency ω.

$$H(\omega, t) = A(\omega) \cdot (1 - e^{-t/\tau_{\text{heat}}}) \tag{5.1}$$

Figure 5.3 shows an example for heat corrected pump probe data. Note that this heat correction is only used in Figure 5.5, Figure 5.6 and Figure 5.7, but not in Figure 5.8, where the four-level-model accounts for heating effects.

5.4 Results and Discussion

5.4.1 Static Spectra

Figure 5.4 shows SFG intensity spectra of the DOPC-D_2O and the DOCPe-D_2O interface and the molecular structure of DOPC and DOCPe in the inset. The broad peak from $2200\,\text{cm}^{-1}$ to $2800\,\text{cm}^{-1}$ originates from the OD-stretch vibration of the interfacial water.[33,154] This peak is broadened by a wide distribution of different OD-bond strengths, intermolecular coupling as well as a Fermi resonance with the overtone of the water stretch vibration.[117,119,155–157] No significant difference can be observed between DOPC and DOCPe in the OD-Stretch region of the SFG spectrum. CH-Stretch vibrations of the lipid give rise to the SFG signal between $2800\,\text{cm}^{-1}$ and $2950\,\text{cm}^{-1}$.[144]

Phase-resolved SFG measurements were previously performed on the DOPC- and DOCPe-H_2O interface, showing that the orientation of the interfacial water depends on the headgroup of the lipid.[144] The CPe headgroup showed a net downwards orientation of the interfacial water dipole moment, indicative of the hydrogen atoms pointing

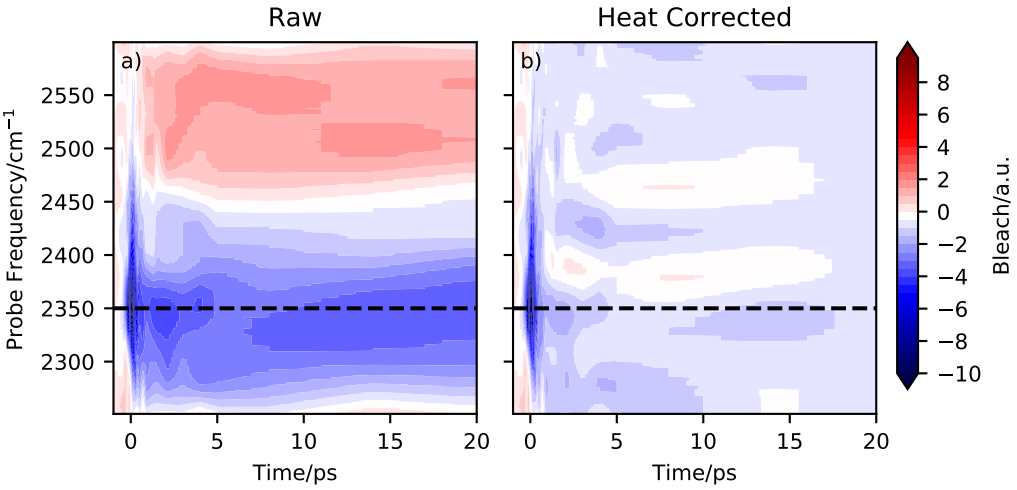

Figure 5.3: Effect of heat correction on Pump-Probe spectra. a) bleach spectrum of DOPC-D_2O interface without heat correction. b) same spectrum after heat correction.

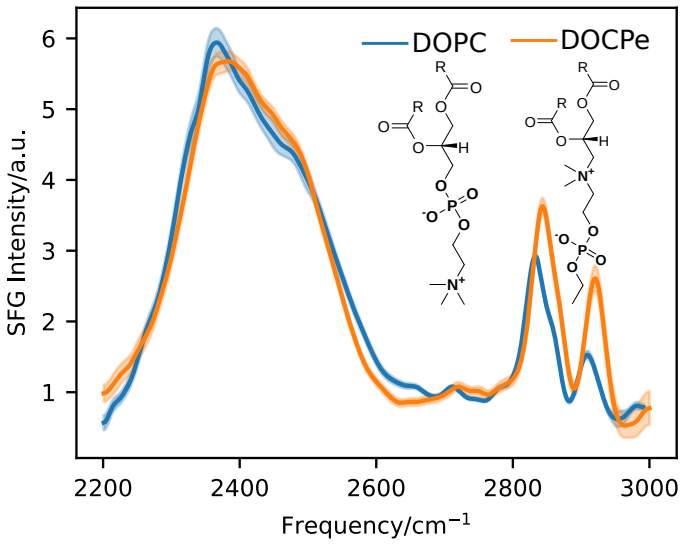

Figure 5.4: Static SFG intensity spectra of DOPC and DOCPe. The inset shows the molecular structure of DOPC and DOCPe.

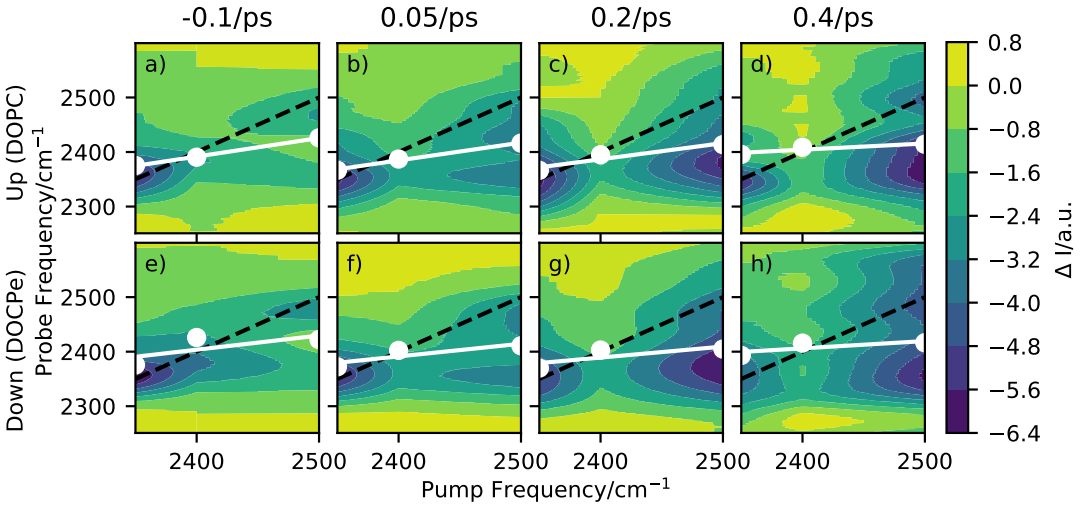

Figure 5.5: 2D-SFG spectra of D_2O in the hydrogen bond OD-stretch region for a) to d) the upwards oriented water (DOPC), and for e) to h) the downwards oriented water (DOCPe), at four different pump-probe time delays. The white dots correspond to a spectral center line. The white line denotes a linear regression through the spectral weight. The black dotted line indicates the pump=probe frequency diagonal.

down towards the bulk. For the PC headgroup the situation is reversed, meaning that the interfacial water hydrogen atoms point on average upwards, away from the bulk phase. The phase-resolved experiments showed as well a small blue shift of the $\mathrm{Im}(\chi^{(2)})$ spectrum of DOPC compared to the $\mathrm{Im}(\chi^{(2)})$ spectrum of DOCPe, indicating slightly weaker hydrogen bonding of water for DOPC.
MD simulations support the hypothesis of the opposing water orientation at the DOPC- and DOCPe-water interface, showing that the orientation of the field in between the choline (+) and the phosphate group (−) determines the orientation of the interfacial water.[158–160] Further, there exists an alternative interpretation based on phase-resolved SFG data and MD simulations of the 1-palmitoyl-2-oleoyl-sn-glycero-3-phosphocholine (POPC) water interface.[151,161] There, three differently bound types of water were proposed to be responsible for the $\mathrm{Im}(\chi^{(2)})$ spectrum of the POPC-water interface. However, the exact molecular mechanism causing the water orientation on zwitterionic headgroups is out of the scope of this work. Instead we study the effect of water orientation on the vibrational dynamics. To do so we use 2D-SFG spectroscopy of the DOPC and DOCPe-water interface

5.4.2 2D-SFG Spectra

Figure 5.5 shows 2D-SFG spectra of upwards (DOPC) and downwards (DOCPe) oriented interfacial water at four different pump-probe time delays. See Figure 5.2 for details on the pump frequency spectrum. The $t = 0\,\mathrm{ps}$ time axis is calibrated by measuring the bleach on a gold sample and setting $t = 0\,\mathrm{ps}$ to the maximum bleach. The color (ΔI) denotes the difference of SFG intensity between the pump beam being on (pumped) and the pump beam beeing off (unpumped). The pumped and the unpumped spectra are corrected for heating effects and normalized to the specific pump power. Details of the heat correction are described in Figure 5.3. The signal ΔI is dominated by a combination of bleach and stimulated emission.[51]
A qualitative comparison of the 2D-SFG spectra of upwards (DOPC) and downwards (DOCPe) oriented water shows no significant differences between the two orientations. As such, we discuss in the following the common spectral features of both water orientations.
The amplitude of ΔI on the diagonal is comparable for a pump beam frequency of $2350\,\mathrm{cm}^{-1}$ and $2500\,\mathrm{cm}^{-1}$, but significantly smaller for a pump beam frequency of $2400\,\mathrm{cm}^{-1}$. At a pump beam frequency of $2350\,\mathrm{cm}^{-1}$, both systems show an instantaneous response at the same probe frequency. At a pump beam frequency of $2400\,\mathrm{cm}^{-1}$ the bleach appears at a lower probe frequency of about $2380\,\mathrm{cm}^{-1}$. Pumping at a central frequency of $2500\,\mathrm{cm}^{-1}$ results in an instantaneous signal at a probe frequency of $2500\,\mathrm{cm}^{-1}$, but after less then $0.2\,\mathrm{ps}$ additional signal is observable at a $2350\,\mathrm{cm}^{-1}$ probe frequency, hinting towards spectral diffusion or a cross-peak.
This cross-peak-like structure, visible at a probe frequency of $2350\,\mathrm{cm}^{-1}$ if pumped at $2500\,\mathrm{cm}^{-1}$ and small-time delays ($0.05\,\mathrm{ps}$), at the lipid water interface has previously been observed for the cetyltrimethylammonium bromide (CTAB) water and SDS-water interfaces.[115,162] However, the interpretations are very different in both cases. Inoue et al.[162] showed in the case of CTAB that the cross-peak vanishes upon isotopic dilution, and assigned it to the coupling of the water stretch mode with the overtone of the bending mode, i.e. the Fermi resonance. Livingstone et al.[115] proposed for the SDS case two types of water, coupling differently with the lipid headgroup and showed that the Fermi resonance cannot account for all observed effects. Work on DPTAP showed only a single broad peak when studied with D_2O and HOD.[60,147]
Overall, the discussion of the origin of the cross-peak is out of the scope of this work. Instead, the goal here is to investigate and highlight the possible effects of interfacial water orientation on interfacial vibrational water dynamics. Because isotopic dilution significantly reduces the signal intensity and thus the signal-to-noise ratio, and does not completely resolve the complication induced by the Fermi resonance, we perform the experiments with D_2O and not HOD to ensure best possible sensitivity regarding differences induced by the interfacial water orientation.
On the downside of this, we must deal with complex coupling dynamics, which we account for by analyzing the data in two ways. At first, we investigate the time evolution for the spectral weight frequency. Afterward, we treat the system as a set of coupled oscillators, with central vibrational frequencies at $2350\,\mathrm{cm}^{-1}$ and $2500\,\mathrm{cm}^{-1}$,

giving rise to two cross-peaks at their respective frequencies.

5.4.3 Determination of the Spectral Weight Line

The spectral weight is determined by taking vertical slices of Figure 5.5 at a given pump beam frequency. The slice is fitted with the sum of two Gaussians and examples for three different pump beam frequencies, at a pump-probe time delay of −0.1 ps are shown in Figure 5.6.

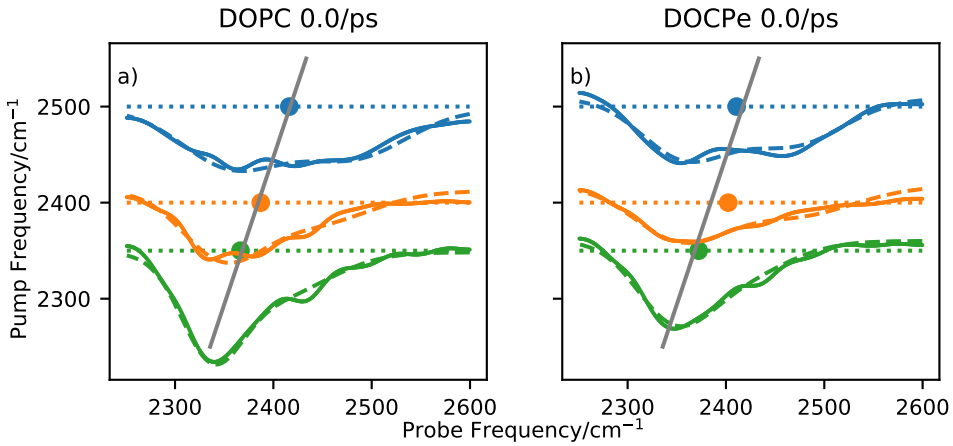

Figure 5.6: Transient SFG spectra of DOPC and DOCPe. The X-Axis shows the probe frequency, while the dotted line on the Y-Axis corresponds to the pump frequency. The distance between dotted and colored line denotes the Δ intensity in a.u. Each point on the dotted line illustrates the SW of Equation 5.3. The grey line is a linear fit through the SW points and corresponds to the white line of Figure 5.5.

In Figure 5.6 the vertical difference of the dotted lines equals the central pump frequency difference and the distance between the dotted and the solid line corresponds to the ΔI of Figure 5.5: e.g. the difference in SFG intensity with pump beam on and pump beam off. The double peak like structure for a pump frequency of 2500 cm^{-1} illustrates, that at least two peaks are needed to describe the data. The fit function has the form:

$$t(\omega) = \sum_{n}^{2} A_n e^{-(\omega-\omega_n)^2/(2\sigma_n^2)} + c_n \tag{5.2}$$

With Amplitude A_n the position ω_n, the offset c_n and the width σ_n of the feature n. The spectral weight is defined as the average of ω_n weighted with A_n. e.g:

$$SW = \frac{\sum_n^2 A_n \cdot \omega_n}{\sum_n^2 A_n} \tag{5.3}$$

SW is shown as a colored dot in Figure 5.6 and as a white dot in Figure 5.5. By plotting the SW vs the central pump beam frequency, the spectral weight line (SWL) can be determined. The SWL is shown as a grey line in Figure 5.6 and as a white line in Figure 5.5.

5.4.4 Time Dependency of the Slope of the Spectral Weight Line

By plotting the slope of the SWL vs the pump-probe time delay, Figure 5.7 is obtained. The time dependency of the SWL is important, as it contains information on spectral diffusion.[163] Figure 5.7 is fitted with the convolution of a Gaussian function and an exponential decay. The function has the form of Equation 5.4. Here the Gaussian accounts for the finite instrument response function and has a fixed with of $\sigma = 0.16$ ps. The start time μ (center of the Gaussian) is fixed to -0.2 ps to reduce the amount of free parameters. The -0.2 ps offset corrects roughly for the different definitions of time zero throughout the experiment and the fit. As Equation 5.4 contains the product of a gaussian and an errorfunction, the amplitude of Equation 5.4 at t=0 is 50 % of the maximum amplitude. However t=0 is experimentally defined by the maximum bleach on gold, as this is easier to determine during the experiment. The exponential decay has a lifetime of τ and is varied together with the Amplitude A to obtain the best fit. The maximum of the SWL is slightly different for the two lipids with DOPC : 0.34 ± 0.04 and DOCPe : 0.25 ± 0.05.

$$SWL(t, \mu, \sigma, \tau, A) = \frac{1}{2} A \exp\left(\frac{2\tau(\mu - t) + \sigma^2}{2\tau^2}\right) \operatorname{erfc}\left(\frac{\sigma^2 + \tau(\mu - t)}{\sqrt{2}\sigma\tau}\right) \tag{5.4}$$

Figure 5.7 shows the time dependency of the SWL modeled with the convolution of Gaussian function and an exponential decay (Equation 5.4). Here the Gaussian function accounts for the instrument response function and has a width of σ=0.16 ps.[58] The exponential decay describes the time scale of the spectral diffusion and shows comparable decay times of 0.47 ps $\pm$ 0.07 ps for DOPC and 0.5 ps $\pm$ 0.1 ps for DOCPe. Previous studies of DPTAP[60,147,148] showed spectral diffusion of the timescale of 0.35 ps for D_2O, 1.1 ps for HOD within the OD-Stretch region and 0.75 ps $\pm$ 0.35 ps for HOD within the OH-Stretch region. Interestingly it seems that a timescale of about 0.5 ps is characteristic for the interfacial spectral diffusion of vibrational energy and is almost independent of the chemical structure of the lipid as well as the isotopic content of the water.
In a study using DPPG as negative and DPTAP as positive lipid, the centerline slope of DPPG and DPTAP were found to be significantly different.[147,148] This difference was attributed to an ultrafast, but invisible process occurring on a sub-0.1 ps timescale and was attributed to water orientation in the direct vicinity of water in contact with the lipids. The DPPG/DPTAP study used phase-resolved 2D-SFG, but as explained in[51] the two methods probe fundamentally the same dynamic properties. Instead, our results suggest that the orientation of water in the direct vicinity of DOPC and DOCPe seems to be unimportant for spectral diffusion of the OD-Stretch vibration, because both amplitude and temporal evolution of the SWL are comparable within

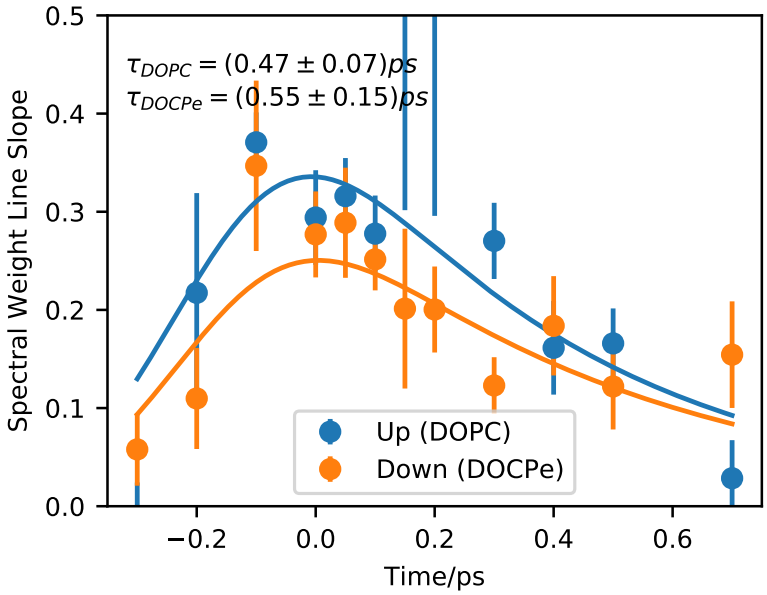

Figure 5.7: Spectral weight line slope of the interfacial OD-stretch vibration of D_2O covered with a mono layer of DOPC and DOCPe as a function of pump-probe delay time. Solid line shows a fit of Equation 5.4.

the uncertainty of the experiment. Hence, a comparison between the results of Tahara and co-workers[147,148] and the present work, highlights the importance of the detailed chemical environments that different lipids constitute for the water. The orientational arrangement of water for the DPPG and DPTAP headgroups are caused by the net charge on the head groups. In contrast, the reorientation of water for DOPC and DOCPe is the result of the change of the electric field direction in the headgroup region, and not of a sign change of the net charge of the lipid headgroups. In the following, we switch to the interpretation of Figure 5.5 and analyze the 2D-SFG spectra by assuming two coupled oscillators at $2350\,\mathrm{cm}^{-1}$ and $2500\,\mathrm{cm}^{-1}$.

5.4.5 Dynamics

The traces shown in Figure 5.8 are obtained by averaging vertical areas of probe frequencies at $2350\,\mathrm{cm}^{-1} \pm 30\,\mathrm{cm}^{-1}$, $2400\,\mathrm{cm}^{-1} \pm 30\,\mathrm{cm}^{-1}$ and $2500\,\mathrm{cm}^{-1} \pm 30\,\mathrm{cm}^{-1}$ at a given pump frequency and plotted *vs.* the pump-probe time delay. $30\,\mathrm{cm}^{-1}$ corresponds roughly to the $1\,\sigma$ spectral width of the pump pulse (see Figure 5.2). If the central pump frequency equals the probe frequency, the trace is labeled "Diagonal". At a central pump frequency of $2350\,\mathrm{cm}^{-1}$ the "Cross Up" labeled trace is centered around a probe frequency of $2500\,\mathrm{cm}^{-1}$ and describes an uphill energy transport process. At the $2500\,\mathrm{cm}^{-1}$ pump frequency, the "Cross Down" labeled trace is centered around a probe frequency of $2350\,\mathrm{cm}^{-1}$ and describes a downhill energy transport process. Note

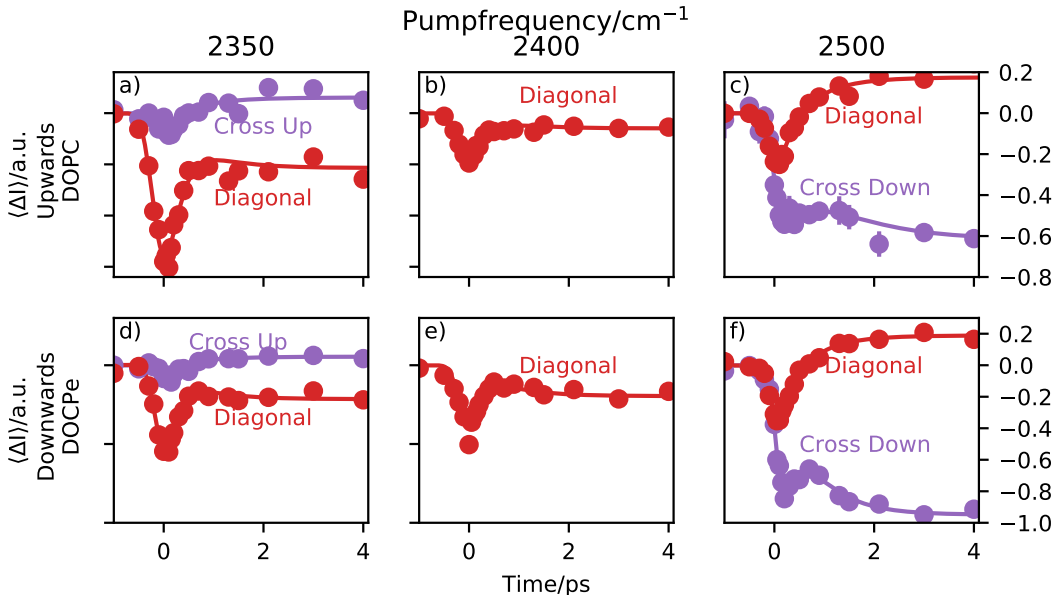

Figure 5.8: Traces of three different central pump frequencies. The "Diagonal" labeled traces are obtained by averaging areas of Figure 5.5, where the central pump frequency equals the central probe frequency. The "Cross" labeled traces have a central probe frequency of 2500 cm^{-1} if pumped at 2350 cm^{-1} and vice versa if pumped at 2500 cm^{-1}. The direction of energy transfer is labeled with "Up" for uphill and "Down" for downhill energy transfer.

that the traces in Figure 5.8 contain no heat correction, unlike the 2D-SFG spectra in Figure 5.5. Heating effects are accounted for within the fitting model and thus they do not need to be subtracted beforehand.[47,58–60,115]

A trace consists of three sections. For negative times, e.g. the probe pulse arrives at the sample before the pump pulse and consequently, the trace is a flat line below 0 ps. As the pump and the probe start to overlap, the transient signal appears. The point in time, where the signal has reached about 50 % of its amplitude is called the lag time and the duration of the signal rise is determined by the instrument response function of the setup. Following, one observes the relaxation of the system. This is due to the relaxation of the pump-induced vibrational excitation and reflects the lifetime of the excited vibrational state. Due to heating effects, the final state after >4 ps is not necessarily the initial state but can be different.

Heat weakens the hydrogen bonds and shifts the spectrum towards higher frequencies. Consequently, the spectral intensity increases at around a probe frequency of 2500 cm^{-1} and decreases at a probe frequency of 2350 cm^{-1}. This is the cause for a positive ΔI in Figure 5.8 at a probe frequency of 2500 cm^{-1} and negative ΔI at a probe frequency of 2350 cm^{-1}.

At a central pump frequency of 2350 cm^{-1}, a relatively large bleach of the diagonal peak for both water orientations (DOPC and DOCPe) is observed. With a delay of about 0.2 ps we see a much weaker, but still significant bleach in the cross-peak region. After about 1 ps the dynamic processes have largely ended. At a central pump frequency of 2400 cm^{-1} it is not possible to define a cross-peak, and thus only the diagonal trace is shown. Tuning the pump frequency to 2500 cm^{-1} reveals an interesting dynamic structure. There is significant bleach visible for the diagonal peak, but also for the cross-peak. This hints towards spectral diffusion from the diagonal peak downhill towards the cross-peak. Note that no significant qualitative differences between the observed dynamics for the two opposite water orientations are found. The reproducible bump, visible in e.g. the blue trace in Figure 5.8 f), makes it clear that at least a two-lifetime model is needed to describe the data.

Depending on the nature of the coupling, the ingrowth of the cross-peak can be delayed relative to that of the diagonal peak. Indeed such a delay can be found in Figure 5.8, if the lag times of the diagonal and cross-peak are compared. Here the lag time is obtained from the fits of Figure 5.8, and corresponds to the point in time when the trace has reached 50 % of its maximum height. The result is, that if pumped at 2350 cm^{-1}, the uphill cross peak appears about 0.2 ps after the diagonal peak. The situation is similar if pumped at 2500 cm^{-1}, where the diagonal peak appears about 0.1 ps prior to the downhill cross-peak. To exclude instrumental artifacts as the source of the lag time difference, the same analysis has been performed on gold, showing lag times of at most 40 fs ± 10 fs. This observation is consistent with near-resonant vibrational energy transfer. However for the upwards (DOPC) and the downwards (DOCPe) oriented water, there is no significant difference in the lag times.

The traces are fitted with the four-level-model commonly used.[18,60,164] The inset of Figure 5.9 shows the energy levels postulated by the model. For further details see a previous publication, where the analytical solution to this model was presented.[58] The

lifetime of the vibrationally excited state amounts to τ_1, with the system decaying into an intermediate state. The decay from the intermediate state into a heated ground state is characterized by a lifetime of τ_2 for which 0.7 ps has been used.[58,165] Using this model, we obtain the lifetime of the excited vibrational states for different interfacial water orientation

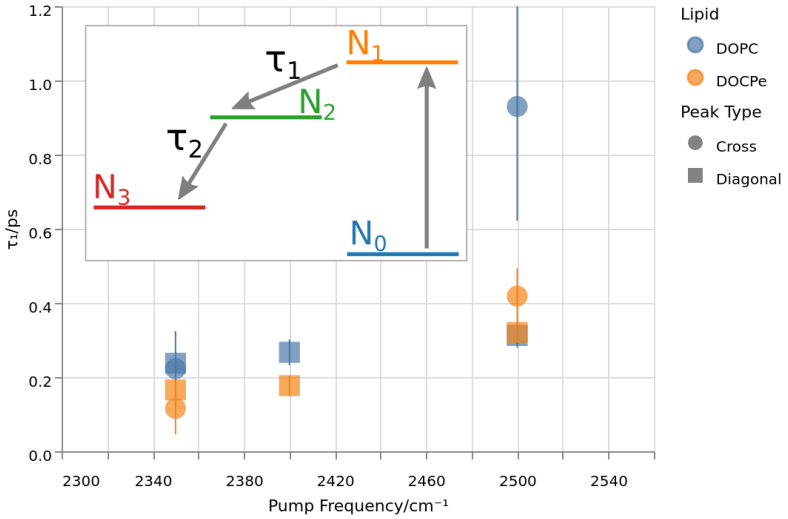

Figure 5.9: Lifetimes of the excited vibrational state τ_1 as function of the pump frequency. The colors denote the lipid, while the shape corresponds to the selected peak. The inset shows the energy levels of the four-level-model used to extract τ_1 by fitting the data of Figure 5.8.

Figure 5.9 shows τ_1 lifetimes extracted from the four-level-model. Overall the vibrational dynamics are fast at a pump frequency of 2350 cm^{-1} with lifetimes around 0.2 ps. Upon increasing pump frequencies, the lifetimes increase to τ_1 greater than 0.4 ps at a central pump frequency of 2500 cm^{-1}. A similar trend has already been reported for the neat water-air, as well as the water-DPTAP interface.[58,60,114] At the lowest pump frequency, there is neither a significant difference between the cross and diagonal peaks, nor between the opposing water orientations. At 2400 cm^{-1} pump frequency, there is a 1 σ difference between the two water orientations, and at the 2500 cm^{-1} pump frequency, there is no significant difference between the lipids for the diagonal peak, but a 1 σ difference in τ_1 at the cross-peak lifetime for the two water orientations. The overall impression of Figure 5.9 could be that DOPC shows a slightly larger τ_1 then DOCPe. However one has to keep in mind, that the error bars of Figure 5.9 do not account for correlation effects of the fit parameters. A significant improvement in the signal to noise ratio would be needed to consolidate this observation.

5.5 Conclusion

We have investigated the influence of the water orientation on the dynamics of the interfacial OD-Stretch vibration of D_2O. 2D-SFG spectroscopy of oppositely oriented water interfaces reveal no significant differences of neither the time dependency of the SWL, nor the vibrational lifetimes of a potential cross or diagonal peak. These results contrast previous findings,[147,148] where the water orientation, resulting from charged headgroups, was identified as the cause of dynamical changes. For the present results, the orientation is induced by the lipid headgroup dipolar field. Because the interfacial water vibrational response and dynamics are independent of water orientation at the DOPC- and DOCPe-water interfaces, we conclude that the properties of water cannot explain the biological differences between DOPC and DOCPe on a molecular level.

6 Conclusion and Outlook

Obviously, the spectroscopic research of water is challenging but also rewarding. Using surface-sensitive spectroscopic methods, it is finally possible to investigate the behavior of soft matter at interfaces on a molecular scale. In this thesis, the molecular dynamics of interfacial water at various interfaces is studied. As a method of choice, we use sum-frequency generation (SFG) spectroscopy. Due to its spectroscopic symmetry selection rules, SFG is surface specific for centrosymmetric media. With a pump-probe measurement scheme, it is possible to excite molecular vibrational states and follow the relaxation process on the sub ps time scale. By tuning the center frequency of the pump laser, it is possible to obtain two-dimensional spectroscopic data and study vibrational coupling. On water, this reports on the complex and rich interfacial substructure of the water hydrogen bond network that, in turn, is sensitive to, e.g. electrolytes or lipids itself.
In Chapter 3, the interfacial structure of water in contact with the negatively surface charged muscovite mica is investigated. By exchanging surface cations on muscovite mica, the heterogeneous ice nucleation temperature can be altered. The lowest ice nucleation temperature of $-26\,^{\circ}\mathrm{C}$ is observed for Na-Mica, while the highest ice nucleation temperature of $-20\,^{\circ}\mathrm{C}$ is observed on H-Mica. By using SFG spectroscopy, it is revealed that the average water alignment depends on the mica surface cation. The highest average water alignment is found for Na-Mica, and the lowest for H-Mica. This indicates that the water hydrogen bond network is aligned in the Na-Mica case hindering the formation of ice crystals. The opposite happens for the H-Mica interface, where the formation of ice crystals is not hindered. With this ordering mechanism both, the SFG and the ice nucleation temperature results can be explained. However, there also remain some issues, as, e.g., the ice nucleation temperature of Cs-Mica and K-Mica are significantly different with $-23\,^{\circ}\mathrm{C}$ and $-25\,^{\circ}\mathrm{C}$, but the average SFG intensity, and thus probably the average water alignment, is indistinguishable for these two interfaces. Most likely heterogeneous ice nucleation is affected by multiple molecular mechanisms, and water alignment is one amongst others. E.g., the distortion of the interfacial crystal structure due to surface cations could play an important role in all of the mentioned cases as well.
In Chapter 4, the influence of electrolytes on the vibrational dynamics of interfacial water is investigated. It is shown that a significant difference between the interfacial vibrational spectrum of Na_2SO_4-D_2O-Air, Na_2CO_3-D_2O-Air, and D_2O-Air exists. This could be explained by both salts Na_2SO_4 and Na_2CO_3 strengthening the interfacial hydrogen bond network. However in the case of Na_2SO_4 the spectral difference could also be caused by a bulk term, where an electric field due to spatial charge separation of the anion and the cation add a term proportional to $E\chi^{(3)}$ to the observed SFG

spectrum. The same effect is not sufficient to describe the spectral changes induced by Na_2CO_3. By performing pump-probe SFG experiments for various central pump frequencies, the vibrational dynamics of the interfacial water is studied. With pump-probe SFG, differences in energy transfer and vibrational coupling can be investigated. Here, no significant difference in the vibrational dynamics of neat-D_2O, Na_2SO_4-D_2O and Na_2CO_3-D_2O can be observed. A common four-level-model, describing dissipation of energy from the excited state via in intermediate state into a heated ground state, is used to describe the observed pump-probe traces and the extracted lifetimes are, within the uncertainty of the experiment, identical. For the analysis of the measurement, an analytical solution to the four-level model, previously not used in the SFG community, is introduced.
In chapter 5 the effect of oppositely oriented water on the vibrational dynamics is investigated. For this, we compare the two lipid water interfaces of DOPC and DOCPe. DOPC is known to align the average water dipole moment downwards, away from the lipid interface, while DOCPe aligns the average water dipole moment upwards, towards the lipid interface. The only chemical difference between the two lipids is the ordering of the positively charged choline and the negatively charged phosphate group within the headgroup. The orientational flip of the interfacial water is thus assumed to be an effect of the electrical field reversal throughout the lipid head group. By performing a 2D pump-probe SFG experiment, it is found that neither the slope of the spectral weight line, nor the vibrational dynamics of the pump-probe traces show any significant difference. The conclusion is thus that interfacial lipid-bound water dynamics is independent of water orientation. However by comparison with DPTAP and DPPG water interfaces, the same conclusion is not necessarily true for chemically induced water orientation.
The common element of the presented results is water at interfaces. However, there is also a struggle for significance and reproducibility in all of the shown. The SFG signal of the mica-water and the lipid-water interface is relatively strong, and thus the main noise contribution is the photon shot noise. However, the SFG intensity of the electrolyte-water-air interface is significantly weaker, making the electronic noise of the readout system an additional significant noise contributor. Thus a careful signal to noise ratio analysis is imperative. Here a phase-resolved SFG setup could help to lower the detection threshold. In particular, pump-probe SFG experiments benefit substantially from a lower detection threshold, as this can decrease measurement time and thus increase the amount of data, improving the statistical significance of the results.
Personally, I think the brightest part of the future of 2D-SFG lies ahead of us. However, not a single, but a collection of challenging experimental obstacles are blocking the way forward. Interesting discoveries of, in particular, the neat water-air interface are currently hiding below detection threshold and reproducibility issues. For one, there is the overall complexity of the 2D-SFG setup, that imposes a steep and long learning curve for the experimentalist, with many possible points of failure along the road. Here more automation could certainly help. Secondly, automation can also help to tackle reproducibility issues, because simpler measurement routines allow for

more statistical evidence, as repetition would be less time-consuming. Third, there is certainly room for improving the S/N ratio by expanding towards a co-linear phase-resolved 2D-SFG setup. By using a phase-resolved setup, in particular low-intensity SFG systems, like neat water-air, could benefit from shorter integration times. The strongest weakness of ordinary phase-resolved SFG setups is that they are sensitive to sample height variations on the level of the visible wavelength. However, this issue can be mitigated by using a co-linear phase-resolved SFG setup. In conjunction with a pulse shaped narrowband excitation setup, currently unknown vibrational coupling between different modes might be detectable in the near future.
On the system side, water will remain a hot topic for the foreseeable future. E.g., the vibrational dynamics of Eigen- and Zundel-states at the interface is under investigation. Currently, there are two approaches to investigate the dynamics of the water excess proton complex experimentally. The direct approach is, to compare the vibrational structure and dynamics of neat water and of e.g. aqueous hydrochloric acid. This has been successfully carried out for bulk water systems. However, the excess proton-induced vibrational features, extend over at least $2000\,\mathrm{cm}^{-1}$ and are only visible as distortions to the neat water vibrational spectrum.[53] This makes improvements of the S/N ratio imperative, if surface-specific data is desired. But, there also exists an alternative, intrinsically surface-specific approach. Here one studies the interaction of water at negatively charged surfaces. A negatively charged surface can give rise to an intense H_3O^+ Eigen like stretch signal at $2550\,\mathrm{cm}^{-1}$.[166] This signal can have an SFG intensity on the same order as the OH-stretch signal. Hypothetically this should make the investigation of the dynamics of the H_3O^+ system at negatively charged surfaces feasible. Hopefully, such a measurement will provide new insights into the nature of the vibrational dynamics of Eigen- and maybe even Zundel-states at interfaces.

Bibliography

[1] V. D. Kobtsev, D. N. Kozlov, S. A. Kostritsa, V. V. Smirnov, and O. M. Stel'makh.
Temperature fluctuations in turbulent flame measured using coherent anti-stokes raman scattering.
Technical Physics Letters, 41(8):756–758, Aug 2015.

[2] C. Eliasson, N. A. Macleod, and P. Matousek.
Noninvasive detection of concealed liquid explosives using raman spectroscopy.
Analytical Chemistry, 79(21):8185–8189, 2007.
PMID: 17880183.

[3] Joanna S. Day, Howell G.M. Edwards, Steven A. Dobrowski, and Alison M. Voice.
The detection of drugs of abuse in fingerprints using raman spectroscopy i: latent fingerprints.
Spectrochimica Acta Part A: Molecular and Biomolecular Spectroscopy, 60(3):563 – 568, 2004.

[4] Ketan Gajjar, Júlio Trevisan, Gemma Owens, Patrick J Keating, Nicholas J Wood, Helen F Stringfellow, Pierre L Martin-Hirsch, and Francis L Martin.
Fourier-transform infrared spectroscopy coupled with a classification machine for the analysis of blood plasma or serum: A novel diagnostic approach for ovarian cancer.
Analyst, 138(14):3917–3926, 2013.

[5] Heike Arnolds and Mischa Bonn.
Ultrafast surface vibrational dynamics.
Surface Science Reports, 65(2):45 – 66, 2010.

[6] W. Kauzmann, C. B. Anfinsen, M. L. Anson, Kenneth Bailey, and John T. Edsall.
Some factors in the interpretation of protein denaturation11the preparation of this article has been assisted by a grant from the national science foundation.
In *Advances in Protein Chemistry*, volume 14, pages 1–63. Academic Press, 1959.

[7] Margaret S. Cheung, Angel E. García, and José N. Onuchic.
Protein folding mediated by solvation: Water expulsion and formation of the hydrophobic core occur after the structural collapse.
Proceedings of the National Academy of Sciences, 99(2):685–690, 2002.

[8] Martin Chaplin.
Do we underestimate the importance of water in cell biology?

Nature Reviews Molecular Cell Biology, 7(11):861–866, 2006.

[9] Yaakov Levy and José N. Onuchic.
Water mediation in protein folding and molecular recognition.
Annual Review of Biophysics and Biomolecular Structure, 35(1):389–415, 2006.
PMID: 16689642.

[10] S. E. Bauer, Y. Balkanski, M. Schulz, D. A. Hauglustaine, and F. Dentener.
Global modeling of heterogeneous chemistry on mineral aerosol surfaces: Influence on tropospheric ozone chemistry and comparison to observations.
Journal of Geophysical Research: Atmospheres, 109(D2), 2004.

[11] BJ Murray, D O'sullivan, JD Atkinson, and ME Webb.
Ice nucleation by particles immersed in supercooled cloud droplets.
Chemical Society Reviews, 41(19):6519–6554, 2012.

[12] James D Atkinson, Benjamin J Murray, Matthew T Woodhouse, Thomas F Whale, Kelly J Baustian, Kenneth S Carslaw, Steven Dobbie, Daniel O'Sullivan, and Tamsin L Malkin.
The importance of feldspar for ice nucleation by mineral dust in mixed-phase clouds.
Nature, 498(7454):355, 2013.

[13] Wendell M. Latimer and Worth H. Rodebush.
Polarity and ionization from the standpoint of the lewis theory of valence.
J. Am. Chem. Soc., 42(7):1419–1433, July 1920.

[14] Jordi Fraxedas.
Water at Interfaces: A Molecular Approach.
CRC Press, 2014.

[15] Alenka Luzar and David Chandler.
Hydrogen-bond kinetics in liquid water.
Nature, 379(6560):55–57, 1996.

[16] Anders Nilsson and Lars G. M. Pettersson.
The structural origin of anomalous properties of liquid water.
Nature Communications, 6(1):8998, 2015.

[17] Rossend Rey, Klaus B. Møller, and James T. Hynes.
Hydrogen bond dynamics in water and ultrafast infrared spectroscopy.
The Journal of Physical Chemistry A, 106(50):11993–11996, 2002.

[18] Jörg Lindner, Peter Vöhringer, Maxim S. Pshenichnikov, Dan Cringus, Douwe A. Wiersma, and Maxim Mostovoy.
Vibrational relaxation of pure liquid water.
Chemical Physics Letters, 421(4):329 – 333, 2006.

[19] YR Shen.
Fundamentals of sum-frequency spectroscopy.
Cambridge University Press, 2016.

[20] Yuen-Ron Shen.
The principles of nonlinear optics.
New York, Wiley-Interscience, 1984, 575 p., 1984.

[21] P. A. Franken, A. E. Hill, C. W. Peters, and G. Weinreich.
Generation of optical harmonics.
PRL, 7(4):118–119, August 1961.

[22] M. Bass, P. A. Franken, A. E. Hill, C. W. Peters, and G. Weinreich.
Optical mixing.
Phys. Rev. Lett., 8:18–18, Jan 1962.

[23] X. D. Zhu, Hajo Suhr, and Y. R. Shen.
Surface vibrational spectroscopy by infrared-visible sum frequency generation.
Phys. Rev. B, 35:3047–3050, Feb 1987.

[24] James P Smith and Vicki Hinson-Smith.
Product review: Sfg coming of age, 2004.

[25] Shaul Mukamel.
Principles of Nonlinear Optical Spectroscopy, volume 29.
Oxford university press New York, 1995.

[26] Peter Hamm.
Principles of nonlinear optical spectroscopy: A practical approach or: Mukamel for dummies.
University of Zurich, 41(5):77, 2005.

[27] Robert W Boyd.
Nonlinear optics.
Elsevier, 2003.

[28] Wei Gan, Bao-hua Wu, Zhen Zhang, Yuan Guo, and Hong-fei Wang.
Vibrational spectra and molecular orientation with experimental configuration analysis in surface sum frequency generation (sfg).
The Journal of Physical Chemistry C, 111(25):8716–8725, 2007.

[29] Chiaki Hirose, Naotoshi Akamatsu, and Kazunari Domen.
Formulas for the analysis of the surface sfg spectrum and transformation coefficients of cartesian sfg tensor components.
Appl. Spectrosc., 46(6):1051–1072, Jun 1992.

[30] Hong-Fei Wang, Wei Gan, Rong Lu, Yi Rao, and Bao-Hua Wu.
Quantitative spectral and orientational analysis in surface sum frequency generation vibrational spectroscopy (sfg-vs).
International Reviews in Physical Chemistry, 24(2):191–256, 2005.

[31] Alex G. Lambert, Paul B. Davies, and David J. Neivandt.
Implementing the theory of sum frequency generation vibrational spectroscopy: A tutorial review.
Applied Spectroscopy Reviews, 40(2):103–145, 2005.

[32] Michael Falk and TA Ford.
Infrared spectrum and structure of liquid water.
Canadian Journal of Chemistry, 44(14):1699–1707, 1966.

[33] Q. Du, R. Superfine, E. Freysz, and Y. R. Shen.
Vibrational spectroscopy of water at the vapor/water interface.
Phys. Rev. Lett., 70:2313–2316, Apr 1993.

[34] Donna Strickland and Gerard Mourou.
Compression of amplified chirped optical pulses.
Optics communications, 56(3):219–221, 1985.

[35] D. E. Spence, P. N. Kean, and W. Sibbett.
60-fsec pulse generation from a self-mode-locked ti:sapphire laser.
Opt. Lett., 16(1):42–44, Jan 1991.

[36] X. Zhuang, P. B. Miranda, D. Kim, and Y. R. Shen.
Mapping molecular orientation and conformation at interfaces by surface nonlinear optics.
Phys. Rev. B, 59:12632–12640, May 1999.

[37] Xing Wei, Seok-Cheol Hong, Xiaowei Zhuang, Tomohisa Goto, and Y. R. Shen.
Nonlinear optical studies of liquid crystal alignment on a rubbed polyvinyl alcohol surface.
Phys. Rev. E, 62:5160–5172, Oct 2000.

[38] Ellen H. G. Backus, Nuria Garcia-Araez, Mischa Bonn, and Huib J. Bakker.
On the role of fresnel factors in sum-frequency generation spectroscopy of metal–water and metal-oxide–water interfaces.
The Journal of Physical Chemistry C, 116(44):23351–23361, 2012.

[39] Wei Gan, Dan Wu, Zhen Zhang, Ran-ran Feng, and Hong-fei Wang.
Polarization and experimental configuration analyses of sum frequency generation vibrational spectra, structure, and orientational motion of the air/water interface.
J. Chem. Phys., 124(11):114705, March 2006.

[40] Xiao-Hua Hu, Feng Wei, Hui Wang, and Hong-Fei Wang.
α-quartz crystal as absolute intensity and phase standard in sum-frequency generation vibrational spectroscopy.
J. Phys. Chem. C, 123(24):15071–15086, June 2019.

[41] R. Superfine, J. Y. Huang, and Y. R. Shen.
Phase measurement for surface infrared-visible sum-frequency generation.
Opt. Lett., 15(22):1276–1278, Nov 1990.

[42] Igor V. Stiopkin, Himali D. Jayathilake, Andrey N. Bordenyuk, and Alexander V. Benderskii.
Heterodyne-detected vibrational sum frequency generation spectroscopy.
Journal of the American Chemical Society, 130(7):2271–2275, 2008.
PMID: 18217755.

[43] H. Held, A. I. Lvovsky, X. Wei, and Y. R. Shen.
Bulk contribution from isotropic media in surface sum-frequency generation.
Phys. Rev. B, 66:205110, Nov 2002.

[44] Grazia Gonella, Cornelis Lütgebaucks, Alex G. F. de Beer, and Sylvie Roke.
Second harmonic and sum-frequency generation from aqueous interfaces is modulated by interference.
J. Phys. Chem. C, 120(17):9165–9173, May 2016.

[45] Yu-Chieh Wen, Shuai Zha, Xing Liu, Shanshan Yang, Pan Guo, Guosheng Shi, Haiping Fang, Y. Ron Shen, and Chuanshan Tian.
Unveiling microscopic structures of charged water interfaces by surface-specific vibrational spectroscopy.
Phys. Rev. Lett., 116:016101, Jan 2016.

[46] Jan Schaefer, Grazia Gonella, Mischa Bonn, and Ellen H G Backus.
Surface-specific vibrational spectroscopy of the water/silica interface: Screening and interference.
Physical chemistry chemical physics : PCCP, 19(25):16875—16880, June 2017.

[47] John A. McGuire and Y. Ron Shen.
Ultrafast vibrational dynamics at water interfaces.
Science, 313(5795):1945–1948, 2006.

[48] Michael D. Fayer, David E. Moilanen, Daryl Wong, Daniel E. Rosenfeld, Emily E. Fenn, and Sungnam Park.
Water dynamics in salt solutions studied with ultrafast two-dimensional infrared (2D IR) vibrational echo spectroscopy.
Accounts of Chemical Research, 42(9):1210–1219, 2009.
PMID: 19378969.

[49] Cho-Shuen Hsieh, Masanari Okuno, Johannes Hunger, Ellen H. G. Backus, Yuki Nagata, and Mischa Bonn.
Aqueous heterogeneity at the air/water interface revealed by 2D-HD-SFG spectroscopy.
Angewandte Chemie International Edition, 53(31):8146–8149, 2014.

[50] Thomas la Cour Jansen.
Multi-dimensional spectroscopy.
2009.

[51] Ellen H. G. Backus, Jenée D. Cyran, Maksim Grechko, Yuki Nagata, and Mischa Bonn.
Time-resolved sum frequency generation spectroscopy: A quantitative comparison between intensity and phase-resolved spectroscopy.
The Journal of Physical Chemistry A, 122(9):2401–2410, 2018.
PMID: 29432016.

[52] John B. Asbury, Tobias Steinel, Kyungwon Kwak, S. A. Corcelli, C. P. Lawrence, J. L. Skinner, and M. D. Fayer.

Dynamics of water probed with vibrational echo correlation spectroscopy.
The Journal of Chemical Physics, 121(24):12431–12446, 2004.

[53] Martin Thämer, Luigi De Marco, Krupa Ramasesha, Aritra Mandal, and Andrei Tokmakoff.
Ultrafast 2d ir spectroscopy of the excess proton in liquid water.
Science, 350(6256):78–82, 2015.

[54] Maksim Grechko, Taisuke Hasegawa, Francesco D'Angelo, Hironobu Ito, Dmitry Turchinovich, Yuki Nagata, and Mischa Bonn.
Coupling between intra- and intermolecular motions in liquid water revealed by two-dimensional terahertz-infrared-visible spectroscopy.
Nature Communications, 9(1):885, 2018.

[55] Han-Kwang Nienhuys, Sander Woutersen, Rutger A. van Santen, and Huib J. Bakker.
Mechanism for vibrational relaxation in water investigated by femtosecond infrared spectroscopy.
The Journal of Chemical Physics, 111(4):1494–1500, 1999.

[56] M. L. Cowan, B. D. Bruner, N. Huse, J. R. Dwyer, B. Chugh, E. T. J. Nibbering, T. Elsaesser, and R. J. D. Miller.
Ultrafast memory loss and energy redistribution in the hydrogen bond network of liquid H_2O.
Nature, 434(7030):199–202, March 2005.

[57] Marc Smits, Avishek Ghosh, Martin Sterrer, Michiel Müller, and Mischa Bonn.
Ultrafast vibrational energy transfer between surface and bulk water at the air-water interface.
Phys. Rev. Lett., 98:098302, Mar 2007.

[58] Malte Deiseroth, Mischa Bonn, and Ellen H. G. Backus.
Electrolytes change the interfacial water structure but not the vibrational dynamics.
The Journal of Physical Chemistry B, 123(40):8610–8616, 2019.
PMID: 31513402.

[59] Tobias Steinel, John B. Asbury, Junrong Zheng, and M. D. Fayer.
Watching hydrogen bonds break: a transient absorption study of water.
The Journal of Physical Chemistry A, 108(50):10957–10964, 2004.
PMID: 19096727.

[60] Ruth A. Livingstone, Zhen Zhang, Lukasz Piatkowski, Huib J. Bakker, Johannes Hunger, Mischa Bonn, and Ellen H. G. Backus.
Water in contact with a cationic lipid exhibits bulklike vibrational dynamics.
The Journal of Physical Chemistry B, 120(38):10069–10078, 2016.
PMID: 27564997.

[61] Cho-Shuen Hsieh, Huib J. Bakker, Lukasz Piatkowski, and Mischa Bonn.

Gigahertz modulation of femtosecond time-resolved surface sum-frequency generation due to acoustic strain pulses.
J. Phys. Chem. C, 118(36):20875–20880, September 2014.

[62] Joseph J. Loparo, Sean T. Roberts, and Andrei Tokmakoff.
Multidimensional infrared spectroscopy of water. i. vibrational dynamics in two-dimensional IR line shapes.
The Journal of Chemical Physics, 125(19):194521, 2006.

[63] Ellen H. G. Backus, Daniel Bonn, Sophie Cantin, Sylvie Roke, and Mischa Bonn.
Laser-heating-induced displacement of surfactants on the water surface.
The Journal of Physical Chemistry B, 116(9):2703–2712, 2012.
PMID: 22324652.

[64] Shenglin Jin, Yuan Liu, Malte Deiseroth, Jie Liu, Ellen H. G. Backus, Hui Li, Han Xue, Lishan Zhao, Xiao Cheng Zeng, Mischa Bonn, and Jianjun Wang.
Use of ion exchange to regulate the heterogeneous ice nucleation efficiency of mica.
J. Am. Chem. Soc., September 2020.

[65] Daniel Rosenfeld, Steven Sherwood, Robert Wood, and Leo Donner.
Climate effects of aerosol-cloud interactions.
Science, 343(6169):379–380, 2014.

[66] Anand Kumar, Claudia Marcolli, and Thomas Peter.
Ice nucleation activity of silicates and aluminosilicates in pure water and aqueous solutions-part 3: Aluminosilicates.
Atmospheric Chemistry and Physics, 19(9):6059–6084, 2019.

[67] Cindy E Morris, Franz Conen, J Alex Huffman, Vaughan Phillips, Ulrich Pöschl, and David C Sands.
Bioprecipitation: A feedback cycle linking earth history, ecosystem dynamics and land use through biological ice nucleators in the atmosphere.
Global change biology, 20(2):341–351, 2014.

[68] Thorsten Bartels-Rausch.
Chemistry: Ten things we need to know about ice and snow.
Nature, 494(7435):27, 2013.

[69] Daniel A Knopf, Peter A Alpert, and Bingbing Wang.
The role of organic aerosol in atmospheric ice nucleation: A review.
ACS Earth and Space Chemistry, 2(3):168–202, 2018.

[70] Thomas Koop, Beiping Luo, Athanasios Tsias, and Thomas Peter.
Water activity as the determinant for homogeneous ice nucleation in aqueous solutions.
Nature, 406(6796):611, 2000.

[71] B. Zobrist, C. Marcolli, T. Peter, and T. Koop.
Heterogeneous ice nucleation in aqueous solutions: the role of water activity.
J. Phys. Chem. A, 112(17):3965–3975, May 2008.

[72] Jianyong Lv, Yanlin Song, Lei Jiang, and Jianjun Wang.
Bio-inspired strategies for anti-icing.
ACS Nano, 8(4):3152–3169, April 2014.

[73] Shuwang Wu, Zhiyuan He, Jinger Zang, Shenglin Jin, Zuowei Wang, Jianping Wang, Yefeng Yao, and Jianjun Wang.
Heterogeneous ice nucleation correlates with bulk-like interfacial water.
Science Advances, 5(4), 2019.

[74] Qiang Wang, Lishan Zhao, Chenxi Li, and Zexian Cao.
The decisive role of free water in determining homogenous ice nucleation behavior of aqueous solutions.
Scientific Reports, 6(1):26831, 2016.

[75] Anand Kumar, Claudia Marcolli, Beiping Luo, and Thomas Peter.
Ice nucleation activity of silicates and aluminosilicates in pure water and aqueous solutions–part 1: The k-feldspar microcline.
Atmospheric Chemistry and Physics, 18(10):7057–7079, 2018.

[76] Hiroki Watanabe, Takuhiro Otsuka, Makoto Harada, and Tetsuo Okada.
Imbalance between anion and cation distribution at ice interface with liquid phase in frozen electrolyte as evaluated by fluorometric measurements of ph.
The Journal of Physical Chemistry C, 118(29):15723–15731, 2014.

[77] HR Pruppacher.
On the growth of ice crystals in supercooled water and aqueous solution drops.
pure and applied geophysics, 68(1):186–195, 1967.

[78] C Hoose.
Interactive comment on "heterogeneous ice nucleation on atmospheric aerosols: A review of results from laboratory experiments" by c. hoose and o. möhler.
2012.

[79] Benjamin J Murray.
Cracking the problem of ice nucleation.
Science, 355(6323):346–347, 2017.

[80] Richard G Layton and Franklin S Harris Jr.
Nucleation of ice on mica.
Journal of the Atmospheric Sciences, 20(2):142–148, 1963.

[81] JH Shen, K Klier, and AC Zettlemoyer.
Ice nucleation by micas.
Journal of the Atmospheric Sciences, 34(6):957–960, 1977.

[82] David Ehre, Etay Lavert, Meir Lahav, and Igor Lubomirsky.
Water freezes differently on positively and negatively charged surfaces of pyroelectric materials.
Science, 327(5966):672–675, 2010.

[83] Alik Belitzky, Eran Mishuk, David Ehre, Meir Lahav, and Igor Lubomirsky.

Source of electrofreezing of supercooled water by polar crystals.
The journal of physical chemistry letters, 7(1):43–46, 2015.

[84] A. Abdelmonem, E. H. G. Backus, N. Hoffmann, M. A. Sánchez, J. D. Cyran, A. Kiselev, and M. Bonn.
Surface-charge-induced orientation of interfacial water suppresses heterogeneous ice nucleation on α-alumina (0001).
Atmospheric Chemistry and Physics, 17(12):7827–7837, 2017.

[85] Emmanuel Anim-Danso, Yu Zhang, and Ali Dhinojwala.
Surface charge affects the structure of interfacial ice.
The Journal of Physical Chemistry C, 120(7):3741–3748, 2016.

[86] Eun-Mi Choi, Young-Hwan Yoon, Sangyoub Lee, and Heon Kang.
Freezing transition of interfacial water at room temperature under electric fields.
Phys. Rev. Lett., 95:085701, Aug 2005.

[87] B Bera, N Kumar, MHG Duits, MA Cohen Stuart, and F Mugele.
Cationic hofmeister series of wettability alteration in mica–water–alkane systems.
Langmuir, 34(45):13574–13583, 2018.

[88] Lei Xu and Miquel Salmeron.
An xps and scanning polarization force microscopy study of the exchange and mobility of surface ions on mica.
Langmuir, 14(20):5841–5844, 1998.

[89] Aashish Tuladhar, Zizwe A. Chase, Marcel D. Baer, Benjamin A. Legg, Jinhui Tao, Shuai Zhang, Austin D. Winkelman, Zheming Wang, Christopher J. Mundy, James J. De Yoreo, and Hong-fei Wang.
Direct observation of the orientational anisotropy of buried hydroxyl groups inside muscovite mica.
Journal of the American Chemical Society, 141(5):2135–2142, 2019.

[90] Astrid Döppenschmidt and Hans-Jürgen Butt.
Measuring the thickness of the liquid-like layer on ice surfaces with atomic force microscopy.
Langmuir, 16(16):6709–6714, 2000.

[91] Ervin R Van Artsdalen.
Complex ions in molten salts. ionic association and common ion effect.
The Journal of Physical Chemistry, 60(2):172–177, 1956.

[92] Kai Liu, Chunlei Wang, Ji Ma, Guosheng Shi, Xi Yao, Haiping Fang, Yanlin Song, and Jianjun Wang.
Janus effect of antifreeze proteins on ice nucleation.
Proceedings of the National Academy of Sciences, 113(51):14739–14744, 2016.

[93] Brittany Glatz and Sapna Sarupria.
The surface charge distribution affects the ice nucleating efficiency of silver iodide.
J. Chem. Phys., 145(21):211924, December 2016.

[94] Ahmed Abdelmonem, Ellen H. G. Backus, and Mischa Bonn.
Ice nucleation at the water–sapphire interface: Transient sum-frequency response without evidence for transient ice phase.
The Journal of Physical Chemistry C, 122(43):24760–24764, 2018.

[95] X. Yu and H. Hantsche.
Some aspects of the charging effect in monochromatized focused xps.
Fresenius' Journal of Analytical Chemistry, 346(1):233–236, 1993.

[96] H Heimann, S Moskowitz, CR Harihara Iyer, MN Gupta, NS Mankiker, et al.
Silicosis in mica mining in bihar, india.
Arch. Indust. Hyg. & Occupational Med., 8(5):420–35, 1953.

[97] Kai-Tak Wan, Douglas T. Smith, and Brain R. Lawn.
Fracture and contact adhesion energies of mica-mica, silica-silica, and mica-silica interfaces in dry and moist atmospheres.
Journal of the American Ceramic Society, 75(3):667–676, 1992.

[98] H. K. Christenson.
Adhesion and surface energy of mica in air and water.
J. Phys. Chem., 97(46):12034–12041, November 1993.

[99] Guifeng Li, Ali Dhinojwala, and Mohsen S. Yeganeh.
Interference effect from buried interfaces investigated by angular-dependent infrared-visible sum frequency generation technique.
J. Phys. Chem. C, 115(15):7554–7561, April 2011.

[100] Berrin Tansel.
Significance of thermodynamic and physical characteristics on permeation of ions during membrane separation: Hydrated radius, hydration free energy and viscous effects.
Separation and Purification Technology, 86:119 – 126, 2012.

[101] A. Abdelmonem, J. Lützenkirchen, and T. Leisner.
Probing ice-nucleation processes on the molecular level using second harmonic generation spectroscopy.
Atmospheric Measurement Techniques, 8(8):3519–3526, 2015.
Copyright - Copyright Copernicus GmbH 2015; Last updated - 2018-01-22.

[102] Meinrat O. Andreae and Paul J. Crutzen.
Atmospheric aerosols: Biogeochemical sources and role in atmospheric chemistry.
Science, 276(5315):1052–1058, 1997.

[103] M. O. Andreae and P. Merlet.
Emission of trace gases and aerosols from biomass burning.
Global Biogeochemical Cycles, 15(4):955–966, 2001.

[104] V. Ramanathan, P. J. Crutzen, J. T. Kiehl, and D. Rosenfeld.
Aerosols, climate, and the hydrological cycle.
Science, 294(5549):2119–2124, 2001.

[105] Ying Wang, Guoshun Zhuang, Aohan Tang, Hui Yuan, Yele Sun, Shuang Chen, and Aihua Zheng.
The ion chemistry and the source of $PM_{2.5}$ aerosol in beijing.
Atmospheric Environment, 39(21):3771 – 3784, 2005.

[106] Christopher B Field and Michael R Raupach.
The Global Carbon Cycle: Integrating Humans, Climate, and the Natural World, volume 62.
Island Press, 2004.

[107] Wei Hua, Dominique Verreault, and Heather C. Allen.
Relative order of sulfuric acid, bisulfate, hydronium, and cations at the air–water interface.
Journal of the American Chemical Society, 137(43):13920–13926, 2015.
PMID: 26456219.

[108] Wei Hua, Xiangke Chen, and Heather C. Allen.
Phase-sensitive sum frequency revealing accommodation of bicarbonate ions, and charge separation of sodium and carbonate ions within the air/water interface.
The Journal of Physical Chemistry A, 115(23):6233–6238, 2011.
PMID: 21513316.

[109] Wei Hua, Aaron M. Jubb, and Heather C. Allen.
Electric field reversal of Na_2SO_4, $(NH_4)_2SO_4$, and Na_2CO_3 relative to $CaCl_2$ and NaCl at the air/aqueous interface revealed by heterodyne detected phase-sensitive sum frequency.
The Journal of Physical Chemistry Letters, 2(20):2515–2520, 2011.

[110] Erwin A Vogler.
Structure and reactivity of water at biomaterial surfaces.
Advances in Colloid and Interface Science, 74(1):69 – 117, 1998.

[111] Pavel Jungwirth and Douglas J. Tobias.
Ions at the air/water interface.
The Journal of Physical Chemistry B, 106(25):6361–6373, 2002.

[112] E. M. Knipping, M. J. Lakin, K. L. Foster, P. Jungwirth, D. J. Tobias, R. B. Gerber, D. Dabdub, and B. J. Finlayson-Pitts.
Experiments and simulations of ion-enhanced interfacial chemistry on aqueous NaCl aerosols.
Science, 288(5464):301–306, 2000.

[113] Ken-ichi Ataka, Takao Yotsuyanagi, and Masatoshi Osawa.
Potential-dependent reorientation of water molecules at an electrode/electrolyte interface studied by surface-enhanced infrared absorption spectroscopy.
The Journal of Physical Chemistry, 100(25):10664–10672, 1996.

[114] Sietse T. van der Post, Cho-Shuen Hsieh, Masanari Okuno, Yuki Nagata, Huib J. Bakker, Mischa Bonn, and Johannes Hunger.

Strong frequency dependence of vibrational relaxation in bulk and surface water reveals sub-picosecond structural heterogeneity.
Nature Communications, 6:8384, September 2015.

[115] Ruth A. Livingstone, Yuki Nagata, Mischa Bonn, and Ellen H. G. Backus.
Two types of water at the water–surfactant interface revealed by time-resolved vibrational spectroscopy.
Journal of the American Chemical Society, 137(47):14912–14919, 2015.
PMID: 26544087.

[116] R. W. Leach and H. Gursky.
The cosmic ray background in charge coupled devices.
Publications of the Astronomical Society of the Pacific, 91:855, dec 1979.

[117] Maria Sovago, R. Kramer Campen, George W. H. Wurpel, Michiel Müller, Huib J. Bakker, and Mischa Bonn.
Vibrational response of hydrogen-bonded interfacial water is dominated by intramolecular coupling.
Phys. Rev. Lett., 100:173901, Apr 2008.

[118] Satoshi Nihonyanagi, Tatsuya Ishiyama, Touk-kwan Lee, Shoichi Yamaguchi, Mischa Bonn, Akihiro Morita, and Tahei Tahara.
Unified molecular view of the air/water interface based on experimental and theoretical $\chi(2)$ spectra of an isotopically diluted water surface.
Journal of the American Chemical Society, 133(42):16875–16880, 2011.
PMID: 21899354.

[119] Jan Schaefer, Ellen H. G. Backus, Yuki Nagata, and Mischa Bonn.
Both inter- and intramolecular coupling of O–H groups determine the vibrational response of the water/air interface.
The Journal of Physical Chemistry Letters, 7(22):4591–4595, 2016.
PMID: 27797213.

[120] Yuki Nagata and Shaul Mukamel.
Vibrational sum-frequency generation spectroscopy at the water/lipid interface: Molecular dynamics simulation study.
Journal of the American Chemical Society, 132(18):6434–6442, 2010.
PMID: 20394423.

[121] G. M. Gale, G. Gallot, F. Hache, N. Lascoux, S. Bratos, and J-Cl. Leicknam.
Femtosecond dynamics of hydrogen bonds in liquid water: A real time study.
Phys. Rev. Lett., 82:1068–1071, Feb 1999.

[122] Maria Sovago, R. Kramer Campen, Huib J. Bakker, and Mischa Bonn.
Hydrogen bonding strength of interfacial water determined with surface sum-frequency generation.
Chemical Physics Letters, 470(1):7 – 12, 2009.

[123] Shoichi Yamaguchi.

Development of single-channel heterodyne-detected sum frequency generation spectroscopy and its application to the water/vapor interface.
The Journal of Chemical Physics, 143(3):034202, 2015.

[124] Kailash C. Jena, Paul A. Covert, and Dennis K. Hore.
The effect of salt on the water structure at a charged solid surface: Differentiating second- and third-order nonlinear contributions.
The Journal of Physical Chemistry Letters, 2(9):1056–1061, 2011.

[125] Simone Pezzotti, Daria Ruth Galimberti, Y Ron Shen, and Marie-Pierre Gaigeot.
Structural definition of the bil and dl: A new universal methodology to rationalize non-linear $\chi^{(2)}(\omega)$ SFG signals at charged interfaces, including $\chi^{(3)}(\omega)$ contributions.
Physical chemistry chemical physics : PCCP, 20(7):5190—5199, February 2018.

[126] D. E. Gragson, B. M. McCarty, and G. L. Richmond.
Ordering of interfacial water molecules at the charged air/water interface observed by vibrational sum frequency generation.
Journal of the American Chemical Society, 119(26):6144–6152, 1997.

[127] Alexander M. Smith, Alpha A. Lee, and Susan Perkin.
The electrostatic screening length in concentrated electrolytes increases with concentration.
The Journal of Physical Chemistry Letters, 7(12):2157–2163, 2016.
PMID: 27216986.

[128] Sudipta Das, Mischa Bonn, and Ellen H. G. Backus.
The surface affinity of cations depends on both the cations and the nature of the surface.
The Journal of Chemical Physics, 150(4):044706, 2019.

[129] Takako Imamura, Yuri Mizukoshi, Tatsuya Ishiyama, and Akihiro Morita.
Surface structures of NaF and Na_2SO_4 aqueous solutions: Specific effects of hard ions on surface vibrational spectra.
The Journal of Physical Chemistry C, 116(20):11082–11090, 2012.

[130] Satoshi Nihonyanagi, Ryoji Kusaka, Ken-ichi Inoue, Aniruddha Adhikari, Shoichi Yamaguchi, and Tahei Tahara.
Accurate determination of complex $\chi^{(2)}$ spectrum of the air/water interface.
The Journal of Chemical Physics, 143(12):124707, 2015.

[131] M Bonn, H Ueba, and M Wolf.
Theory of sum-frequency generation spectroscopy of adsorbed molecules using the density matrix method—broadband bibrational sum-frequency generation and applications.
Journal of Physics: Condensed Matter, 17(8):S201–S220, feb 2005.

[132] Michitoshi Hayashi, Ying-Jen Shiu, Kuo Kan Liang, Sheng Hsien Lin, and Yuan Ron Shen.

Theory of time-resolved sum-frequency generation and its applications to vibrational dynamics of water.
The Journal of Physical Chemistry A, 111(37):9062–9069, 2007.
PMID: 17725327.

[133] Shunhao Xiao, Florian Figge, Guillaume Stirnemann, Damien Laage, and John A. McGuire.
Orientational dynamics of water at an extended hydrophobic interface.
Journal of the American Chemical Society, 138(17):5551–5560, 2016.
PMID: 27045950.

[134] Cho-Shuen Hsieh, R. Kramer Campen, Ana Celia Vila Verde, Peter Bolhuis, Han-Kwang Nienhuys, and Mischa Bonn.
Ultrafast reorientation of dangling OH groups at the air-water interface using femtosecond vibrational spectroscopy.
Phys. Rev. Lett., 107:116102, Sep 2011.

[135] Zhen Zhang, Lukasz Piatkowski, Huib J. Bakker, and Mischa Bonn.
Ultrafast vibrational energy transfer at the water/air interface revealed by two-dimensional surface vibrational spectroscopy.
Nat Chem, 3(11):888–893, November 2011.

[136] Sho Imoto, Sotiris S. Xantheas, and Shinji Saito.
Ultrafast dynamics of liquid water: Energy relaxation and transfer processes of the OH stretch and the HOH bend.
The Journal of Physical Chemistry B, 119(34):11068–11078, 2015.
PMID: 26042611.

[137] Rossend Rey, Klaus B. Møller, and James T. Hynes.
Ultrafast vibrational population dynamics of water and related systems: a theoretical perspective.
Chemical Reviews, 104(4):1915–1928, 2004.
PMID: 15080716.

[138] Rossend Rey and James T. Hynes.
Vibrational energy relaxation of HOD in liquid D_2O.
The Journal of Chemical Physics, 104(6):2356–2368, 1996.

[139] S. Ashihara, N. Huse, A. Espagne, E.T.J. Nibbering, and T. Elsaesser.
Vibrational couplings and ultrafast relaxation of the O–H bending mode in liquid H_2O.
Chemical Physics Letters, 424(1):66 – 70, 2006.

[140] Dominika Lesnicki and Marialore Sulpizi.
A microscopic interpretation of pump–probe vibrational spectroscopy using ab initio molecular dynamics.
The Journal of Physical Chemistry B, 122(25):6604–6609, 2018.
PMID: 29799755.

[141] Malte Deiseroth, Mischa Bonn, and Ellen Backus.

Orientation independent vibrational dynamics of lipid-bound interfacial water. *Phys. Chem. Chem. Phys.*, pages –, 2020.

[142] Gerrit van Meer, Dennis R. Voelker, and Gerald W. Feigenson.
Membrane lipids: Where they are and how they behave.
Nature Reviews Molecular Cell Biology, 9:112, February 2008.

[143] Emily K. Perttu, Aditya G. Kohli, and Francis C. Szoka.
Inverse-phosphocholine lipids: A remix of a common phospholipid.
Journal of the American Chemical Society, 134(10):4485–4488, 2012.
PMID: 22364493.

[144] Lisa B. Dreier, Amanuel Wolde-Kidan, Douwe Jan Bonthuis, Roland R. Netz, Ellen H.G. Backus, and Mischa Bonn.
Unraveling the origin of the apparent charge of zwitterionic lipid layers.
The Journal of Physical Chemistry Letters, 10(20):6355–6359, 2019.
PMID: 31568720.

[145] Woongmo Sung, Sangjun Seok, Doseok Kim, C. S. Tian, and Y. R. Shen.
Sum-frequency spectroscopic study of langmuir monolayers of lipids having oppositely charged headgroups.
Langmuir, 26(23):18266–18272, 2010.
PMID: 20977244.

[146] Xiangke Chen, Wei Hua, Zishuai Huang, and Heather C. Allen.
Interfacial water structure associated with phospholipid membranes studied by phase-sensitive vibrational sum frequency generation spectroscopy.
Journal of the American Chemical Society, 132(32):11336–11342, 2010.
PMID: 20698700.

[147] Prashant Chandra Singh, Ken-ichi Inoue, Satoshi Nihonyanagi, Shoichi Yamaguchi, and Tahei Tahara.
Femtosecond hydrogen bond dynamics of bulk-like and bound water at positively and negatively charged lipid interfaces revealed by 2D HD-VSFG spectroscopy.
Angewandte Chemie International Edition, 55(36):10621–10625, 2016.

[148] Ken-ichi Inoue, Prashant C. Singh, Satoshi Nihonyanagi, Shoichi Yamaguchi, and Tahei Tahara.
Cooperative hydrogen-bond dynamics at a zwitterionic lipid/water interface revealed by 2D HD-VSFG spectroscopy.
The Journal of Physical Chemistry Letters, 8(20):5160–5165, 2017.
PMID: 28990784.

[149] Jenée D. Cyran, Ellen H. G. Backus, Yuki Nagata, and Mischa Bonn.
Structure from dynamics: Vibrational dynamics of interfacial water as a probe of aqueous heterogeneity.
The Journal of Physical Chemistry B, 122(14):3667–3679, 2018.
PMID: 29490138.

[150] YR Shen.
Surface properties probed by second-harmonic and sum-frequency generation.
Nature, 337(6207):519, 1989.

[151] Jahur A. Mondal, Satoshi Nihonyanagi, Shoichi Yamaguchi, and Tahei Tahara.
Three distinct water structures at a zwitterionic lipid/water interface revealed by heterodyne-detected vibrational sum frequency generation.
Journal of the American Chemical Society, 134(18):7842–7850, 2012.
PMID: 22533664.

[152] Peter Hamm and Martin Zanni.
Concepts and Methods of 2D Infrared Spectroscopy.
Cambridge University Press, 2011.

[153] Prashant Chandra Singh, Satoshi Nihonyanagi, Shoichi Yamaguchi, and Tahei Tahara.
Ultrafast vibrational dynamics of water at a charged interface revealed by two-dimensional heterodyne-detected vibrational sum frequency generation.
The Journal of Chemical Physics, 137(9):094706, 2012.

[154] N. Ji, V. Ostroverkhov, C. S. Tian, and Y. R. Shen.
Characterization of vibrational resonances of water-vapor interfaces by phase-sensitive sum-frequency spectroscopy.
Phys. Rev. Lett., 100:096102, Mar 2008.

[155] V. Buch.
Molecular structure and oh-stretch spectra of liquid water surface.
J. Phys. Chem. B, 109(38):17771–17774, September 2005.

[156] Hajime Torii.
Time-domain calculations of the polarized raman spectra, the transient infrared absorption anisotropy, and the extent of delocalization of the oh stretching mode of liquid water.
J. Phys. Chem. A, 110(30):9469–9477, August 2006.

[157] B. M. Auer and J. L. Skinner.
Ir and raman spectra of liquid water: Theory and interpretation.
J. Chem. Phys., 128(22):224511, June 2008.

[158] Aniket Magarkar, Tomasz Róg, and Alex Bunker.
Molecular dynamics simulation of inverse-phosphocholine lipids.
The Journal of Physical Chemistry C, 118(33):19444–19449, 2014.

[159] Tatsuhiko Ohto, Ellen H. G. Backus, Cho-Shuen Hsieh, Marialore Sulpizi, Mischa Bonn, and Yuki Nagata.
Lipid carbonyl groups terminate the hydrogen bond network of membrane-bound water.
The Journal of Physical Chemistry Letters, 6(22):4499–4503, 2015.
PMID: 26506078.

[160] Tatsuya Ishiyama, Daichi Terada, and Akihiro Morita.
Hydrogen-bonding structure at zwitterionic lipid/water interface.
The Journal of Physical Chemistry Letters, 7(2):216–220, 2016.
PMID: 26713682.

[161] Suyong Re, Wataru Nishima, Tahei Tahara, and Yuji Sugita.
Mosaic of water orientation structures at a neutral zwitterionic lipid/water interface revealed by molecular dynamics simulations.
J. Phys. Chem. Lett., 5(24):4343–4348, December 2014.

[162] Ken-ichi Inoue, Satoshi Nihonyanagi, Prashant C. Singh, Shoichi Yamaguchi, and Tahei Tahara.
2D heterodyne-detected sum frequency generation study on the ultrafast vibrational dynamics of H_2O and HOD water at charged interfaces.
The Journal of Chemical Physics, 142(21):212431, 2015.

[163] Kyungwon Kwak, Sungnam Park, Ilya J. Finkelstein, and M. D. Fayer.
Frequency-frequency correlation functions and apodization in two-dimensional infrared vibrational echo spectroscopy: A new approach.
J. Chem. Phys., 127(12):124503, September 2007.

[164] Avishek Ghosh, Marc Smits, Jens Bredenbeck, and Mischa Bonn.
Membrane-bound water is energetically decoupled from nearby bulk water: an ultrafast surface-specific investigation.
J. Am. Chem. Soc., 129(31):9608–9609, August 2007.

[165] Krupa Ramasesha, Luigi De Marco, Aritra Mandal, and Andrei Tokmakoff.
Water vibrations have strongly mixed intra- and intermolecular character.
Nature Chemistry, 5(11):935–940, 2013.

[166] Eric Tyrode, Sanghamitra Sengupta, and Adrien Sthoer.
Identifying eigen-like hydrated protons at negatively charged interfaces.
Nature Communications, 11(1):493, 2020.